PHYSIK–DEPARTMENT

Quantifying the thermodynamic driving force of monolayer self-assembly at liquid-solid interfaces

Dissertation

Wentao Song

TECHNISCHE UNIVERSITÄT
MÜNCHEN

TECHNISCHE UNIVERSITÄT MÜNCHEN
Fakultät für Physik
Oskar-von-Miller Lehrstuhl für Wissenschaftskommunikation

Quantifying thermodynamic driving force of monolayer self-assembly at liquid-solid interfaces

Wentao Song

Vollständiger Abdruck der von der Fakultät für Physik der Technischen Universität München zur Erlangung des akademischen Grades eines

Doktors der Naturwissenschaften
(Dr. rer. nat.)

genehmigten Dissertation.

Vorsitzender: Univ.-Prof. Dr. U. Gerland

Prüfer der Dissertation:

1. Priv.-Doz. Dr. M. Lackinger
2. Univ.-Prof. Dr. J. Barth

Die Dissertation wurde am 29.01.2015 bei der Technischen Universität München eingereicht und durch die Fakultät für Physik am 13.04.2015 angenommen.

Content

List of abbreviations v

Abstract I

Kurzfassung I

Introduction and motivation 1

Chapter 1: Scanning Tunneling Microscope 5

- Introduction 5
- 1.1 Theoretical description 5
  - 1.1.1 Simplified one dimensional model 6
  - 1.1.2 Time dependent perturbation theory 7
  - 1.1.3 Tersoff-Hamann approximation 9
  - 1.1.4 More sophisticated theories 10
- 1.2 Experimental setup 11

Chapter 2: Thermodynamic Methods 13

- 2.1 Sublimation enthalpy 13
  - 2.1.1 Theoretical description 13
  - 2.1.2 Experimental setup 15
- 2.2 Total monolayer binding enthalpy 18
  - 2.2.1 Theoretical description of desorption 18
  - 2.2.2 Quadrupole mass spectrometer 19
  - 2.2.3 Experimental setup 20
  - 2.2.4 Analyzing TPD spectra 22
- 2.3 Dissolution enthalpy 25
  - 2.3.1 Thermodynamics of solvation 25
  - 2.3.2 Theoretical description of electronic transitions 26
  - 2.3.3 Experimental setup and an example 27
- 2.4 Computational methods 29
  - 2.4.1 Molecular mechanics 29
  - 2.4.2 Molecular dynamics 30
  - 2.4.3 Density functional theory 30
- 2.5 Evaluation of the entropy change 33

Chapter 3: Non-covalent interactions 37

Solutes and solvents 37

3.1 Hydrogen bonds 38

3.2 Halogen bonds 39

3.3 Surface-molecule interactions 40

Chapter 4: Born-Haber cycle for monolayer self-assembly at the liquid-solid interface – assessing the enthalpic driving force 43

4.1 Abstract 43

4.2 Introduction 43

4.3 Methods 46

- 4.3.1 Experimental methods 46
- 4.3.2 Computational methods 46

4.4 Results and discussion 47

- 4.4.1 Monolayer structure 47
- 4.4.2 Born-Haber cycle. 48
- 4.4.3 Sublimation enthalpy. 49
- 4.4.4 Enthalpy of dissolution. 50
- 4.4.5 Binding enthalpy of TPA in a monolayer on graphite with respect to vacuum 52
- 4.4.6 Dewetting enthalpy 53
- 4.4.7 Overall enthalpy change for self-assembly of interfacial TPA monolayers 54
- 4.4.8 Concentration threshold for monolayer self-assembly 55
- 4.4.9 Entropy cost vs. enthalpy gain 55
- 4.4.10 Temperature threshold of thermodynamical stability 57

4.5 Supporting information 60

- 4.5.1 Experimental Details 60
- 4.5.2 Additional STM Results 62
- 4.5.3 Computational Details and Additional Results 63
- 4.5.4 Energy of the 9A Wetting Layer 67
- 4.5.5 TPA Dimers Formation in Solution 70

4.6 Conclusion and Summary 71

Chapter 5: Thermodynamics of 4, 4’-stilbenedicarboxylic acid monolayer self-assembly at the nonanoic acid-graphite interface 73

5.1 Abstract 73

5.2 Introduction 73

5.3 Methods 77

- 5.3.1 Experimental 77

5.3.2 Computational 78
5.4 Results and discussion 78
5.4.1 Monolayer structure 78
5.4.2 Born-Haber cycle 79
5.4.3 Binding enthalpy of monolayer on graphite with respect to vacuum 80
5.4.4 Sublimation enthalpy 82
5.4.5 Dissolution enthalpy 84
5.4.6 Dewetting Enthalpy 85
5.4.7 Total binding energy and entropy 87
5.5 Supporting information 88
STM Split image. 88
5.6 Conclusion and Summary 89
Chapter 6: Thermodynamics of halogen bonded monolayer self-assembly at the liquid–solid interface 93
6.1 Abstract 93
6.2 Introduction 93
6.3 Results and discussion 94
6.4 Supporting information 99
6.4.1 STM experiments 99
6.4.2 Additional STM data 100
6.4.3 Density Functional Theory 102
6.5 Conclusion and summary 105
Chapter 7: Conclusions and outlook 107
References 113
List of Figures 137
List of Publications 139
Acknowledgement 141
Curriculum Vitae 142
University Studies 142
Teaching Experiences 142

List of abbreviations

1D	One-dimensional
2D	Two-dimensional
3D	Three-dimensional
TPA	Terephthalic acid
9A	Nonanoic acid
SDA	4, 4’- stilbenedicarboxylic acid
HBTP	Hexabromotriphenylene
7A	Heptanoic acid
STM	Scanning tunneling microscope
MFC	Microflow calorimetry
MM	Molecular mechanics
MD	Molecular dynamics
MC	Monte Carlo
DFT	Density functional theory
TPD	Temperature programmed desorption
SEM	Secondary electron multiplier
UHV	Ultra-high vacuum
LDOS	Local density of states
ESQC	Electron scattering quantum chemistry
QCMB	Quartz crystal microbalance
OMBE	Organic molecular-beam epitaxy
QMA	Quadrupole mass analyzer
QMS	Quadrupole mass spectrometer
UV-vis	Ultraviolet to Visible
B&E bands	Benzoic and Ethylenic bands
NVT ensemble	The canonical ensemble
GGA	Generalized gradient approximation
PBE	Perdew-Burke-Ernzerhof functional

vdW-DF	Van der Waals density functional
RAHBs	Resonance assisted hydrogen bond
B3LYP functional	Becke, 3-parameter, Lee-Yang-Parr hybrid functional
6-31G(d)	DFT basis set
CCSD (T)	The single, double, and perturbative triple excitation coupled cluster method

Abstract

This dissertation deals with the quantification of the thermodynamic driving force, i.e. the Gibbs free energy change (ΔG), of monolayer self-assembly at liquid-solid interfaces. The knowledge of ΔG provides important information for targeted 2D-nanostructure fabrication. Enthalpy and entropy contributions are quantified separately and compared to each other.

A direct calorimetric measurement of the overall enthalpy change of self-assembly is almost impossible for most systems of interest. In this dissertation, the enthalpy change is quantified in an indirect way. Sublimation enthalpy, dissolution enthalpy, total monolayer binding enthalpy, and a dewetting enthalpy are determined independently. These enthalpies are combined into an adapted Born-Haber cycle to derive the overall enthalpy change upon self-assembly. Entropies are estimated using a theoretical model proposed by Whitesides et al. evaluated at the concentration threshold of self-assembly. For solutions with a concentration lower than this threshold, stable monolayers are no longer observed. At this critical condition, entropy and enthalpy contributions are equal, i.e. $\Delta H = T\Delta S$.

Two hydrogen bonded and one halogen bonded networks were studied as model systems. Individual enthalpy changes as well as the total enthalpy change upon self-assembly were obtained by using an array of experimental techniques, computational approaches or a hybrid of both.

Self-assembly of terephthalic acid (TPA) was studied as a model system at the nonanoic acid (9A)-graphite interface by employing the Born-Haber cycle. For this system, every experimentally obtained enthalpy difference was directly compared to the corresponding theoretical enthalpy value. The latter was obtained using molecular mechanics and molecular dynamics simulations, resulting in a perfect agreement with the experimental values for each enthalpy. From the resulting Born-Haber cycle it is concluded that the presence of the supernatant solution lowers the total enthalpy change of self-assembly to only a few percent of the equivalent value in vacuum.

Yet, the estimated entropy contribution of individual unsolvated molecules is significantly higher than the overall enthalpy change. These results would imply that the dissolved molecule is thermodynamically more favorable than the self-assembled monolayer at the 9A-graphite interface. In order to resolve this contradiction, we propose a solvation model, i.e. in solution phase TPA molecules break 9A-9A dimers and recombine into 9A-TPA-9A complexes. The corresponding entropy contribution is in perfect

agreement with the enthalpy gain derived from the Born-Haber cycle. Hence, we conclude that solvation of TPA solute with 9A solvent molecules is important to render self-assembly of TPA monolayer a thermodynamically favorable process.

Self-assembly of 4,4'-stilbenedicarboxylic acid (SDA) was also studied at the 9A-graphite interface to reveal the role of the enlarged aromatic backbone for the stabilization of monolayers at the solution-graphite interface. Based on a thorough comparison with the case of TPA, we conclude that interaction of the extended aromatic system with the graphite surface significantly enhances the surface binding enthalpy, thus the stability of the monolayer.

Similarly, halogen bond mediated self-assembly of hexabromotriphenylene (HBTP) was studied at the 7A-graphite interface using a hybrid Born-Haber cycle. The total binding enthalpy of a molecule in an adsorbed monolayer was obtained by density functional theory (DFT) simulations with empirical dispersion correction. In comparison to the dicarboxylic acids, molecule-molecule interactions are significantly weaker for HBTP. HBTP monolayer are mainly stabilized by relatively strong molecule-surface interactions.

Also for HBTP, the Born-Haber cycle was employed with the experimentally measured sublimation and dissolution enthalpies. Thereby, the total enthalpy change is lowered to ~50% of the vacuum value by the presence of the solvent. A direct comparison of the overall enthalpy gain directly with the estimated entropy contribution of unsolvated molecules shows that the solvent influence is significantly weaker for HBTP than in fatty acids for TPA and SDA. Further DFT simulations suggest that the HBTP-7A interaction is not strong enough to break 7A dimers. This implies that HBTP in 7A does not have a strongly bound solvation shell. Accordingly, there is no significant favorable entropy contribution from the releasing solvent molecules from solvation shell upon self-assembly of HBTP monolayer.

.

Kurzfassung

Gegenstand der Dissertation ist die Quantifizierung der thermodynamischen Antriebskraft, d.h. die Änderung der Gibbs-Energie (ΔG), bei der Selbst-Assemblierung von Monolagen an flüssig-fest Grenzflächen. Die Kenntnis von ΔG ist eine wichtige Information für die gezielte Herstellung von 2D Nanostrukturen. Die Enthalpie- und Entropie-Beiträge werden dabei separat quantifiziert und miteinander verglichen.

Eine direkte kalorimetrische Messung der Gesamtänderung der Enthalpie bei der Selbst-assemblierung ist für viele relevante Systeme praktisch nicht möglich. In dieser Dissertation wird diese Enthalpieänderung indirekt quantifiziert. Sublimationsenthalpie, Lösungsenthalpie, die Gesamtbindungsenthalpie in Monolagen und eine Enthalpie für Entnetzung werden unabhängig voneinander bestimmt. Diese Enthalpien werden in einem angepassten Born-Haber-Kreisprozess kombiniert, um daraus die Gesamtänderung der Enthalpie bei der Selbstassemblierung abzuleiten. Entropien werden mit einem von Whitesides et al. vorgeschlagenen theoretischen Modell abgeschätzt, wobei dafür Konzentrationsschwellwerte der Selbst-Assemblierung verwendet werden. Für Lösungen mit Konzentrationen unterhalb dieses Schwellwerts werden keine stabilen Monolagen mehr beobachtet. Bei dieser kritischen Konzentration sind enthalpische und entropische Beiträge gleich, d.h. $\Delta H = T\Delta S$.

Als Modellsysteme wurden zwei über Wasserstoffbrückenbindungen und eine über Halogen-Bindungen gebundene Netzwerke untersucht. Die einzelnen Enthalpieänderungen, sowie die Gesamtänderung der Enthalpie bei der Selbstassemblierung wurden mit einer Reihe experimenteller Techniken, mit Simulationen oder einem Hybrid aus beidem erhalten.

Die Selbstassemblierung von Terephthalsäure (TPA) wurde als Modellsystem an der Nonansäure-(9A)-Graphit-Grenzfläche mittels des Born-Haber Kreisprozesses untersucht. Für dieses System wurde jeder experimentell bestimmte Enthalpieunterschied direkt mit dem entsprechenden theoretischen Wert verglichen. Diese wurden mittels Molekularmechanik und Molekulardynamik Simulationen ermittelt und zeigten eine perfekte Übereinstimmung mit allen experimentellen Enthalpien. Aus dem Born-Haber-Kreisprozess lässt sich ableiten, dass das überstehende Lösungsmittel die Gesamtänderung der Enthalpie bei der Selbstassemblierung auf nur wenige Prozent des äquivalenten Wertes im Vakuum reduziert.

Jedoch ist der abgeschätzte Entropieverlusts bei der Selbstassemblierung einzelner, nicht solvatisierter Moleküle deutlich höher als der Enthalpiegewinn. Dieses Ergebnis würde implizieren, dass das gelöste Molekül thermodynamisch günstiger wäre als die selbst-assemblierte Monolage an der 9A-Graphit-Grenzfläche. Zur Klärung dieses Widerspruchs wird ein Solvatationsmodell vorgeschlagen, bei dem TPA-Moleküle in der Lösung 9A-9A Lösungsmittel Dimere aufspalten und 9A-TPA-9A-Komplexe bilden. Die entsprechende Entropieänderung ist in sehr guter Übereinstimmung mit der Enthalpieänderung aus dem Born-Haber Kreisprozess. Daraus lässt sich schließen, dass die Solvatation von gelösten TPA mit 9A Lösungsmittelmolekülen ausschlaggebend dafür ist, dass die Selbstassemblierung von TPA Monolagen thermodynamisch begünstigt wird.

Die Selbstassemblierung von 4,4'-Stilbendicarbonsäure (SDA) wurde ebenfalls an der Grenzfläche von Nonansäure (9A) und Graphit untersucht, um den Beitrag des vergrößerten aromatischen Gerüsts zur Stabilisierung von Monolagen an der flüssig-fest Grenzfläche zu untersuchen. Basierend auf einem gründlichen Vergleich der Enthalpieänderungen mit dem Fall von TPA wird gefolgert, dass die Wechselwirkung des vergrößerten aromatischen Systems mit der Graphit Oberfläche die Oberflächenbindungsenergie und damit die Stabilität der Monolagen signifikant erhöht.

Gleichermaßen wurde die von Halogen-Bindungen vermittelte Selbstassemblierung von Hexabromo-triphenylen (HBTP) an der 7A-Graphit-Grenzfläche mit einem hybrid Born-Haber-Kreisprozess untersucht. Die Gesamtbindungsenthalpie der Moleküle in einer adsorbierten Monolage wurde mittels Dichte Funktional-Theorie (DFT) mit empirischer Dispersionskorrektur ermittelt. Im Vergleich zu den Dicarbonsäuren TPA und SDA sind bei HBTP die Molekül-Molekül Wechselwirkungen deutlich schwächer. HBTP Monolagen werden hauptsächlich durch relativ starke Molekül-Oberfläche Wechselwirkungen stabilisiert.

Gleichermaßen wird für HBTP der Born-Haber Kreisprozesses angewandt mit experimentell bestimmten Lösungs- und Sublimationsenthalpien. Dabei wird eine Verringerung der gesamten Enthalpieänderung durch das Lösungsmittel auf etwa 50% des Wertes in Vakuum festgestellt. Der direkte Vergleich der gesamten Enthalpieänderung mit dem Entropieverlust unsolvatisierter Moleküle zeigt, dass der Lösungsmitteleinfluss für HBTP in Fettsäuren deutlich geringer ist als bei SDA und TPA. Weiterreichende DFT Simulationen legen nahe, dass die HBTP-7A Wechselwirkungen zu schwach sind um 7A-7A Dimere aufzubrechen. Dies impliziert, dass HBTP in 7A keine stark gebundene Solvatationshülle hat. Entsprechend gibt es keinen begünstigenden signifikanten Entropiebeitrag durch die Freisetzung von Lösungsmittel Molekülen aus der Solvatationshülle bei der Selbstassemblierung von HBTP Monolagen.

Introduction and motivation

For hundreds of years, chemistry has been focused on molecular structures and properties. Interactions and reactions between molecules are the connections between microscopic structure and macroscopic properties of materials. Since supramolecular chemistry was proposed by J. M. Lehn in the 1980s [1], chemistry study has moved to a new level that goes beyond the molecule [2]. Owing to the high applications potential in biology and catalysis, supramolecular chemistry has become one of the most important fields in the 21st century. It studies the structure and properties of supramolecular systems, where two or more molecules are linked by non-covalent bonds. The main objects of study are functional systems formed with weak intermolecular interactions, e.g. hydrogen bonds, halogen bonds, and van-der-Waals interactions. Using non-covalent bonds to build two- or three-dimensional (2D/3D) structures with long-range order is a new concept in engineering of functional materials [3-5].

In the field of nanoscience and nanotechnology, the bottom-up methods to fabricate nanostructures are attracting more and more attentions, since the traditional top-down techniques suffer from limitations in the resolution and accuracy. Among all the different bottom-up methods, molecular self-assembly on single crystal surface plays a special role due to both conceptual and analytical advantages. On the one hand, single crystal surfaces provide an interface and support for nanostructures, an important prerequisite for applications in sensors, catalysis, and organic electronics [6-8]. On the other hand, surface-supported monolayers are ideal samples for real space analytical techniques like the scanning probe microscopy, in particular scanning tunneling microscopy (STM) [9-12]. Hence, a fundamental understanding of mechanisms and driving forces of supramolecular self-assembly is becoming an important topic towards the aim of targeted and efficient nano fabrication [13-17].

Among all dimensionalities and environments, self-assembly at the liquid-solid interface has attracted particular interest not only because of the high relevance to applications such as the lubrication, thin film based organic electronics, and biosensors, but also due to the facile sample preparation [18, 19]. Thermodynamic and kinetic influences of the liquid phase on self-assembly have been demonstrated experimentally [20-22]. Compared to self-assembly in vacuum, the desorption barrier of a self-assembled monolayer is significantly lowered, thereby substantially enhancing the vertical mobility and the intermolecular bond reversibility of the building blocks. As a result, self-assembly at the liquid-solid interface is highly dynamic and in many cases represents thermodynamically most favorable structures [11, 12, 23-25]. Accordingly, thermodynamic models have successfully explained structure formation and phase selection. For self-assembly of larger molecules or stronger interacting surfaces, molecular mobility is lowered by stronger surface-molecule interactions. Hence metastable phases can emerge because of kinetic hindering due to the surface [26]. The lowering of Gibbs free energy is the thermodynamic driving force of self-assembly, i.e. $\Delta G < 0$. Thermodynamic models based on chemical potentials have successfully explained concentration induced phase selection of self-assembly for both homogenous [27, 28] and heterogeneous systems [20]. Recently, de Feyter *et al.* have extended this approach [29] by utilizing temperature dependent STM measurement at different solute concentrations. Their method utilizes experimentally obtained phase transition temperature as an additional experimental parameter for the thermodynamic model. Therefore, it is possible to determine the binding enthalpies and entropies of both phases with respect to the solution phase using a series of carefully performed STM measurement. However, since the basic ingredient of this method is the phase transition temperature with respect to solute concentration, the method is only suitable for systems where polymorphic self-assembly occurs. In addition, the method reads out coverage ratios of different phases in temperature dependent STM images. Moreover, it addresses the overall enthalpy of porous monolayers, but is not able to isolate solvent influences nor to assess individual enthalpy contributions.

Alternatively, Gibbs free energy changes of monolayer self-assemblies can be estimated by evaluating the enthalpy and entropy contributions separately [21, 30]. Molecular mechanics (MM) and molecular dynamics (MD) are often the method of choice for enthalpy evaluation and have been demonstrated to be effective for many systems [20, 21, 28, 30-33]. Although MD and Monte Carlo (MC) simulations have been successfully employed to understand monolayer formation and phase selection [33-37], none of them consider the supernatant solution phase. In addition, MM and MD simulations are not appropriate when intermolecular forces are dependent on electron distribution, as for instance in halogen bonds. In those cases, quantum chemical simulations, for instance density functional theories (DFT), are usually required [38-40].

From the experimental side, a direct measurement of the enthalpy change of monolayer self-assembly at the liquid/solid interface by traditional calorimeters can be very difficult. For most systems, the enthalpy change of self-assembly can be too low to measure. In principle, micro flow calorimetry (MFC) is an established technique to directly measure enthalpies upon adsorption at solution-graphite interfaces [41]. By using large surface areas as available in graphitized carbon black, the adsorption enthalpy is amplified to a measurable range. However, some obvious disadvantages exist. First, the normalization of adsorption energies requires a precise measurement of surface area. This area is typically obtained from gas adsorption experiments, which are not parameter free. Second, MFC is limited to graphite (0001) facets, where large distinct crystallographic surfaces is available as for graphitized carbon black. Furthermore, its accuracy decreases with overall enthalpy change.

In this dissertation, different experimental techniques and computational methods are combined to provide a detailed quantitative view of all enthalpy contributions. Bulk crystal, surface supported monolayers in vacuum, free molecules in vacuum, and monolayers at solution-graphite interfaces are defined as reference states. Accordingly, an adapted Born-Haber cycle is introduced to derive the total enthalpy gain upon self-assembly. Moreover, the subtle thermodynamic balance of self-assembly can be addressed, especially the solvent effect which is of particular importance. For instance, this effect may act as the key factor in structure selection for polymorphic systems [42-44]. Independently performed simulations are compared to experimental results, in order to achieve a thorough understanding of intermolecular interactions. Compared to the previously mentioned approaches, this method circumvents many difficulties, and at the same time, gives not only the overall enthalpy change, but also a detailed enthalpy picture of contributions including the solvent effect.

Chapter 1 introduces the basic working principle of STM. The first part introduces the theoretical description of STM imaging, the simplest one-dimensional tunneling theory, Bardeen's perturbation theory, and the three-dimensional spherical tip model by Tersoff and Hamann. The chapter also briefly introduces more sophisticated models. The second part focuses on the basic setup and principles of the ambient STM system used in this work.

Chapter 2 introduces all experimental and computational approaches used to quantify the enthalpies and entropies. Experimental approaches include temperature dependent effusion rate measurements, temperature programmed desorption (TPD) measurements, and temperature dependent absorbance spectra. Computational methods include molecular mechanics, molecular dynamics, and the density functional theory. The theoretical model used for entropy estimation is also discussed.

Chapter 3 describes the driving forces of molecular self-assembly from a microscopic point of view. The first part gives a brief introduction of hydrogen bonds and the specific hydrogen bond interactions involved in this work. The second part introduces halogen bonds and illustrates the halogen-halogen interaction involved in this thesis. The third part introduces types of molecule-substrate interaction and the current research status.

In Chapter 4, terephthalic acid (TPA) self-assembly at the nonanoic acid (9A)-graphite interface is studied as a model system to develop a complete thermodynamic picture of self-assembly.[16] Precise enthalpy values were derived using independently obtained experimental and theoretical Born-Haber cycles. Every individual enthalpy difference, as well as the total enthalpy change of self-assembly from the solution phase into an adsorbed monolayer was quantified independently by both experimental and theoretical methods. In addition, entropy contributions were compared to the derived enthalpy gain to achieve a complete thermodynamic view. This approach reveals that the solvation of TPA in 9A lowers the entropy cost and renders the monolayer self-assembly into a thermodynamically favored process. In addition, the reversible thermal desorption of TPA at the 9A-graphite interface was observed and was studied using the Born-Haber cycle.

In Chapter 5, the Born–Haber cycle is applied to the monolayer self-assembly of 4,4’-stilbenedicarboxylic acid (SDA) at the 9A-graphite interface.[17] A direct comparison of TPA and SDA is used to evaluate and quantify the contribution of the extended aromatic backbone to the stabilization of the monolayer at the 9A–graphite interface.

In Chapter 6, hexabromotriphenylene (HBTP) is utilized as a model system for a quantitative understanding of the halogen bond mediated self-assembly.[45] In this case, the overall enthalpy change was assessed using a hybrid Born-Haber cycle. The enthalpy of the solid phase was indirectly determined by experimentally obtained sublimation enthalpy and dissolution enthalpy. On the other hand, the binding enthalpy of the HBTP monolayer on graphite in vacuum was obtained by independently assessing intermolecular interactions and graphite-molecule interaction. Both interactions are obtained using DFT simulations based on experimentally obtained lattice parameters. Comparison with theoretical entropy estimates suggests a negligible entropy influence of solvation on HBTP in 7A. From simulations of HBTP–7A binding enthalpy, a completely different solvation model compared to dicarboxylic acids is proposed to explain the obtained critical concentration.

Chapter 1: Scanning Tunneling Microscope

Introduction

The scanning tunneling microscope (STM), invented in 1982 by G. Binning and H. Rohrer at IBM Zürich [46], is a powerful instrument for obtaining real space information at the atomic level. It relies on the tunneling effect between a conductive sample and a metal tip, which leads to a tunneling current of electrons that flow between tip and sample. Under good experimental conditions in vacuum and with a sharp tip (ideally atomic level), the resolution can reach 0.1 nm laterally and 0.01 nm vertically [47].

Based on different instrument designs, the STM can work under various conditions, from ultra-high vacuum (UHV) to ambient [48, 49], from low temperatures close to 0K [50] to high temperatures up to a few hundred centigrade [51-53]. Although in UHV, the STM can work in a wider temperature range, reach higher resolution, and provide higher reproducibility, ambient STM is also frequently employed in surface science, especially at the liquid-solid interface [9, 54]. Solutions are of special interest for studying entropy effects and dynamic behaviors. In this thesis, non-conductive nonanoic acid and heptanoic acid were used as the solvents to work at the liquid-solid interface. In this chapter, a theoretical description will be given and the experimental setup will be discussed.

1.1 Theoretical description

At first, a theoretical description of quantum tunneling will be given using a simplified one-dimensional model with a rechtangular barrier. In the following sections, more elaborate theories comprising Bardeen’s perturbation theory and Tersoff-Hamman are introduced. A general overview of more sophisticated interpretations of STM images is given in the last section.

1.1.1 Simplified one dimensional model

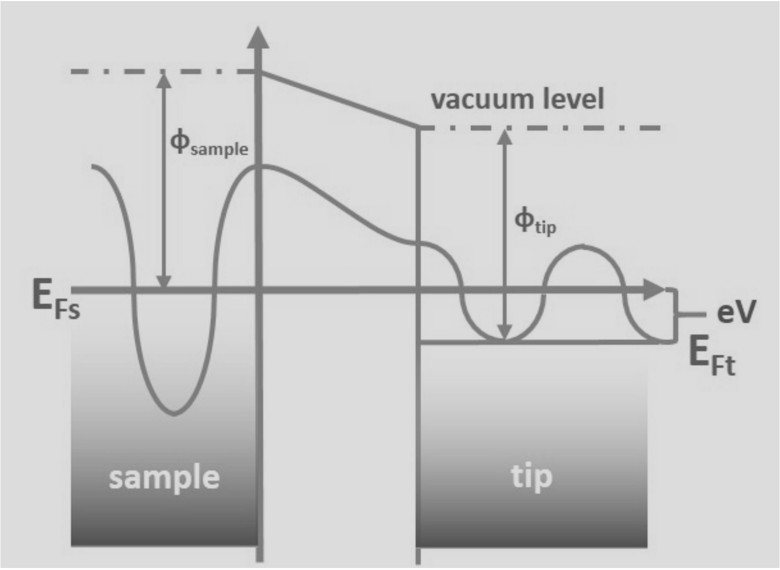

Figure 1.1. the schematic of a simplified quantum tunneling model between two metal electrodes. The work function of sample ϕ_{sample} and ϕ_{tip} is defined as the energy difference between vacuum level and each Fermi level. V is the applied tunneling voltage V between the tip and the sample. Electrons tunnel from sample to tip when a negative voltage is applied to the sample. Adapted from literature [55-57].

STM uses the quantum mechanical tunneling effect. The simplest theoretical description is the one dimension rectangular potential barrier [58, 59]. Electrons can penetrate a classically impenetrable potential barrier. When a metal tip is close enough to a conducting sample (~6 Å), the electron wave functions of the tip and the sample overlap with each other. It is possible for electrons of both tip and sample to tunnel through the barrier. When a bias voltage V is applied between the tip and the sample, as shown in Fig. 1.1, electrons from occupied states near the Fermi level of the sample will tunnel through the potential barrier into the empty tip states, resulting in a net tunneling current.

A simplest case is the stationary 1D tunneling problem, the wave function of electrons can be described by the Schrödinger equation:

$$\left[-\frac{\hbar^2}{2m}\frac{\partial^2}{\partial x^2}+U(x)\right]\Psi_n(x)=E_n\Psi_n(x) \tag{1.1.1}$$

Here $U(x)$ is the potential, m the electron mass, $\hbar$ the reduced Planck's constant, Ψ_n the wave function of n^th^ state, and E_n the corresponding energy.

If the barrier is rechtangular, i.e. $U(x)=U(0)=U$, for $0< x < d$. d is the width of the potential barrier.

For $E_n < U$, i.e. when electron energy is lower than the barrier, normally taken identical to the vacuum work function, wave function within the potential barrier $0< x < d$ can be approximated as:

$$\Psi_n(x) = \Psi_n(0)(e^{-\kappa x} + Re^{\kappa x}) \tag{1.1.2}$$

$\kappa = \sqrt{\frac{2m(U-E_n)}{\hbar^2}}$ is the decay constant of the wave function.

For electrons near the Fermi level, $U - E_F = \Phi$, i.e. the vacuum work function. Here it is assumed the work function is the same for the sample and the tip for simplicity. Accordingly, the decay constant is rewritten as $\kappa = \sqrt{2m\Phi}/\hbar$.

The probability P of tunneling is proportional to the square of the wave function at x=d, $|\Psi_n(d)|^2$, i.e.

$$\mathrm{P} \propto |\Psi_n(0)|^2 e^{-2\kappa d} \tag{1.1.3}$$

The exponential dependence implies that the tunneling probability is very sensitive to barrier width d and the vacuum work function Φ.

When a bias voltage is applied, where $eV < \Phi$, electrons with their energy between E_F and $E_F - eV$ can tunnel through the potential barrier. Accordingly, tunneling current I_T is proportional to the summation over all contributing states:

$$I_T \propto \sum_{E_n=E_F-eV}^{E_F} |\Psi_n(0)|^2 \, e^{-2\kappa d} \tag{1.1.4}$$

If the bias voltage is small enough, i.e. $eV \ll \Phi$, I_T can be rewritten using the local density of states (LDOS) at Fermi level:

$$I_T \propto V\rho_s(0, E_F)e^{-2\kappa d} \tag{1.1.5}$$

Here $\rho_s(x, E_F) \equiv \frac{1}{eV}\sum_{E_n=E_F-eV}^{E_F}|\Psi_n(x)|^2$ is the local density of states.

According to equation (1.1.5), I_T is exponentially dependent on tip-sample distance d, allowing sensitive detection of the corrugation of electronic states.

1.1.2 Time dependent perturbation theory

The simplified one-dimensional model is able to describe tunneling in principle. However, for the three-dimensional tunneling problem in STM, a more accurate theory is required. Since STM has been invented, two main theories have been successfully applied to explain experimental results, i.e. the transfer Hamiltonian method based on time dependent perturbation theory, and the elastic scattering quantum chemistry method. In the transfer Hamiltonian method, tip and sample are considered to be independent of each other, with only weak coupling interaction. The total Hamiltonian is considered as the sum of H_0 without coupling and a coupling perturbation $H^T(t)$. In 1961, this approach was first applied to explain a superconductor tunneling junction by Bardeen [60]. In STM, tip and sample can be treated as two independent systems with coupling treated as perturbation. The coupling via tunneling is assumed to be weak enough so that the tunneling junction can be treated as a perturbation. Tip states are orthogonal to sample states. Electron-electron interactions are ignored, and occupation probabilities for electrons in the tip and in the sample are independent from each other. The occupation probability can be described by the Fermi-Dirac statistics. If we assume that the Hamiltonians of tip and sample are H_s and H_t, respectively, the total Hamiltonian can be written as $H=H_s+H_t+H_{tr}$. Tip states and sample states are described by the Schrödinger equation in each subsystem.

The tunneling probability from tip state $|t\rangle$ to sample state $|s\rangle$ state is only determined by the perturbation factor, given by:

$$R_{t\to s} = \frac{2\pi}{\hbar}|M_{ts}|^2\delta(E_t - E_s) \tag{1.1.6}$$

M_{ts} is the matrix element of the perturbation potential between states $|t\rangle$ and $|s\rangle$. It can be calculated by integration over a surface dividing the tip and sample:

$$M_{ts} = \frac{\hbar^2}{2m}\int [\Psi_t^*(\vec{r})\nabla\Psi_s(\vec{r}) - \Psi_t^*(\vec{r})\nabla\Psi_s(\vec{r})]d^2\,\vec{r} \tag{1.1.7}$$

In 1993, C. J. Chen *et al*. proposed a modified Bardeen approach (MBA) to explain a real STM system. The net tunneling current was given by [61]:

$$I_{t\to s} = \frac{2\pi e}{\hbar}\int |M_{st}|^2\,\rho_t(E - eV)\rho_s(E)f_t(E - eV)[1 - f_s(E)]dE \tag{1.1.8}$$

Here, the occupation probability of electrons to each state is given by a Fermi distribution function $f(E) = \frac{1}{e^{\frac{E-E_F}{k_BT}}+1}$. $\rho_t(E)$ and $\rho_s(E)$ are the local density of states (LDOS). Electrons from occupied states (ρ_t, f_t) of the tip can tunnel into unoccupied sample states (ρ_s, $1\text{-}f_s$). For a very low temperature $T\to 0$K and small bias voltage, Fermi distribution function is approximately a step function. With this assumption, the net tunneling current is simplified to:

$$I_T = \frac{2\pi e}{\hbar}\int_0^{eV} \rho_t(E_F - eV + E)\rho_s(E_F + E)\,|M_{st}|^2 dE \tag{1.1.9}$$

If one assumes the tunneling matrix element does not change in the integration range, and the LDOS of the tip is constant near its Fermi level, the tunneling current is simplified to be proportional to the LDOS of the sample, given by:

$$I_T \propto V \cdot \rho_s(E_F) \tag{1.1.10}$$

From equation (1.10), one can see that the spatial dependence of the tunneling current reveals the LDOS at the Fermi level on the sample surface.

1.1.3 Tersoff-Hamann approximation

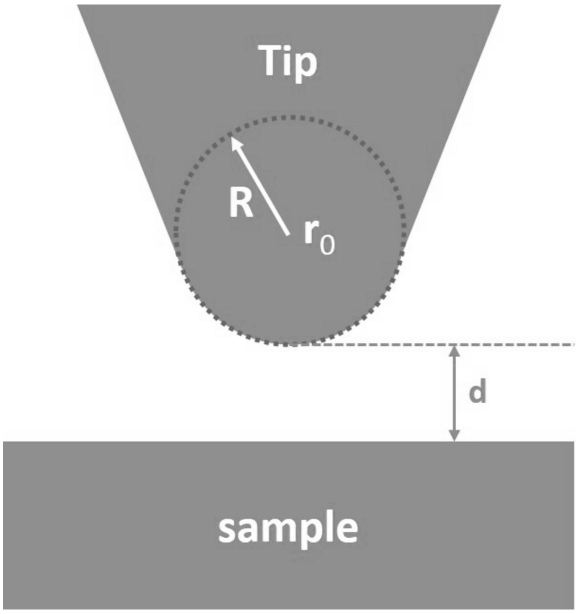

Figure 1.2. Tip model defined by Tersoff and Hamann. Only s-states of the tip are considered. *r₀* is the position of the tip centre, *R* the radius of the tip curvature, *d* the distance between tip and sample, adapted from literature [57, 62].

For simplicity, it is often assumed that the LDOS of the tip does not influence the STM image. After STM was invented, J. Tersoff and D. R. Hammann proposed a simplified tip model [62, 63], where the tip is assumed to be a local spherical potential well with a radius *R*, as depicted in Fig. 1.2. In this model, only *s* states of the tip are considered. Therefore, tunneling matrix elements are given by:

$$M_{st} = \frac{2\pi\hbar^2}{m\kappa}\Omega_{tip}^{-1/2}\kappa R e^{\kappa R}\Psi_t(\overrightarrow{r_0}) \tag{1.1.11}$$

Ω_{tip} is the volume of the spherical tip, $\overrightarrow{r_0}$ is the position of the tip center, *R* the radius of the tip curvature. Hence, when a bias voltage *V* is applied, the tunneling current can be stated as,

$$I_T \propto \int_{E_F}^{E_F+eV} \rho_s(\overrightarrow{r_0}, E)\, dE \tag{1.1.12}$$

$$\rho_s(\overrightarrow{r_0}, E) \equiv \sum_i |\Psi_i(\overrightarrow{r_0})|^2 \delta(E_i - E_F) \propto \rho_s(E) e^{-\frac{2d}{\hbar}\sqrt{2m[(\Phi - E)+eV]}} \tag{1.1.13}$$

In the above formulas, I_T is the tunneling current, $\rho_s(\overrightarrow{r_0}, E)$ is the LDOS, d is the gap distance, and Φ is the vacuum work function. If we assume $\rho_s(\overrightarrow{r_0}, E)$ does not change near E_F, then $I_T \propto \rho_s(\overrightarrow{r_0}, E_F)$, i.e. tunneling current is proportional to the LDOS at the Fermi level at the tip centre.

1.1.4 More sophisticated theories

Early STM studies investigated the atomic structures of single crystal surfaces like Al(111), Pt(100), Si(111), graphite, etc.[64-66]. Subsequent studies focused on the adsorption of small atoms and isolated molecules [67, 68]. For molecular adsorbates, it has been demonstrated that STM images reveal the electronic states of the adsorbate rather than the geometric structure [69-72]. A theoretical description based on the Jellium model is proposed by Lang (1985) using Bardeen's approximation to calculate the tunneling current between two metal electrodes with an adsorbate in between. The tunneling current can be enhanced or reduced by electron states of adsorbates coupling with states close to the Fermi level of metal electrodes [73, 74]. Similar conclusions can also be drawn from the Tersoff-Hamann model [62, 63]. Later on, Eigler (1991) gives a quantitative demonstration of STM height measurement of Xe on Ni(110) by comparison of experiments with calculations based on the Jellium model [75].

To explain more general cases like semiconductors, molecular monolayers, scanning tunneling spectroscopy etc., more sophisticated models of tip, including tip properties, were proposed. A popular model was proposed by C. J. Chen in 1991 [76, 77]. He extended the *s*-wave tip in the Tersoff-Hamann model to linear combination of complete sets of eigenfunctions. Localized surface states of both the tip and the sample are used to calculate the tunneling current. For instance, d_{z2} states of W or Pt/Ir tips overlap with the sp^3 dangling bonds of the sample surface. Therefore, much higher lateral resolution can be obtained than the Fermi-Level LDOS [78].

In 1995, Hallmark and Chian used an extended Hückel Theory to calculate Hückel orbitals of molecules adsorbed on substrate surfaces [70]. In their work, the relation between STM images and contour maps of LDOS was successfully revealed. Recently, Sautet and Joachim proposed an approach based on Electron Scattering Quantum Chemistry (ESQC) [79]. The tunneling effect of electrons, through an adsorbate on a substrate surface, is treated as a scattering process in a periodic bulk crystal with a defect [80, 81]. This method uses a generalized Landau formula based on quantum chemistry calculations to obtain the entire Hamiltonian of the tunneling junction [79, 82]. Accompanied by the development of computational power, more sophisticated methods are used to simulate the tip, adsorbates and the substrate at different conditions, but these will not be discussed here [83].

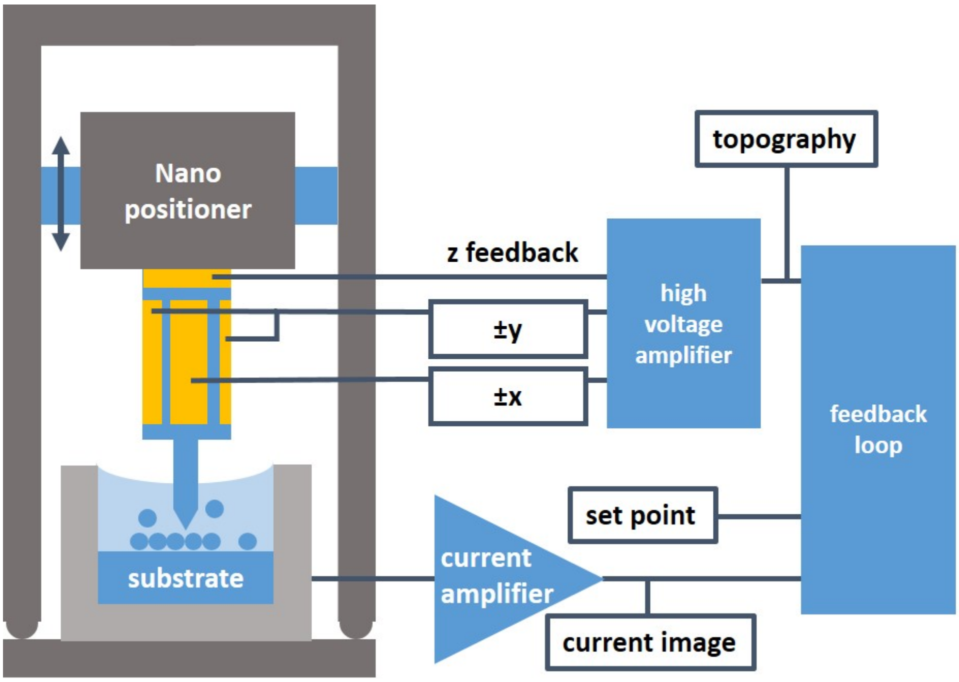

Figure 1.3. Sketch of the STM setup. Scanning is performed by a piezo tube. The substrate is put in a specially designed sample holder to prevent outflow of the solution. Adapted from literatures [55, 57].

A schematic setup of the STM used in this dissertation is illustrated in Fig. 1.3. It consists mainly of a piezoelectric scanner, a nano-positioner, a current amplifier, the feedback loop, a high voltage amplifier, and the controlling units. In the scheme, the central part is the single tube piezoelectric scanner, which uses four segmented outer electrodes to control the motions of X/Y directions, and one inner electrode to control the motion of the Z direction. Single tube scanners are the most widely applied scanner used to image small areas [84]. On the one hand, it is small and hence easy to assemble. On the other hand, it is rigid against vibrations.

A further important component is a modified ANPz50 linear positioner from the attocube systems AG, used for the coarse approach. The operation principle is based on the so-called stick-slip effect. First, the axis of the positioner extends slowly by applying a voltage ramp to the attached piezo. Meanwhile, the clamped nano positioner is transported by static friction. Accompanied by a following fast movement of the axis in the opposite direction, the positioner slips over the axis for one-step, because of the great inertia. Repetition of the process allows a movement in one direction with precisely controlled steps of ~100 nm.

The approach is accomplished by the combination of the scanning piezo and nano-positioner. A slow voltage ramp is applied to the Z electrode until the piezo is fully extended. If no tunneling current is detected, it will be fully contracted and the nano positioner moves several steps forward. The procedure is iterated until a tunneling current is detected.

When the tip reaches tunneling range, the feedback loop can be switched on again to extend the z-piezo. The tunneling current is amplified and transformed into a voltage by a sum of $10^9\,V/A$. Accordingly, a tunneling current in the range of pA can be detected. The measured current and the set point current are used as the input of the feedback. Accordingly, the feedback loop extends or contracts the piezo tube in Z direction to eliminate the difference between the measured tunneling current and the set point current. This is accomplished by applying voltage to the inner segment with respect to the outer four segments. The piezo tube allows one to control the distance between the tip and the sample with an accuracy of ~pm. The extension of the piezotube is linearly dependent on the applied bias voltage. When applying a voltage to the outer segments, scanning tube is bent to perform raster scanning along the sample surface. Expansion and contraction of the piezo tube are recorded with respect to X/Y coordinates and accordingly a topography image is acquired.

A very sharp tip is a critical factor for high lateral resolution. Electrochemical etched Tungsten tips were most favorable in UHV conditions since sharper tips and reproducible results could be obtained. However, for working in ambient conditions, mechanically cut Pt/Ir tips are more favorable owing to their resistance to oxidation. Moreover, a well-prepared Pt/Ir tip contains asperities on the tip surface, allowing even better atomic resolution than Tungsten tips. However, a disadvantage that accompanies with asperities is their limitations when working on surfaces with higher degrees of roughness [47].

Another key factor of getting a high quality STM image is to eliminate or isolate the noise from the signal, e.g. mechanical noises, electric noises, temperature fluctuations, and so on. In this work, mechanical noises are eliminated by spring suspension, eddy current damping, and an air damped table. Electrical noise is mainly eliminated by grounding the system in a proper way and operating inside a metal box for shielding. Temperature fluctuations, however, can only be diminished by lowering the temperature, which is impossible for ambient STM. For liquid-solid STM, additional problems are created by the concentration changes of the solution caused by spilling. In this work, the spilling is avoided using a rimmed sample holder with a relatively high solution volume (~40 µL), as depicted in Fig. 1.3.

Chapter 2: Thermodynamic Methods

Enthalpy differences between bulk crystals, graphite supported monolayers, isolated molecules in vacuum, and molecules in solution were assessed by using established experimental techniques, computational methods, or a hybrid of both. In this chapter, all experimental and computational methods used in this thesis are discussed in detail. Experimental methods, including temperature-dependent effusion rate measurements, temperature programmed desorption, and temperature-dependent UV-vis absorption spectroscopy are introduced in the first three sections. Computational methods, including molecular mechanics (MM), molecular dynamics (MD), and density functional theory (DFT) using both empirical dispersion correction and van der Waals functionals are discussed in the following section.*

In addition, theoretical models that were used to estimate entropies of self-assembly are discussed in the last section. Assessment of the dewetting entropy related to a self-assembled 9A solvent monolayer is based on the literature value of melting entropy, and hence will not be discussed further here [85].

2.1 Sublimation enthalpy

The binding enthalpy difference between bulk crystals and isolated molecules in vacuum, i.e. the enthalpy of sublimation, is obtained by temperature-dependent effusion rate measurements. This is accomplished using a combination of Knudsen cell and Quartz Crystal Microbalance (QCMB) designed by Gutzler *et al.* [86]. This also provides an important insight for predicting the effusion rate of compounds, which is an extremely important parameter for organic molecular-beam epitaxy (OMBE).

A detailed theoretical description of the QCMB and a detailed discussion of the thermodynamic basis of the measurement are provided in the first subsection. Later, the experimental setup as used in this thesis is discussed in the following subsection.

2.1.1 Theoretical description

QCMB is a sensitive in-situ analytical method used to monitor tiny mass changes based on the piezoelectric properties of quartz crystals. A typical QCMB instrument consists of an electrical oscillator circuit, a frequency counter, and a piezoelectric crystal. In this work, an AT cut shear force quartz crystal is used as the acoustic resonator and energy transformer. When an electric AC field is applied between the gold electrodes coated on both sides of the quartz surface, the crystal will perform a shear oscillation due to the inverse piezoelectric effect. The frequency of the AC voltage is adjusted so that the circuit is operated at the eigenfrequency of the crystal. This frequency shifts when the mass loaded on the quartz crystal changes. Eigenfrequency shifts induced by rigid adsorbates on the piezoelectric crystal can be described by the Sauerbrey equation [87],

---

* Natalia Martsinovich (University of Sheffield, UK) is gratefully acknowledged for doing all the simulations.

$$\Delta m_{QCMB} = -\frac{A_Q v_{trans} \rho_Q}{2 f_0^2} \Delta \mathrm{f} \tag{2.1.1}$$

Δf is the frequency shift; f_0 the nominal eigenfrequency of the quartz crystal (6 MHz); Δm_{QCMB} the mass of the loaded adsorbates; A_Q the total adsorption area; ρ_Q the density of quartz (2.65 g·cm^{-3}); v_{trans} the propagation velocity of an elastic transversal wave perpendicular to the quartz crystal surface (3340 kHz mm). The Sauerbrey equation can describe the frequency shift very well when $\Delta f \ll f_0$. In this thesis, the total eigenfrequency shift during the measurement is about $1 \times 10^4 \mathrm{Hz} \ll 6\mathrm{MHz} = f_0$ for each compound. Accordingly the effusion rate can be approximated by equation (2.1.1), when the sticking coefficient is constant, i.e. the effusion rate is proportional to the mass of the loaded adsorbates on the QCMB Δm_{QCMB}. According to equation (2.1.1), Δf is negative, i.e. the eigenfrequency of the quartz crystal shifts to a lower value when adsorbates are loaded onto the quartz crystal.

For a constant temperature of the crucible in a Knudsen cell and with a large enough mean free path, the effusion rate through the opening of the Knudsen cell is given by [88],

$$\Delta m_{crucible}/\Delta t = -\frac{1}{4}\frac{p(T)}{RT}\langle v\rangle \mathrm{A_o} \tag{2.1.2}$$

Here p is the saturated vapor pressure of the compound in the Knudsen cell at T; $\Delta m_{crucible}$ is the mass of molecules coming out of the crucible. $\mathrm{A_o}$ is the area of the cell opening; $\langle v\rangle$ is the average gas velocity.

$\langle v\rangle$ can be deduced from the Maxwell-Boltzmann distribution as $\sqrt{8k_BT/\pi m_{molc}}$ where m_{molc} is the mass of the compound and k_B is the Boltzmann constant. Accordingly, the effusion rate is given by,

$$\Delta m_{crucible}/\Delta t \propto T^{-\frac{1}{2}} p(T) \tag{2.1.3}$$

$p(T)$ can be approximated as proportional to $\Delta m_{crucible}/\Delta t$ within a relatively small temperature range. On the one hand, $p(T)$ depends exponentially on temperature, and dominates the right side of equation (2.1.3). On the other hand, $T^{-\frac{1}{2}}$ does not vary much within the required temperature range. Taking the used compound TPA as an example, the crucible temperature ranges from 375 K to 400 K. Accordingly, the prefactor $T^{-1/2}$ causes a margin error of only ~4% in the proportionality between effusion rate and vapor pressure. Consequently, for a narrow T range, the equation (2.1.3) can be approximated as,

$$\Delta m_{crucible}/\Delta t \propto p(T) \tag{2.1.4}$$

For a constant sticking coefficient, the effusion rate from the crucible $\Delta m_{crucible}/\Delta t$ is proportional to the rate of mass loaded onto the QCMB, accordingly to the eigenfrequency decline rate $\Delta f/\Delta t$. Hence, equation (2.1.4) is transformed into,

$$\Delta f/\Delta t \propto p(T) \tag{2.1.5}$$

The phase transition from the solid state to the gas phase is a kinetic process, but the rate is determined by the vapor pressure which can be approximated by the Clausius-Clapeyron relation. Therefore, the change of vapor pressure differential with respect to temperature is described as:

$$\frac{dp}{dT} = \frac{L}{T\Delta v} \tag{2.1.6}$$

Here L is the specific heat of the phase transition, i.e. the enthalpy of sublimation ΔH_{sub}; Δv is the volume change of the phase transition. For the sublimation process, the volume of the solid state can be neglected in comparison to the volume of the gas phase. Accordingly, Δv can be approximated as the volume of gas phase V, which is approximated by the ideal gas equation as nRT/p. n is the amount of the gas. Equation (2.1.6) is then simplified as,

$$\frac{dp}{dT} = \frac{p \cdot \Delta H_{sub}}{nRT^2} \tag{2.1.7}$$

The relation between p and ΔH_{sub} is then obtained by the integration of equation (2.1.7):

$$p \propto e^{\frac{\Delta H_{sub}}{RT}} \tag{2.1.8}$$

According to equation (2.1.5), the vapor pressure is approximated directly proportional to the eigenfrequency decline rate $\Delta f/\Delta t$. Equation (2.1.8) can be rewritten as,

$$\Delta f/\Delta t \propto e^{\frac{\Delta H_{sub}}{RT}} \tag{2.1.9}$$

Hence, ΔH_{sub} can be obtained by measuring $\Delta f/\Delta t$ vs. T, and derived from a corresponding Arrhenius plot of $ln|\Delta f/\Delta t|$vs.$1/T$.

2.1.2 Experimental setup

Knudsen cells are abundantly applied in OMBE due to their high reproducibility related to temperature stability. The used Knudsen effusion cell is combined with a quartz crystal microbalance (QCMB, crystal diameter 1.4 cm, nominal eigenfrequency 6.0 MHz) to directly monitor the effusion rate of the molecule, as depicted in Fig. 2.1 a. The Knudsen cell consists of a molybdenum crucible, a heating filament, and a QCMB integrated into the shutter and connected with a BNC feedthrough. The Knudsen cell is operated inside a high vacuum chamber pumped with a turbo molecular pump and an oil rotary fore pump to keep the pressure in the range of 10^{-7} mbar. The crucible temperature was measured with a type K thermocouple and held constant with a Eurotherm 2416 temperature controller (Invensys Systems GmbH, Limburg an der Lahn). Before every measurement, the crucible is degassed to avoid contaminating of the compounds studied. A commercial circuitry (Q-pod, INFICON) thickness monitor was used to drive and readout the QCMB.

Thereafter, $\Delta f/\Delta t$ is recorded for a series of crucible temperatures with an increment 5°C. The crucible temperature was varied between 100 °C and 120 °C for TPA crystal, between 125 °C and 165 °C for SDA crystal, and between 225 °C and 270 °C for HBTP crystal. Accordingly, ΔH_{sub} can be derived from the corresponding Arrhenius plot. In Fig. 2.1 b and c, 4,4'-stilbenedicarboxylic acid (SDA) bulk material was used as an example to illustrate how ΔH_{sub} was derived from the $\Delta f/\Delta t$ data. The measured $\Delta f/\Delta t$ with respect to temperature is depicted in Fig. 2.1 b. By plotting $ln|\Delta f/\Delta t|$ vs. $1/RT$, ΔH_{sub} is obtained from the slope. As depicted in Fig. 2.1 c, each data point is obtained using the slope of each effusion rate curve.

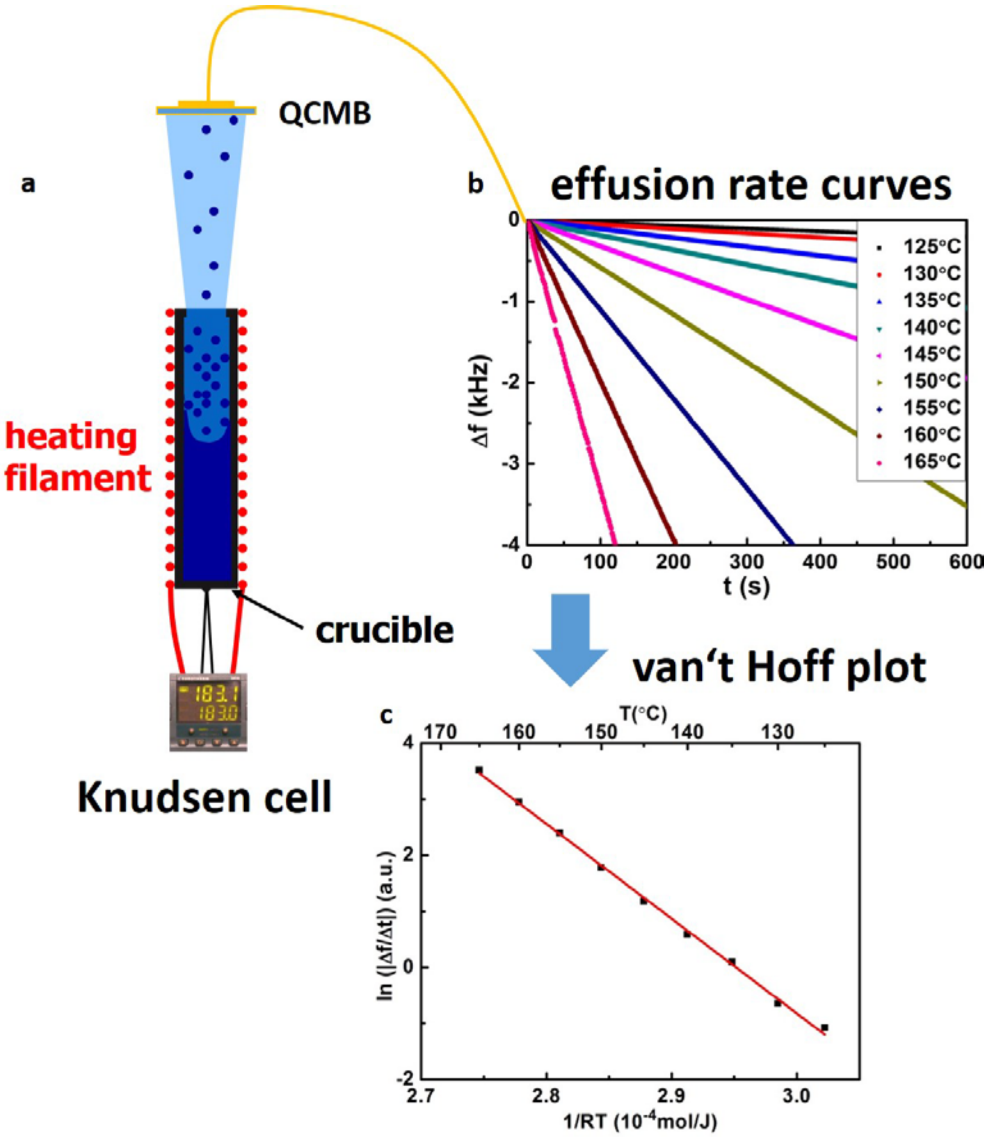

Figure 2.1. (a) experimental setup of the sublimation enthalpy measurement; a crucible is surrounded by a heating filament; the temperature of the crucible is monitored by a type K thermocouple mounted at the bottom. A Eurotherm 2416 controlling unit is used to monitor and control the temperature of the crucible. (b) The eigenfrequency shift (Δf) is recorded as a function of time by the electronics of the QCMB for a series of crucible temperatures. (c) For the corresponding van't Hoff plot, each data point corresponds to the slope of an effusion rate curve in (b). (b) and (c) are the sublimation measurements for SDA, adapted from publication 2 (cf. section 5.4) [17].

2.2 Total monolayer binding enthalpy

In this thesis, the total binding enthalpy of molecules in a surface supported monolayer with respect to isolated molecules in a vacuum was obtained by temperature programmed desorption (TPD) measurements.

TPD has been extensively used to determine the kinetic and thermodynamic parameters of desorption or decomposition reactions on surfaces [89-93]. In a typical TPD measurement, the temperature of an adsorbate covered surface is usually controlled to increase linearly with time. Owing to the thermal activation, molecules or atoms desorb from the surface and then are detected in the gas phase. TPD spectra are obtained by recording the number of atoms or molecules desorbing from the substrate vs. temperature. In principle, any parameter that is proportional to the number of the desorbed adsorbates can be used to monitor the desorption rate, e.g. thermal conductivity [94], work function, and so on. Due to the advantages of the high sensitivity and straightforwardness of mass selective detection of adsorbates, partial pressure measured by mass spectroscopy is utilized in most TPD measurements in ultra-high vacuum (UHV) [95-97]. In a continuously pumped UHV system, the desorption rate of atoms or molecules from the surface are approximated to be proportional to the corresponding partial pressure in the gas phase. By recording the partial pressure of the desorbing substance from the substrate, a thermal desorption spectrum can be obtained with respect to time and temperature.

A theoretical description of desorption will be given in the first subsection, and an experimental setup will be described in the following subsection. In the last subsection, the different methods used to evaluate TPD spectra are discussed in detail.

2.2.1 Theoretical description of desorption

Adsorption takes place when interactions with the surface are strong enough to overcome the related entropy loss. Based on the surface-molecule interactions, adsorption is categorized into physisorption and chemisorption. For inert substrates, substrate-molecule interactions are mainly long-range dispersion forces, and no chemical bonds are formed during adsorption. Hence, molecular orbitals and structures of the adsorbate are not perturbed by the substrate. This kind of adsorption is typically spontaneous and reversible, and is termed as physisorption. Greater details will be discussed in Chapter 3. On the other hand, if there are chemical bonds formed between adsorbates and the substrate, chemisorption takes place. In this case, adsorbates usually bond with the surface via covalent or ionic bonds. Chemisorption is normally irreversible. The corresponding surface binding energy is typically one order of magnitude higher than in the case of physisorption. However, since only physisorption takes place in the systems studied, chemisorption will not be discussed further in this thesis [98].

Desorption and adsorption processes can be considered as the reverse of each other. Hence, both can be described using similar thermodynamic parameters. Most of the methods used to derive desorption energies are based on the rate law of nth order desorption [99, 100],

$$R_{des} = -\frac{d\Theta}{dt} = k_n \cdot \Theta^n \tag{2.2.1}$$

Where the temperature dependent rate constant k_n is given by an Arrhenius equation,

$$k_n = \nu_n \cdot exp\left[-\frac{\Delta E_{des}}{RT}\right] \tag{2.2.2}$$

Combining equations (2.2.1) and (2.2.2) yields the so-called Polanyi-Wigner equation. All relevant parameters can depend on coverage. Accordingly, this is stated as,

$$R_{des} = -\frac{d\Theta}{dt} = \nu(\Theta)_n \cdot \Theta^{n(\Theta)} \cdot exp\left[-\frac{\Delta E_{des}(\Theta)}{RT}\right] \tag{2.2.3}$$

However, the desorption energy in most cases depends on temperature. This is because thermal desorption is more likely a dynamic method that provides information far below the equilibrium temperature. Therefore, the Polanyi-Wigner equation is only an approximate tool and not sufficient to analyze complex TPD spectra. Accordingly, the corresponding data analysis often requires the assistance of computational approaches, e.g. MC simulations [101].

2.2.2 Quadrupole mass spectrometer

Because of the small dimensions and the light weight, quadrupole mass spectrometers (QMS) are suitable for applications in vacuum chambers, e.g. leak detection, partial pressure measurements, and determining desorption or adsorption rates in vacuum, etc. In this thesis, a QMA 125 from Balzers equipped with a SEM was used for detection of the desorbing molecules at the strongest peak in the corresponding mass spectra. The desorbing TPA molecules were detected at 149 amu. For SDA, the mass peak at 179 amu was used for detection.

A QMS consists of three parts: an ion source, a quadrupole mass analyzer, and an ion detector. Ions are generated by electron impact ionization. Electrons are emitted from an electrically heated filament, and are accelerated by a potential difference between the source and the impact region. Molecules entering the impact area are directly ionized or dissociated into fragmented ions upon electron impact. After that, ions with different mass to charge ratio (*m/Ze*) enter the quadrupole mass analyzer.

The filter system of a quadrupole mass analyzer consists of four parallel rods arranged symmetrically around the axis of the system. Opposite rods are electrically connected. A potential difference of $U + V \cdot cos(\omega t)$ is applied between the two pairs of connected rods. Accordingly, the potential distribution near the axis of the system is given by,

$$\Phi = [U + V cos(\omega t)] \frac{x^2 + y^2}{2{r_0}^2} \tag{2.2.4}$$

Corresponding differential ion motions are given by,

$$\frac{d^2x}{dt^2} + \frac{\omega^2}{4}[a + 2q cos(\omega t)] = 0 \tag{2.2.5}$$

$$\frac{d^2y}{dt^2} - \frac{\omega^2}{4}[a + 2q cos(\omega t)] = 0 \tag{2.2.6}$$

$$\frac{d^2z}{dt^2} = 0 \tag{2.2.7}$$

Here, $a = \frac{8eU}{m{r_0}^2}$ and $q = \frac{4eV}{m{r_0}^2}$ are the stability parameters.

For a given set of *U*, *V*, and ω values, only ions with certain *m/Ze* value can travel through the filter with stable trajectories. However, molecules can be doubly or triply ionized. Accordingly, compounds with larger molecular mass than the effective mass range of the QMS (200 amu in this work) can also be detected at half or one third of the molecular mass.

Particles passing through the mass filter are ultimately registered at the detector. Detection of the amount of passed ions is accomplished by measuring their charge (faraday cup) or counting the number of the ions (SEM). With the assistance of an electronic preamplifier and a SEM, an ion current of lower than 1 pA (10^7 ions a second) is detectable.

2.2.3 Experimental setup

The whole experimental setup for TPD measurements is mounted in a stainless steel Ultra-High Vacuum (UHV) chamber, as illustrated in Fig. 2.2. The chamber is pumped using a turbo molecular pump with a combination of a set of mechanical pumps and an ion getter pump. The graphite substrate is fixed on a sample holder with the possibility to tilt and rotate in different directions. This sample holder allows one to prepare the sample and perform TPD measurements in the same UHV chamber. For sample cleaning, graphite is first annealed from the backside at a surface temperature of 800 K for ～1 hour using the electron beam heating method (Fig. 2.2). A K-type thermocouple is fixed on the graphite surface to monitor and control the temperature again by a Eurotherm 2416 controller. After the graphite is annealed, the monolayer is prepared using the OMBE. Therefore, the evaporation rate can be monitored with a QCMB to get reproducible coverage, as discussed in section 2.1. Crucible temperature is again controlled by a Eurotherm 2416 controller. After the sample is prepared, it is rotated to point to the direction of the QMS to start the measurements. A closed-cycle helium cryostat with a copper rod and a copper strap conducting heat away from the sample holder allows a low starting temperature for TPD measurements. Linearly rising surface temperature is obtained by linearly increasing the set point temperature. Desorption rate vs. time is recorded by the mass spectrometer. Together with the recorded surface temperature vs. time, a TPD spectrum is obtained by a program written by Matthias Lischka using LabVIEW.

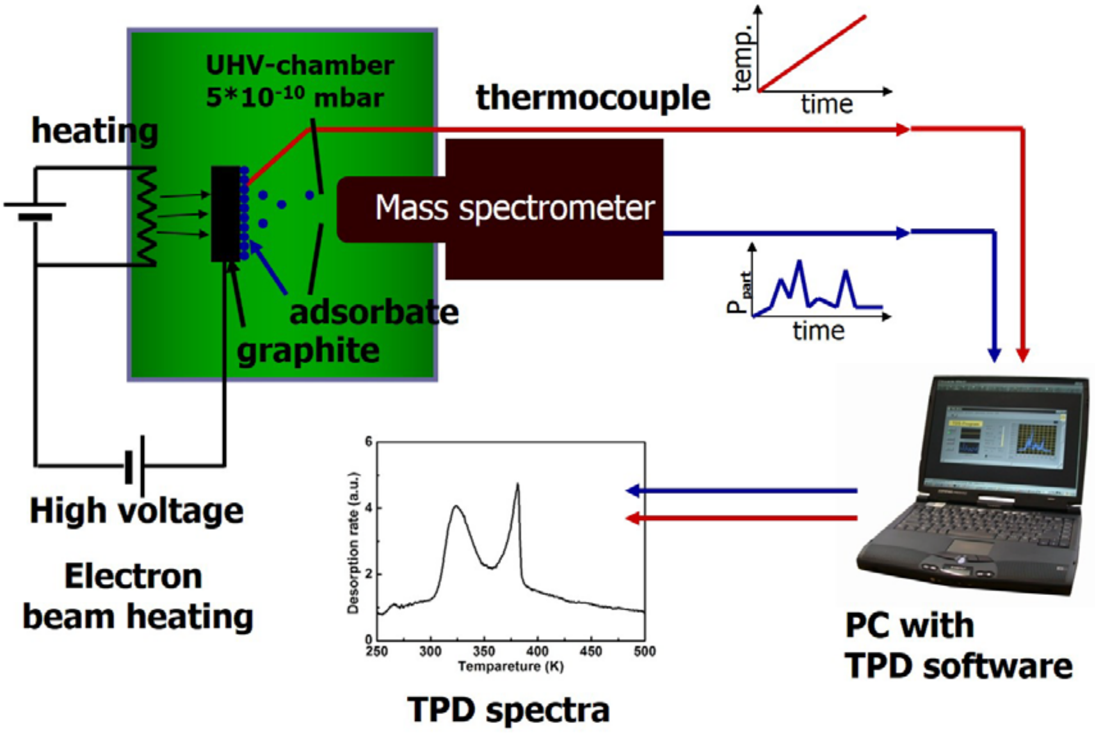
UHV-chamber
5*10-10 mbar
heating
thermocouple
temp.
time
Mass spectrometer
Ppart
time
adsorbate
graphite
High voltage
Electron beam heating
6
4
2
0
Desorption rate (a.u.)
250
300
350
400
450
500
Tempareture (K)
TPD spectra
PC with
TPD software

Figure 2.2. Experimental setup for TPD. The sample is mounted inside a stainless steel UHV chamber. Electron beam heating is used. A quadrupole mass spectrometer is used to monitor the desorption rate. Using the recorded desorption rate and programmed heating curve, the TPD spectra is obtained by plotting desorption rate vs. temperature, using a software written by Matthias Lischka with LabVIEW.

One of the most important prerequisites for accurate TPD measurements is to keep the temperature homogenous across the surface. One option is to decrease the heating rate such that the sample has enough time to remain in thermal equilibrium.

Another important prerequisite for a successful TPD measurement is the ultra-high vacuum (UHV), ideally in the range of 10^{-10} mbar to reduce background noise. On the other hand, the pumping rate should be high enough to avoid readsorption of adsorbates. A slow pumping rate causes broader peaks in the TPD spectra, which makes quantitative analyses or even qualitative estimations impossible. When the pumping rate is high enough, the detected signal in the mass spectrometer is approximated to be proportional to the desorption rate.

2.2.4 Analyzing TPD spectra

TPD spectra are mostly evaluated based on the Polanyi-Wigner equation (cf. section 2.2). Different approaches can be used to derive the desorption energy, e.g. heating rate variation method, Redhead method, leading edge method, complete analysis method, etc.

One of the most applied methods for analyzing TPD spectra is the heating rate variation method. This method is based on a series of TPD experiments conducted with different constant heating rates $\beta = dT/dt$. For all spectra, the initial coverage is kept constant. All thermodynamical parameters are assumed to be independent of coverage Θ. By plotting $ln(T_{max}^2/\beta)$ vs. $1/RT_{max}$, where T_{max} is the temperature of maximum desorption rate, the desorption energy ΔE_{des} can be derived for 0, 1st, and 2nd order desorption. In addition to the difficulty in keeping the coverage constant for different TPD measurements, this method also requires the prior assumption that ΔE_{des} and ν_n are independent of coverage which is in most cases not applicable. Another straightforward analysis method was proposed by Redhead [99, 102] and allows the derivation of ΔE_{des} by using only one TPD curve, $\Delta E_{des} \approx RT_{max}\left[\ln\left(\frac{\nu_1 T_{max}}{\beta}\right) - 3.64\right]$. Due to the simplicity of the Redhead method, it is applied intensively on thermal desorption of gases. However, the Redhead method is only applicable for 1st order desorption, where intermolecular interactions are negligible. In addition, it assumes that ν_1 is known and independent of coverage, which is in most cases wrong.

To derive ΔE_{des} without knowledge of desorption order, Habenschaden and Küppers proposed the so-called leading edge analysis method [103]. At the leading edge of a TPD spectrum, where coverage remains almost unchanged, ΔE_{des} can be derived from the logarithmic Polanyi-Wigner equation without knowing the desorption order. It has been reported by Liberman *et al*. that the leading edge of the desorption peak for CCl_4 desorbed from GaAs(110) is independent of coverage [104]. However, the leading edges of TPD spectra are often obscured by very strong background noise, which makes the evaluation in many cases unreliable.

To avoid all the above difficulties, the complete analysis method is used to derive the desorption energy in this work. On the one hand, it does not require the knowledge of the desorption order which we do not have. On the other hand, the background noise at the leading edge is significant in our TPD spectra [105]. Therefore, the leading edge method is not appropriate for our data. In the following, the principle of the complete analysis method is derived from the Polanyi-Wigner equation.

Taking the logarithm of the Polanyi-Wigner equation for a constant coverage gives the following relation,

$$\ln[R_{Des}(\Theta)] = \ln[\nu_n(\Theta)] + n\ln[\Theta] - \frac{\Delta E_{des}(\Theta)}{RT} \tag{2.2.8}$$

For a comparably high coverage $\Theta \rightarrow 1$, $\nu_n(\Theta)$, n and $\Delta E_{des}(\Theta)$ are assumed to be constant and independent of temperature. Consequently, for two different temperatures T_2 and T_1, the following relation can be derived:

$$\begin{aligned} \ln[R_{des}(\Theta)]_{T_2} - \ln[R_{des}(\Theta)]_{T_1} \\ = \left[\ln\nu_n(\Theta) + \mathrm{n}\ln[\Theta] - \frac{\Delta E_{des}(\Theta)}{RT_2}\right]_{T_2} - \left[\ln\nu_n(\Theta) + \mathrm{n}\ln[\Theta] - \frac{\Delta E_{des}(\Theta)}{RT_1}\right]_{T_1} \\ = \frac{\Delta E_{des}(\Theta)}{RT_1} - \frac{\Delta E_{des}(\Theta)}{RT_2} = \Delta E_{des}(\Theta)\cdot\left(\frac{1}{RT_1} - \frac{1}{RT_2}\right) \end{aligned} \tag{2.2.9}$$

Thereby, $\Delta E_{des}(\Theta)$ can be derived from the slope of $\ln R_{des}(\Theta)$ vs. $1/RT$. Hence, the desorption energy can be derived for a chosen coverage.

For a surface supported monolayer with pronounced intermolecular interactions, the desorption energy per molecule is related to the two-dimensional arrangement. Even for cases without polymorphism, $\Delta E_{des}(\Theta)$ is higher for molecules within the domain than molecules at domain boundaries. Therefore, $\Delta E_{des}(\Theta)$ of lower coverage, corresponding to higher temperatures, is lower compared to that of higher coverage. In addition, the background noise obscures the signal at the onset of the TPD spectra. Therefore, we utilize the data points at temperatures prior to the maximum desorption rate, but not at the onset of the spectra. In this region of the spectra, both the TPD signal and the surface coverage are still large.

The advantage of the complete analysis method is that it requires fewer assumptions and features the best accuracy among all methods. On the other hand, this method is quite time consuming and complicated.

Fig. 2.3 illustrates the TPD measurements of TPA monolayer on graphite surface (cf. section 4.4). TPA monolayers were deposited from a Knudsen cell with a crucible temperature of 110 °C for 15 minutes. These deposition parameters reproducibly yielded coverages just below one monolayer. For slightly longer deposition times multilayer peaks appeared in the desorption traces. During deposition the substrate was held at 300 K and cooled to 250 K prior to the desorption experiment with a closed cycle helium cooler. In the desorption experiment, the surface temperature was linearly ramped from 250 K up to 550 K by means of a temperature controller (Eurotherm 2416). Three sets of experiments were performed with three different heating rates of 0.25 K s^{-1}, 0.42 K s^{-1} and 0.84 K s^{-1}, corresponding TPD spectra are illustrated in Fig 2.3a. The coverage is obtained by integration of desorption rate over desorption time. Together with temperature vs. time, a set of diagrams of Θ vs. T can be derived from the original $R_{des}(\Theta)$ vs. T obtained at different heating rates and different initial coverages, as depicted in Fig. 2.3 b. For a chosen coverage, the corresponding temperature can be extracted from the $\Theta(T)$ curves. Accordingly, the corresponding $R_{des}(\Theta)$ can be read out from the corresponding TPD spectra in Fig. 2.3 a. In the end, $\Delta E_{des}(\Theta)$ is derived from the slope of plotting $\ln R_{des}(\Theta)$ vs. $1/RT$. The desorption energy is derived to be +140.2±9.5 kJ mol^{-1} per molecule as shown in Fig. 2.3 c.

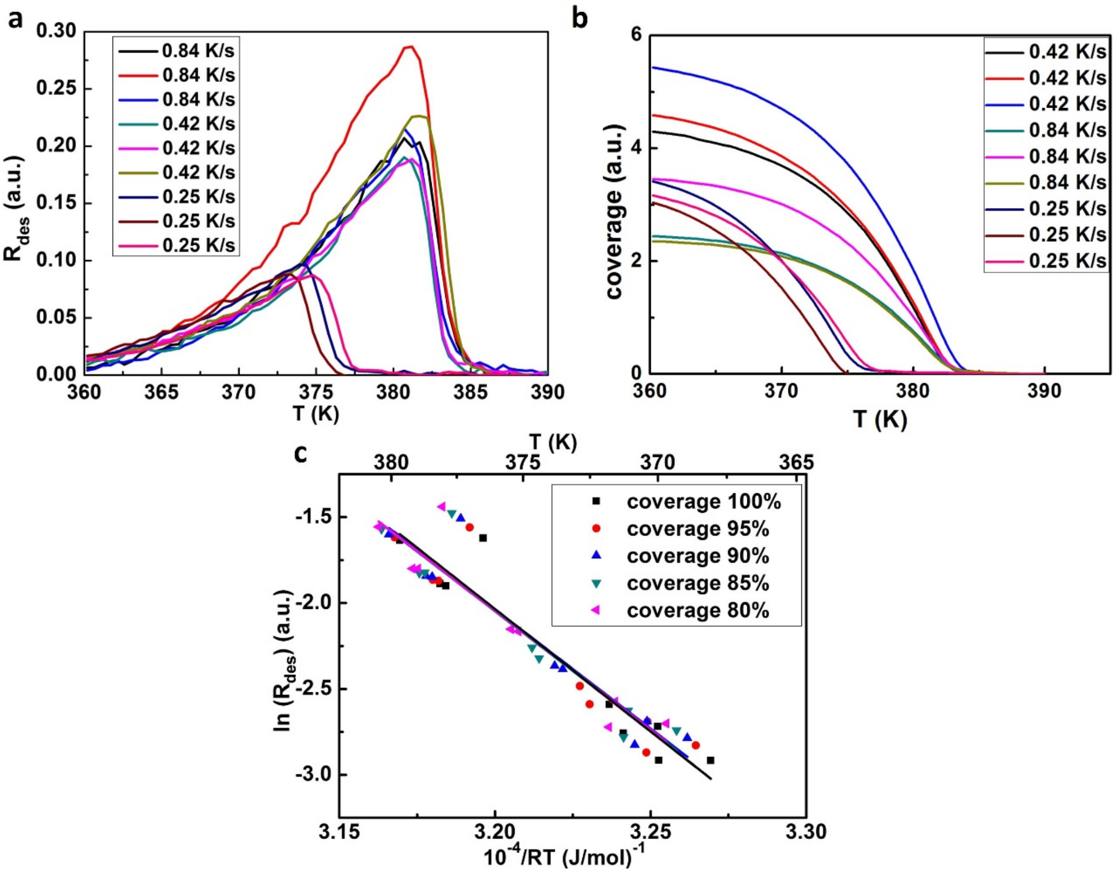

Figure 2.3. An example of TPD measurements: TPA from graphite in UHV: (a) desorption rate vs. sample temperature traces for different heating rates; (b) corresponding coverage vs. temperature curves integrated from TPD spectra; (c) Arrhenius plots derived for different coverages. The enthalpy of desorption amounts to +(140.2 ± 9.5) kJ mol^{-1}. (a and c are adapted from [16] with permission from American Chemical Society)

2.3 Dissolution enthalpy

The enthalpy of dissolution is derived from temperature dependent solubility measurements. This is accomplished by using temperature dependent UV-vis absorbance spectra. Based on the Beer-Lambert-Bouguer law, absorbance is proportional to solute concentration,

$$A = log\left(\frac{I - I_d}{I_0 - I_d}\right) = a \cdot l \cdot c \qquad (2.3.1)$$

Here A is the absorbance, I the intensity of light transmitted through the solution, and I_d the dark spectrum. The reference intensity I_0 is assigned to the intensity of light transmitted through the pure solvent. a is the absorption coefficient, l the optical path length, and c the concentration of the solute. Therefore, a UV-vis spectrometer can be used to quantify the concentration of saturated solutions, i.e. the solubility. A thermodynamic description of solubility is given in the first subsection. Theoretical descriptions of light absorption are provided in the following subsection. Experimental details are introduced in the last subsection.

2.3.1 Thermodynamics of solvation

The absorbance of saturated solutions is measured after the system has reached thermodynamic equilibrium. Solubility of compounds can be influenced by temperature, pressure, and the type of solvent. For solvation without dissociation, the relation between the Gibbs free energy change upon solvation, ΔG_{sol}, and the solute concentration of an ideal solution is given by [106],

$$\Delta G_{sol} = \mu_{sol} - \mu_s = \Delta H_{sol} - T\Delta S_{sol} = -RT \ln X_{sol} \qquad (2.3.2)$$

Here μ_{sol} is the chemical potential of the solution phase, μ_s the chemical potential of the solid phase, ΔH_{sol} the enthalpy change upon solvation, ΔS_{sol} the entropy change of solvation, and X_{sol} the mole-fraction of the saturated solution.

Assuming ΔH_{sol} and ΔS_{sol} do not change with temperature, ΔH_{sol} can be derived from the van't Hoff equation. Together with equation (2.3.1), ΔH_{sol} can be calculated by,

$$\Delta H_{sol} = \left[\frac{\partial(-\ln X_{sol})}{\partial(1/RT)}\right]_p = \left[\frac{\partial(-\ln c)}{\partial(1/RT)}\right]_p = \left[\frac{\partial(-\ln A)}{\partial(1/RT)}\right]_p \qquad (2.3.3)$$

Accordingly, the enthalpy of solvation can be calculated from a linear fit in plots of $-\ln A$ vs. $1/RT$. For ideal solutions, this value is equal to the fusion enthalpy of solutes. For non-ideal solutions, dissolution is considered as a two-step process: first the solute solid melts; then the solute liquid and the solvent form a solution. Accordingly, ΔH_{sol} is considered as the sum of ΔH_f, the fusion enthalpy of solute crystal, and ΔH_m, the mixing enthalpy of the solute liquid and the solvent. However, in this thesis, only the overall enthalpy change of solvation ΔH_{sol} is relevant. By using equation

(2.3.3), ΔH_{sol} can be directly obtained from the temperature dependence of the absorption spectra.

2.3.2 Theoretical description of electronic transitions

Molecular energy states are partitioned into three groups of discrete energy states, i.e. electronic states ($1\sim20\,\mathrm{eV}$, $60\mathrm{nm} < \lambda < 1250\,\mathrm{nm}$), vibrational states ($0.05\sim1\,\mathrm{eV}$, $1.25\mu\mathrm{m} < \lambda < 25\mu\mathrm{m}$), and rotational states ($< 0.05\mathrm{eV}$, $\lambda > 25\mu\mathrm{m}$). The three groups of states are relevant to electron motions, nucleus vibrations, and molecular rotations, respectively. Emission and absorption of ultraviolet to visible light (UV-vis, 100-800 nm) are typically related to electronic transitions, which have a substantially larger extinction coefficients than rotational and vibrational transitions. However, electronic transitions are always accompanied by rotational and vibrational transitions. Therefore, absorption/emission peaks in UV-vis spectra broaden into absorption/emission bands.

Electronic transitions can occur for π, σ, and n electrons, corresponding to double or triple bonds, single bonds, and lone pair electrons, respectively. According to molecular orbital theory, every bonding orbital with a lower energy has a corresponding antibonding orbital with a higher energy, i.e., every π or σ orbital has a corresponding π^* or σ^* orbital. By absorption of photons, a valence electron can be promoted from the ground state to an excited state. Also, n electrons can be promoted to π^* and σ^* orbitals, even though they are not bonding, i.e. do not have a corresponding antibonding orbital. Based on the energetic order of bonding and anti-bonding states σ, π, n , π^* and σ^*, four different kinds of transitions can take place, with different excitation energies,

$$\Delta E_{n\rightarrow\pi^*} < \Delta E_{\pi\rightarrow\pi^*} < \Delta E_{n\rightarrow\sigma^*} < \Delta E_{\sigma\rightarrow\sigma^*} \tag{2.3.4}$$

Most of the absorption spectra of organic compounds are dominated by $\pi \rightarrow \pi^*$ and $n \rightarrow \pi^*$ transitions. These transitions usually take place in unsaturated compounds, i.e. chromophores. The simplest chromophores contain groups with double or triple bonds, e.g. vinyl groups, carboxyl groups, nitroso-groups, ethynyl groups, azotoluene, etc. Aliphatic substituents, e.g. $–CH_3$, $-C_2H_5$, are usually not able to absorb UV-vis light by themselves. However, substituents on chromophores can shift and enhance absorbance through the n–π conjugation effect.

Transitions in aromatic compounds as relavant to this work are related to transitions between different π and π^* states in aromatic rings, are associated with Benzoic and Ethylenic bands (B&E bands).[107] For instance, Benzene has three $\pi\rightarrow\pi^*$ transitions: one B band and two E bands. The B band is observed around 255 nm, with the corresponding extinction coefficient $215\ \mathrm{L}\cdot mol^{-1}\cdot cm^{-1}$. The E_1 band is at 200 with an extinction coefficient of $8000\ \mathrm{L}\cdot mol^{-1}\cdot cm^{-1}$; the E_2 band at 180 nm, with an extinction coefficient of $6\times10^4\ \mathrm{L}\cdot mol^{-1}\cdot cm^{-1}$.[108]

2.3.3 Experimental setup and an example

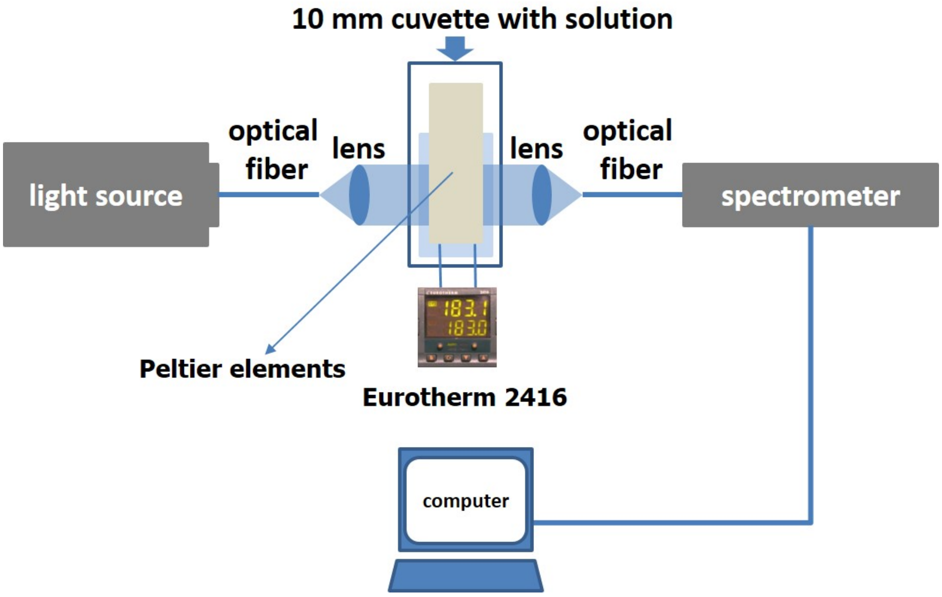

Figure 2.3. a scheme of the UV-vis absorption spectrometer; the cuvette is heated by two Peltier elements mounted on two sides of the cuvette at a direction perpendicular to the light path. Solution temperature is stabilized by a Eurotherm 2416 which controls the current through the Peltier elements. Light is transmitted from an optical fiber and then focused by a lens into a collimated parallel beam. After transmission through the cuvette, it is again focused by another lens into another optical fiber. After the light signal is analyzed by the spectrometer, an absorbance spectrum is generated by the software.

In this work, an USB4000 Miniature Fiber Optic Spectrometer from Ocean Optics, an ISS-UV/VIS light source, and a quartz glass cuvette (Hellman 100-QS) with an optical path length of 10 mm were used. The cuvette is mounted inside a closed opaque box to reduce background light from outside. The light source consists of a combined Deuterium and Tungsten bulb, with light emission ranges of 200-400 nm and 360-850 nm respectively. The emitted light is transmitted through an optical fiber; and then is focused into a collimated beam by a lens. After transmission through the cuvette containing the solution, the light is again focused by another lens into another optical fiber and then conducted into the spectrometer.

About 2 ml oversaturated solution was used for the measurement. It was prepared at room temperature with a large amount of bulk crystals (~0.1mg) mixed with two ml solvent in the cuvette. Crystals were separated from the saturated solution by putting the cuvette into a centrifuge at a spin speed of 100 rounds s^{-1} for 5 hours.

After the sample was prepared, the cuvette was mounted in the testing system. A type K thermocouple immersed into the solution in the cuvette was again used to monitor the solution temperature. By a combination of a Eurotherm 2416 controller and two Peltier elements (TEC1-03504), the solution temperature was stabilized with in ± 0.2 °C. Peltier elements were gently pressed on the sidewalls of the cuvette using two screws.

Transmission spectra through pure solvent at each temperatures were used as the reference spectra. Absorbance spectra were recorded after the solution equilibration for 24 hours after the solution temperature stablized. This waiting time is assumed to be sufficient when the solubility is very low as for the systems studied in this work.

TPA absorption spectra in nonanoic acid were acquired between 30 °C and 42 °C; SDA absorption spectra in nonanoic acid were acquired between 30 °C and 54 °C; HBTP absorption spectra in nonanoic acid were acquired between 22 °C and 54 °C.

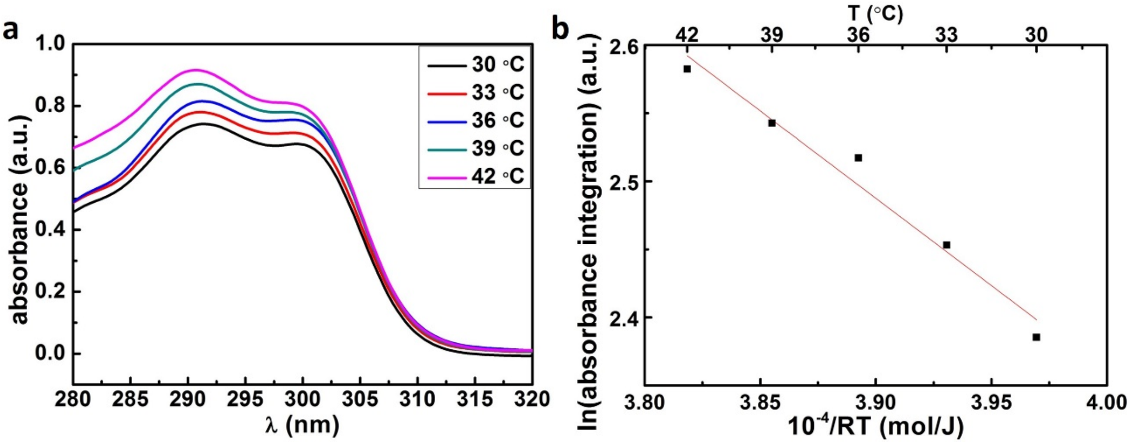

Figure 2.4. Measurement of TPA solubility in 9A as a function of temperature: (a) UV−Vis absorption spectra of saturated TPA in 9A solutions obtained at different temperatures; (b) Van't Hoff plot of the absorbance integrated in the interval λ = 290 nm-320 nm. The slope yields a value for the enthalpy of dissolution of +(12.8 ± 1.3) kJ mol^{-1} (permission from American Chemical Society [16], cf. section 4.4).

In Fig. 2.4, the absorbance spectra of TPA in 9A solvent at different temperatures and the corresponding van't Hoff plots are illustrated (cf. section 4.4). Two absorption bands center at 290 and 300 nm, as shown in Fig. 2.4 (a), which relate to n−π* and π−π* transitions of the aromatic core respectively. To reduce the statistical error, the total amount of dissolved molecule is estimated by integrating of the absorbance over the major absorbance band λ = 290-320 nm. The corresponding van't Hoff plot yields a dissolution enthalpy of +(12.8 ± 1.3) kJ mol^{-1}. Absorbance at shorter wavelength is not considered because the weak signal is obscured by the background noise of the spectrometer.

2.4 Computational methods

Predicting the macroscopic properties of materials is one of the essential goals of theoretical material science. To this end, computational methods are powerful and convenient tools. Depending on the objectives, different computational methods need to be applied. First principle methods based on quantum mechanics are the best choice for calculations at the electron level [109-111], while molecular mechanics, molecular dynamics, and Monte Carlo methods are most suitable for simulations at the molecular level. They are computationally cheaper than quantum chemistry, especially for large systems [16, 17, 112, 113].

In this section, the computational methods employed in this research are briefly introduced. Molecular mechanics (MM) and molecular dynamics (MD) were utilized to study hydrogen bonded self-assembly. Two density functional theory based approaches were then used to study halogen bonded self-assembly and were then compared to each other. One is the GGA-PBE functional [114] with an empirical dispersion correction (D2) proposed by Grimme (PBE+D) [115]. The other is van der Waals density functional (vdW-DF). Natalia Martsinovich (University of Sheffield, U.K.) performed all the simulations described in this dissertation.

2.4.1 Molecular mechanics

In principle, macroscopic properties can be derived from the atomic level, as described by quantum mechanics. However, for very large systems, quantum chemistry simulations are not possible, due to the limitations of computational power. Alternatively, molecular mechanics (MM) based on classical mechanics were used for simulations of large systems. Atoms instead of electrons are treated as the smallest unit, and electron movements or distributions are ignored.

MM simulations have been widely applied to study molecular interactions [116], especially interactions between molecules and surfaces [117]. The total interaction energy is obtained from the sum of pairwise interactions between atoms. Potential energies of covalent bonding and non-covalent bonding are described using different terms in force field functions. Bonding terms are usually used to describe covalent bonding. The corresponding potential energies are written as $E_{bonded} = E_{bond}+E_{angle}+E_{dihedral}$. On the other hand, non-bonding terms are used to describe non-covalent bonding interactions. The corresponding potential energies are usually described as $E_{non\text{-}bonded} = E_{electrostatic}+ E_{van\ der\ Waals}$.

Intermolecular interactions only depend on the distances between atoms. Energy is described as a function of atomic coordinates using classical mechanics instead of wave functions or electron density. Different force fields are used to simulate intermolecular and surface-molecule interactions. Parameters of force fields are typically obtained by experimental techniques or computational methods based on quantum mechanics. In many cases, MM simulations are used together with molecular dynamics (MD) for structural optimizations [112, 113].

In this thesis, binding enthalpies of organic bulk crystals, intermolecular interactions of self-assembled monolayers, and surface-molecule interactions were simulated by using the Tinker code [118] and the MM3 force field [119, 120]. The energy of the double hydrogen bonds between the carboxylic acid groups is significantly enhanced by resonance effects; this is usually not covered by MM simulations. Therefore, the parameters of the so-called resonance assisted hydrogen bonds (RAHBs) were adjusted to reproduce the bond length (r = 1.75Å) and energy (7.78 kcal mol^{-1}) in a carboxylic acid cyclic dimer [120]. 2D arrangements of TPA and SDA were obtained by searching for the energy minimum close to STM measured lattice parameters. The 3D arrangement of TPA was obtained by searching for the energy minimum close to the lattice parameters obtained by X-ray diffraction [121].

2.4.2 Molecular dynamics

MM simulations are effective for studying interactions in static 2D- or 3D- structures. However, for problems like thermodynamic equilibrium in solutions, the physical movements of molecules need to be considered. To this end, molecular dynamics (MD) is developed to describe the physical movements of molecules and atoms. In MD simulations, molecules are allowed to interact for a short period of time. The trajectories of these molecules are described by numerically solving Newton’s equations. Intermolecular forces and potential energies are described by force fields as discussed above for molecular mechanics. By choosing the proper statistic ensemble and force fields for the system, all the physical movements of the system can be obtained from the time integration of the differential equations of motion.

In this study, MD simulations were used to evaluate the dissolution enthalpy of TPA in 9A solution. The canonical (NVT) ensemble was chosen for MD simulations using the Nose-Hoover thermostat at 298 K, with an integration time step of 1 fs. All covalent bonds to H atoms were constrained to their ideal bond length. The “rattle” (cf. section 4.5) algorithm was used for integrating the differential equaitons of motion. Two different force fields were used in the MD calculations: the MM3 force field and the CHARMM27 force field [122] which is widely used for simulations of organic and biomolecules [123].

2.4.3 Density functional theory

Methods based on classical mechanics are not appropriate for describing interactions related to electron distributions, like halogen bonds. More accurate simulations that consider the electron distributions are required for evaluating the binding geometries and energies.

As mentioned at the beginning of this section, electronic states can be obtained from the Schrödinger equation. However, an analytical solution of the Schrödinger equation is already impossible for multi-body problems, and virtually impossible for multi-molecule systems. Since the 1940s, plenty of efforts have been made to approximately solve the Schrödinger equation. After Born and Oppenheimer proposed the single electron approximation that the atom core dynamics can be neglected when compared to electron dynamics, Hartree and Fock proposed a further assumption that electrons can be treated as moving in an effective potential generated by the atom core and other electrons. Accordingly, a system containing *N* electrons can be described by *N* single electron Schrödinger equations:

$$H\Psi = [T + V + U] = \left[\sum_{i}^{N} -\frac{\hbar^2}{2m}\nabla_i^2 + \sum_{i}^{N} V(\vec{r}_i) + \sum_{i<j} U(\vec{r}_i, \vec{r}_j)\right]\Psi = \mathrm{E}\Psi \quad (2.4.1)$$

Where *T* is the kinetic energy of electrons, *U* is the exchange interaction between electrons. *V* is the effective potential of the calculated system. However, it is still difficult to find the analytical solution of Hartree-Fock equations.

In the 1920s, Thomas and Fermi proposed a model that the kinetic and potential energies of the system are described using the electron density. In 1951, a function proportional to $\rho^{1/3}$ was proposed by Slater to describe the exchange interactions of the electrons, and meanwhile the Hartree-Fock-Slater method was proposed to describe multi-atomic systems. In 1964, Hohenberg and Kohn presented the Hohenberg-Kohn theorem which states that the energy of the ground state of multi-electron systems can be determined by the corresponding electron density [124]. In 1965, Kohn and Sham derived a group of self-consistent equations from the Hohenberg-Kohn theorem based on the Local Density Approximation (LDA) [125], where the uniform electron gas approximation is applied to calculate the exchange energy,

$$\left[-\frac{1}{2}\nabla^2 + V_{eff}(\vec{r})\right]\Psi_i(\vec{r}) = \varepsilon_i\Psi_i(\vec{r}) \quad (2.4.2)$$

$$V_{eff}(\vec{r}) = \phi(\vec{r}) + V_{xc}(\vec{r}) \quad (2.4.3)$$

$$\phi(\vec{r}) = v_r(\vec{r}) + \int \frac{n(\vec{r})}{|\vec{r} - \vec{r}'|} d\vec{r}' \quad (2.4.4)$$

$$V_{xc}(\vec{r}) = \frac{\delta E_{xc}[n]}{\delta n} \quad (2.4.5)$$

$$n(\vec{r}) = \sum_{i=1}^{N} |\Psi_i(\vec{r})|^2 \quad (2.4.6)$$

Here ε_i is the Kohn-Sham eigenvalue of the orbital energy, $V_{eff}(\vec{r})$ is the effective potential. $\phi(\vec{r})$ is the Coulomb potential, $V_{xc}(\vec{r})$ is the exchange potential of electrons, and $n(\vec{r})$ the electron density. Kohn-Sham equations can be solved based on a starting electron density $n(\vec{r})$, which can be obtained by the sum of the electron densities of atoms $|\Psi_i(\vec{r})|^2$. Effective potentials and Kohn-Sham equations can be solved self-consistently. Therefore, the multi-electron problem is simplified into a single electron problem in an effective potential field.

Although this so-called DFT-LDA has accomplished great success in terms of the properties of atoms, molecules, and solids, it was believed that quantum chemistry was unable to give reliable results. This was the case until the 1990s, when the approximation was improved using more advanced models for the exchange potential. In this research, the Generalized Gradient Approximation model using Perdew-Burke-Ernzerhof functional (GGA-PBE functional) was used to optimize the 2D arrangement of molecules and calculate the monolayer binding energy of halogen bond mediated superstructures [126].

However, even with more advanced exchange potentials, it is still difficult to calculate the energy of weak interactions, like van der Waals interactions. Different approaches have been proposed to solve this problem. The most popular and successful method is the empirical dispersion correction proposed by Grimme [127]. In this research, the binding energy of a halogen bond mediated monolayer was calculated using the GGA-PBE functional with D2 correction (PBE+D) [115, 128]. In addition, a van der Waals density functional (vdW-DF) was used for comparison. The accuracy of the simulations was tested through comparison with higher level simulations for a pyridine-bromobenzene dimer. Further details are described in section 6.4.

2.5 Evaluation of the entropy change

From the thermodynamic point of view, a spontaneous process takes place when the Gibbs free energy decreases, i.e. $\Delta G=\Delta H-T\Delta S<0$. Therefore, ΔS becomes important at critical conditions like concentration thresholds and temperature thresholds because $\Delta H\approx T\Delta S$, i.e. it becomes comparable to the enthalpy. According to statistical mechanics, entropy is related to degrees of freedom. Hence, for molecules in the solution phase, the higher degree of freedom results in a higher entropy as compared to molecules in the monolayer. After self-assembly, the entropy of adsorbates decreases, resulting in a negative ΔS of the system.

This section focuses on the evaluation of the entropy change upon self-assembly by using a theoretical model proposed by Whitesides *et al* [129]. In this model, entropies of molecules in solution are partitioned into translational, rotational, vibrational, and conformational entropy contributions. Since TPA and HBTP are conformationally rigid, the conformational entropies are negligible in both the solution phase and the adsorbed monolayer. In principle, SDA can adopt both trans and cis conformations. Since the cis conformation is rather high in energy, this conformational freedom is neglected in the entropy estimation. Hence, the total entropy of the molecules can be simplified into the sum of the translational, rotational, and vibrational entropy.

The translational entropy is derived from statistical mechanics based on the single atom approximation. For a single atom, the other components of the total entropy are all zero. Accordingly, translational entropy per molecule in the solution phase is given by the Sackur-Tetrode equation for the gas phase,

$$\mathrm{S_{trans}} = -\mathrm{R}\ln\left[\frac{1}{\mathrm{c}}\left(\frac{2\pi \mathrm{m}\mathrm{k_B}\mathrm{T}\mathrm{e}^{5/3}}{\mathrm{h}^2}\right)^{3/2}\right] \tag{2.5.1}$$

R is the gas constant, *m* the molecular mass, k_B Boltzmann's constant, *T* temperature, *e* Euler's number, *h* Plank's constant. Since equation (2.5.1) was originally conceived for the gas phase, the solvent is taken into account to avoid the overestimation of the translational entropy. Molecules are not entirely free in the whole solution volume, but only in the free space between the solvent molecules. Therefore, the concentration is corrected by referring to the free volume instead of the total volume. In this work, the hard cube approximation is applied for the calculation of the free volume V_{free} [129].

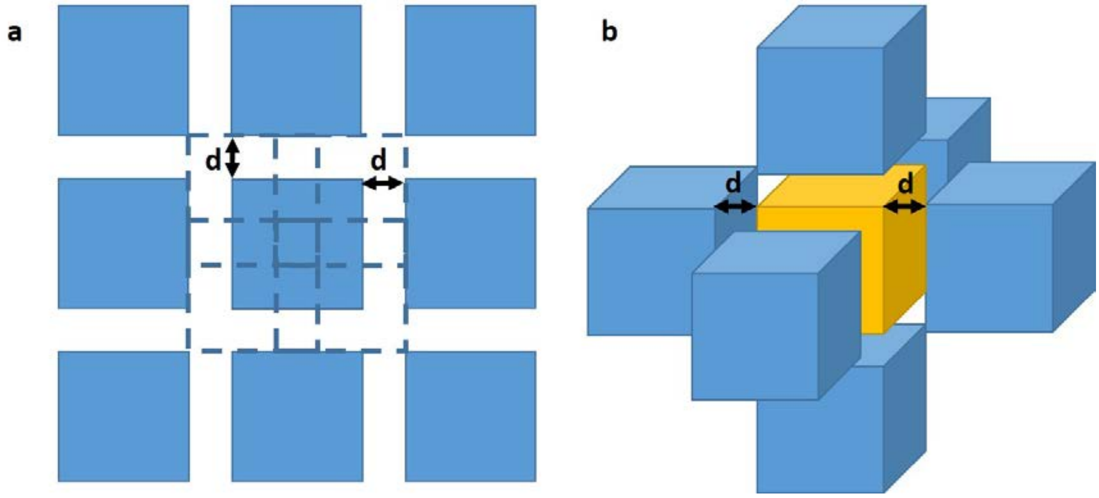

Figure 2.5. Free volume for hard cube approximation. (a) illustrates the 2D case, where the free area of the central hard square equals to the area defined by the dot line in the corner (edge length 2 × *d*, where *d* is the average free length at each dimension); (b) the 3D model, the free space of the center of yellow hard cube equals to the volume of the cube in the coner with a edge length of 2 × *d*.

In the hard cube approximation, solvent molecules are considered as a regular array of hard cubes, as depicted in Fig. 2.5 b. V_{free} is defined as the space for the center of mass of a molecule in liquid to move freely, which is determined by the neighboring molecules. In each direction, average distance d between neighboring molecules is determined by the difference of two distances. One is the average distance between the centres of adjacent cubes; the other is the edge length of each cube, which is defined by the molecular volume. Since a molecule can move in both directions of each dimension, the free distance at each dimension is obtained by doubling the obtained average distance between adjacent atoms, i.e. 2 × *d*, as depicted in Fig. 2.5 a. Extend the 1D case to 3D, the free volume per molecule is given by,

$$V_{free} = (2 \times \mathrm{d})^3 = \left[2\left(\sqrt[3]{V_{ave}} - \sqrt[3]{V_{molc}}\right)\right]^3 \qquad (2.5.2)$$

Here, V_{free} is the free volume, V_{ave} the average volume occupied by one 9A dimer, V_{molc} the molecular volume, i.e. the van der Waals volume.

In this work, the average distance between certres of adjacent cubes is calculated from the density of the liquid phase. Taking 9A solvent as an example, the density of the liquid phase is 906 g L^{-1}. Since it is well known carboxylic acid molecules exist as dimers in their liquid phase, one dimer is considered as one hard cube in this thesis. Together with its molar mass 158.2 g mol^{-1}, the average volume per 9A dimer is calculated to be 584 Å^3. Accordingly, the average distance between certres of adjacent 9A dimer cubes is 8.36 Å. The molecular volume is approximated as the corresponding van der Waals volume, which is calculated to be 346.9 Å^3 per 9A dimer, corresponding to a cube edge of 7.03 Å.

Applying equation (2.5.2), the free volume per 9A dimer is calculated to be 19.25 Å^3. Accordingly, 1 Liter of 9A solvent has a free volume of 31.3 mL. For the evaluation of translational entropies, all concentrations were referred to this free volume, leading to an apparent concentration enhancement by a factor of ~32.

In a similar way, with a mass density of 7A solvent of 0.92 g·cm^{-3} and a van der Waals volume of 278.6 Å^3 per 7A dimer, V_{free} is estimated as 32.6 mL per liter 7A, leading to a concentration enhancement by a factor of ~31. The enhancement factors are similar for 7A and 9A solvent.

Applying the obtained free volume to equation (2.5.1), a significant overestimation for $-T\Delta S_{trans}$ of ~8 kJ mol^{-1} was obtained as compared to the corresponding value obtained using the actual volume.

S_{trans} of TPA in 9A solution was evaluated using the experimentally determined critical concentration of 120 µmol L^{-1}; S_{trans} of SDA in 9A solution was evaluated using the critical concentration of 4.1 µmol L^{-1}; S_{trans} of HBTP in 7A solution evaluated using a critical concentration of 28.8 µmol L^{-1}. For evaluation of S_{trans} of 9A-9A dimers a concentration of 2.86 mol L^{-1} was used, i.e. half of the concentration of 9A in 9A; for 7A-7A dimers, a concentration of 3.54 mol L^{-1} was used.

	Density (g/L)	Molar mass (g/mol)	Average volume (Å^3)	Molecular volume (Å^3)	Free volume per Liter (mL)
9A-9A	906	316	584	346.9	31.3
7A-7A	920	260	496	278.6	32.6

Table 2.1. Involved parameters and the results of calculation of the free volume of the used solvent 7A and 7A. Since it is well known that fatty acids exist as dimers in their liquid phase, here we use 7A-7A and 9A-9A dimer as the smallest unit for calculation.

The rotational entropy of molecules in the solution phase was estimated by directly using the rotational entropy derived for the gas phase. Based on the rigid rotator approximation, the rotational entropy was estimated within ~2% relative error [129, 130],

$$S_{rot} = -R \ln \left[\frac{\pi^{1/2}}{\gamma} \left(\frac{8\pi^2 k_B T e}{h^2} \right)^{3/2} (I_1 I_2 I_3)^{1/2} \right] \qquad (2.5.3)$$

Where I_1, I_2 and I_3 are the principal moments of inertia. γ is determined by the symmetry and was assumed 2 for 9A-9A, 7A-7A, TPA, 9A-TPA-9A, SDA, and 9A-SDA-9A, and 6 for HBTP molecule, as listed in Table 2.2.

	TPA	9A-9A	9A-TPA-9A	SDA	9A-SDA-9A	HBTP	7A-7A
γ	2	2	2	2	2	6	2

Table 2.1. γ used for the calculation of rotataional entropy of molecules, solvents and molecule-solvent complexes used in this work.

The vibrational entropy can be derived from statistical mechanics [131, 132],

$$\mathrm{S_{vib}} = -\mathrm{k}_B \sum_{i=1}^{n} \left[\frac{\frac{hv_i}{\mathrm{k}_B T}}{e^{\frac{hv_i}{\mathrm{k}_B T}} - 1} - \ln\left(1 - e^{-\frac{hv_i}{\mathrm{k}_B T}}\right) \right] \tag{2.5.4}$$

Where v_i is the characteristic frequency of the i^{th} vibrational mode, n is the number of all the vibrational modes. For almost all vibrational modes at room temperature, $TS_{vir} \ll 2$ kJ mol^{-1}. Hence, S_{vir} is almost negligible compared to the translational and rotational entropy in most cases (50~60 kJ mol^{-1} for the studied compounds in this work). Moreover, most of the high-frequency modes are not affected by self-assembly. Hence, the change of vibrational entropy, ΔS_{vir}, was also neglected in this research.

Total entropy change, ΔS_{tot}, is then simplified as the sum of translational and rotational entropy change. By assuming the entropy of the molecule in a monolayer is zero, total entropy change is given by,

$$\Delta S_{tot} = \Delta S_{trans} + \Delta S_{rot} \tag{2.5.5}$$

Chapter 3: Non-covalent interactions

Non-covalent interactions are the primary driving force of supramolecular self-assembly. Low binding enthalpies result in bond reversibility, i.e. the general requirement for low defect densities and long range ordering. The interfacial monolayers studied in this dissertation are stabilized by hydrogen bonds, halogen bonds, and dispersion forces. In this chapter, the weak intermolecular interactions involved in the studied systems are introduced. The first section focuses on hydrogen bonds and especially the two-fold cyclic hydrogen bonds between carboxylic acid groups. The second section introduces halogen bonds. The last section briefly describes the surface-molecule interactions, including dispersion forces and aromatic interactions.

Solutes and solvents

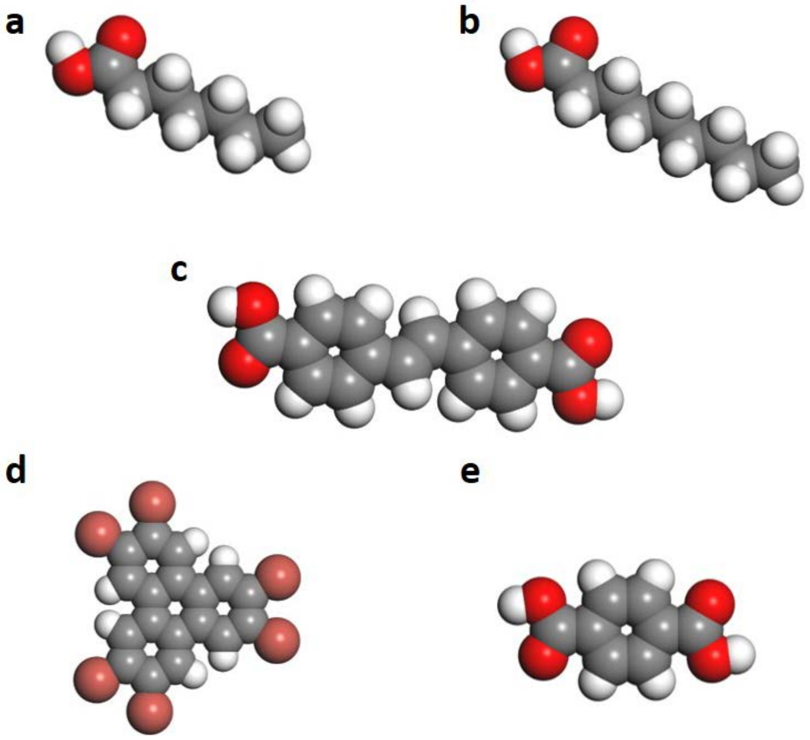

Figure 3.1. Molecular structures of (a) Heptanoic acid (7A): Sigma-Aldrich, purity ≥ 99%; (b) Nonanoic acid (9A): Sigma-Aldrich, purity ≥ 99%; (c) 4, 4’-stilbenedicarboxylic acid (SDA): ABCR GmbH & Co. KG, purity ≥ 96%; (d) Hexabromotriphenylene (HBTP): TCI Europe NV, purity ≥ 96%; and (e) Terephthalic acid (TPA): Sigma-Aldrich, purity ≥ 98%. (grey: carbon, red: oxygen, dark red: bromine, white: hydrogen)

In all cases, self-assembly was studied at the solution-graphite interface. Nonanoic acid (9A) and heptanoic acid (7A) were used as solvents. Two dicarboxylic acids, terephthalic acid (TPA) and 4, 4’-stilbenedicarboxylic acid (SDA) with different aromatic backbones are used as model systems to study hydrogen bond driven self-assembly. Molecular structures are illustrated in Fig. 3.1. Hexabromotriphenylene (HBTP) with an aromatic triphenylene core was used as model system to study halogen bond driven self-assembly.

3.1 Hydrogen bonds

Hydrogen bonds are of utmost importance in nature, e.g. for protein folding and molecular recognition in DNA. Intermolecular hydrogen bonds can also raise the melting and boiling points of compounds. For instance, water would not be liquid under standard conditions.

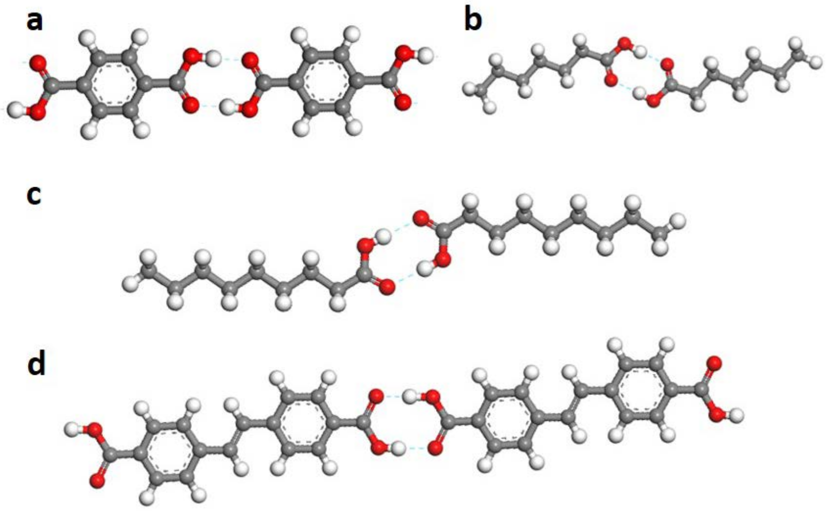

Figure 3.2. scheme of two-fold cyclic hydrogen bonds between carboxylic acid groups of (a) TPA molecules; (b) heptanoic acid molecules; (c), nonanoic acid molecules; and (d) SDA molecules.

An intermolecular hydrogen bond forms when hydrogen atoms bonded with more electronegative atoms (e.g. C, N, O, and F) are attracted by an electronegative atom of another molecule. It has been realized that hydrogen bonds result from a combination of electrostatic interactions, exchange repulsions, polarization effects, covalent bonding, and dispersion forces [133-135]. Typical binding energies of hydrogen bonds are in the range of 2~40 kJ mol^{-1}, i.e. weaker than covalent bonds but stronger than van der Waals interactions. [136] For instance, the strength of a very strong $F - H \cdots F$ hydrogen bond amounts to 29 kJ mol^{-1}, which is still much lower than the strength of the covalent F-H bond of 568 kJ mol^{-1}.[137, 138] Similarly, typical binding energies of $O - H \cdots O$ are in the range of 8~34 kJ mol^{-1} for the hydrogen bond whereas the O−H bond interaction is ~ 463 kJ mol^{-1}. [139, 140]

Due to high directionality and selectivity, hydrogen bonds are suitable interactions for the self-assembly of long-range ordered 2D superstructures on surfaces [3, 141].

Among all different substituents or functional groups that mediate hydrogen bonds, carboxylic groups play a special role. On one hand, they can simultaneously act as the hydrogen bond donor and acceptor at the same time [11]. On the other hand, the two-fold hydrogen bond becomes significantly enhanced because of the π-delocalization in the C═O segment. [142, 143] Accordingly, these hydrogen bonds are also called resonance-assisted hydrogen bonds (RAHBs). Temperature dependent infrared absorption spectra of the monomer to dimer ratio of benzoic acid yield a binding enthalpy of 67.8 kJ mol^{-1} [143], which is significantly stronger than the sum of two individual $O - H \cdots O$ bonds of 2 × 18.8 kJ mol^{-1} = 37.6 kJ mol^{-1}. In Fig. 3.2, hydrogen bonded dimers of molecules and solvents that are relevant for this study are illustrated as examples.

3.2 Halogen bonds

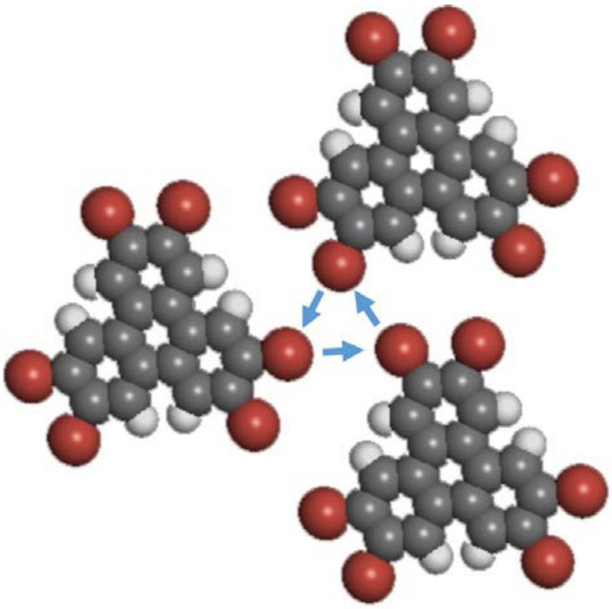

Figure 3.3. Arrangement of HBTP molecules in an adsorbed monolayer. Adjacent halogen atoms form triangular halogen bonds. Blue arrows indicate the direction of the electrical field.

The halogen bond is another important attractive non-covalent interaction. Unlike hydrogen bonds, their rationale remained enigmatic until Brinck *et al.* revealed the anisotropic charge distribution of a halogen substituent. [144] Later, Auffinger *et al.* [145] and Awwadi *et al.* [146] proposed a similar interpretation of halogen bonding using computed electrostatic potentials. A halogen substituent on a phenyl ring contains a electrophilic cap and a nucleophilic equatorial ring [147]. The region of the positive potential is called the σ-hole. Net attractions occur when the electrophilic cap of the halogen is attracted by a nucleophile, or when the nucleophilic ring is attracted by an electrophile. The first case is known as a halogen bond.

In the past few years, halogen substituents have gained much attention in self-assembly, due to their advantages in terms of crystal engineering and material functionality. [148, 149] From the functional side, halogens lower the electronic band gap of organic semiconductors and are resistant to ionization. This is particularly important for the stability of functional materials in the liquid phase. From the crystal engineering side, similar directionality can be achieved by choosing different halogens and a different nucleophile.

Different types of halogen bonds have been reported, e.g. between two halogen atoms, triangular cyclic halogen bonds [150, 151], and even fourfold halogen bonds [152]. The most frequently encountered case is the triangular cyclic halogen bonds. A theoretical description of triangular halogen-halogen-halogen bonds (cf. Fig. 3.3) between trihalomesitylene molecules is given by Bosch [20].

In this thesis, HBTP self-assembly at the 7A-graphite interface is studied as a model system. The building block is illustrated in Fig. 3.3, in which the monolayer is stabilized by triangular cyclic halogen bonds.

3.3 Surface-molecule interactions

In all the studied model systems in this dissertation, adsorption on graphite is mediated by weak van der Waals interactions. Herein, long-range dispersion forces play the major role for the surface-molecule interaction. The corresponding potential energy is proportional to R^{-6} for two single atoms, where R is the distance between atoms. For adsorption on surfaces, the total potential energy is obtained from the integration over all pairs of atoms of the adsorbate and the surface. Therefore, the attractive R^{-6} dependence is reduced to a z^{-3} dependence, where z is the vertical distance between the adsorbate and an infinite surface. This kind of interaction is comparably weak, e.g. 2-10 kJ mol^{-1} for adsorption of noble gases. However, its magnitude increases with the number of atoms, i.e. the size of the adsorbate. For adsorption of large planar compounds, dispersion forces become much stronger and take the major role in the total monolayer binding energy. One example is the HBTP monolayer studied in this work, where the surface-molecule interaction is obtained to be exactly the same by both DFT and MM simulations of ~186 kJ mol^{-1}.

For the adsorption of molecules that contain aromatic moieties on a graphite surface, the size-dependence of the surface-molecule interactions is enhanced by the so-called π-π stacking interaction. It has been theoretically proven that the interaction of aromatic dimers is stronger than for the corresponding saturated complexes [153]. A simplified model to describe aromatic interactions was proposed by Hunter *et al* in 1990 [154] where the aromatic ring is described as a σ-framework and two π-electron clouds. For a benzene molecule for instance, the π-electron clouds of the aromatic ring are negatively charged and the hydrogen atoms are positively charged. Accordingly, the two energetically most favorable conformations of benzene dimers (parallel displaced and edge-to-face) can be explained by electrostatic interactions. However, recent studies reveal that dispersion forces and exchange repulsions are in many cases more important for the total binding energy of π-π stacking interactions [155]. In the last few years, simulations based on van der Waals Density Functional Theory have been used to describe aromatic-graphene interactions [156]. Simulations of adsorbates with different sizes of aromatic systems suggest that the binding energy per carbon atom is proportional to the hydrogen/carbon ratio of the adsorbates [156].

Chapter 4: Born-Haber cycle for monolayer self-assembly at the liquid-solid interface – assessing the enthalpic driving force

Wentao Song, Natalia Martsinovich, Wolfgang M. Heckl, and Markus Lackinger, Born–Haber Cycle for Monolayer Self-Assembly at the Liquid–Solid Interface: Assessing the Enthalpic Driving Force. J. Am. Chem. Soc., 2013. **135**(39): p. 14854-14862, http://dx.doi.org/10.1021/ja407698t. Reproduced and adapted with permission from Journal of the American Chemical Society, Copyright 2013 American Chemical Society.

4.1 Abstract

The driving force for self-assembly is the associated gain in free energy with decisive contributions from both enthalpy and entropy differences between final and initial state. For monolayer self-assembly at the liquid−solid interface, solute molecules are initially dissolved in the liquid phase and then become incorporated into an adsorbed monolayer. In this work, we present an adapted Born−Haber cycle for obtaining precise enthalpy values for self-assembly at the liquid−solid interface, a key ingredient for a profound thermodynamic understanding of this process. By choosing terephthalic acid as a model system, it is demonstrated that all required enthalpy differences between well-defined reference states can be independently and consistently assessed by both experimental and theoretical methods, giving in the end a reliable value of the overall enthalpy gain for self-assembly of interfacial monolayers. A quantitative comparison of enthalpy gain and entropy cost reveals essential contributions from solvation and dewetting, which lower the entropic cost and render monolayer self-assembly a thermodynamically favored process.

4.2 Introduction

Supramolecular self-assembly has been extensively studied for gaining a fundamental understanding of its mechanisms and driving forces. [13-15, 157, 158] This knowledge provides the basis for the efficient and targeted bottom-up fabrication of functional nanostructures. Among the different environments and dimensionalities for self-assembly, two-dimensional surface-supported monolayers take a special role. On the one hand, adsorption on solid substrates readily provides an interface and support for the structures, an important prerequisite for applications in sensors and catalysis. [6-8] On the other hand, surface-supported monolayers are ideal model systems since their properties and become analytically accessible by established techniques, foremost Scanning Probe Microscopy. [9-12] Liquid environments are of particular interest because they enable facile preparation but also serve as suitable test grounds for biological environments. In addition, liquid environments mediate high mobility of the molecular building blocks and enhance bond reversibility. Consequently, many self-assembled structures represent the thermodynamic equilibrium. [9, 11, 12, 24, 25] This holds especially true for supramolecular monolayers at the liquid−solid interface, where thermodynamical descriptions were extremely successful for understanding structure formation and transitions, even in complex multicomponent systems. Thermodynamic models that utilize the concentration dependence of chemical potentials can explain the emergence of different phases with different surface packing densities as a function of solute concentration in homomeric systems [27], [28] and the emergence of different phases with different packing densities and compositions as a function of the two solute concentrations in bimolecular systems. [20] In an alternative approach, the free energy of monolayer self-assembly is estimated by separate evaluation of its contributions, i.e., the enthalpy gain and the entropy loss. Using this approach, it was possible to understand the driving force for temperature-induced reversible phase transitions [21] and the emergence of phases with nonideal, untypical hydrogen-bonding motifs in tricarboxylic acid monolayers. [21] On the other hand, Bellec *et al.* demonstrated that kinetic effects can also become important. [22] All these thermodynamic models provide rationales to understand structure selection but do not facilitate more detailed insight in the subtle balance of the various individual enthalpy and entropy contributions. Only such an in-depth understanding will result in a full quantitative thermodynamical picture of self-assembly, an important step toward deliberate control of nanostructure formation by self-assembly.

Monolayer self-assembly at the liquid−solid interface is driven by the free energy difference between the final state, where molecules are adsorbed and incorporated into the interfacial monolayer, and the initial state, where molecules are dissolved in the supernatant solution. In comparison to self-assembly at the vacuum−solid interface, the presence of the supernatant liquid phase has profound consequences. For instance, the substrate may be precovered with solvent molecules, and desorption of this wetting layer causes an additional enthalpy cost.

Because of the complexity of the solid-monolayer-liquid system and the various adsorption and desorption processes taking place at this interface, a precise quantification of the overall enthalpy difference of self-assembly can become intricate. In principle, microflow calorimetry (MFC) is an established technique to measure adsorption enthalpies from solution on graphitic supports. [41] To amplify the measured heat, MFC takes advantage of large surfaces, as available in graphon (graphitized carbon black). Despite the many advantages of MFC, such as its straightforwardness and the low instrumental effort, several drawbacks remain. First, it is not parameter-free, since the normalization of adsorption energies requires a precise measurement of the surface area, as typically obtained from gas adsorption experiments, which are also not parameter free. MFC is inherently limited to materials with large specific areas of distinct crystallographic surfaces (although this is less of a problem for graphitic materials, thanks to the availability of well-defined (0001) facets). Furthermore, the method is of limited use for processes with particularly small enthalpy differences because the accuracy decreases with the overall enthalpy.

As an alternative route for obtaining the overall enthalpy difference, we present the implementation of a Born−Haber cycle for interfacial monolayer self-assembly. This approach circumvents the above-mentioned disadvantages of MFC, and in addition not only the overall enthalpy is obtained but individual enthalpy contributions are evaluated, thereby offering detailed fundamental insights into the subtle thermodynamic balance of monolayer self-assembly. Moreover, the influence of the solvent can be better understood. This is particularly important because the solvent can play a key role in controlling the monolayer structure in the systems where polymorphism is possible.[42-44]

Widely studied terephthalic acid (TPA, 1, 4-benzenedicarboxylic acid) has been chosen as a generic model system because hydrogen-bonded networks are among the most important classes of interfacial monolayers. In addition, self-assembly of TPA was already experimentally studied on a variety of different surfaces [32, 49, 159-162] and theoretically by Monte Carlo simulations. [34, 163] Moreover, TPA is conformationally rigid, and its relatively small size permits more elaborate calculations as pursued here. However, until now no detailed quantitative thermodynamic understanding of TPA monolayer self-assembly from solution has been realized.

In this work, we combine the results from an array of experimental techniques to provide a detailed quantitative picture of all significant enthalpy contributions. In addition, all enthalpy contributions were independently assessed by molecular mechanics (MM) and molecular dynamics (MD) simulations based on the MM3 force field. [118-120] TPA bulk crystals, unsolvated TPA monolayers, isolated molecules in the gas phase, and dissolved molecules in nonanoic acid (9A) solution serve as well-defined and easily accessible reference states, both for experiments and theoretical calculations. Precise knowledge of the decisive overall enthalpy change enables a quantitative comparison with the entropy cost of self-assembly as obtained from established theoretical models. [129] Contrasting enthalpy gain and entropy cost reveals essential contributions from both solvation and wetting (or dewetting) the substrate by solvent molecules, which crucially affect both the enthalpy and the entropy balance.

4.3 Methods

4.3.1 Experimental methods

The sublimation enthalpy was derived by measurements of the effusion rate that is proportional to the saturated vapor pressure for different temperatures. To this end, an effusion cell equipped with a quartz crystal microbalance was used in high vacuum.[86] Constant slopes in the shift of resonant frequency (Δf) vs. time (t) traces for all temperatures indicate the validity of the chosen approach.

TPA solubility, i.e., the saturation concentration, was determined by temperature-dependent UV−vis absorption spectroscopy using spectra of pure 1-nonanoic acid (9A) solvent at the respective temperatures as reference. According to Lambert−Beer's law, the concentration is directly proportional to the absorbance. UV−vis absorption spectra of TPA exhibit two clear absorption bands centered at 290 and 300 nm due to n-π^* and π-π^* transitions as anticipated for an aromatic compound. Since there is no interference with absorption of the 9A solvent in this spectral range, temperature-dependent UV−vis absorption spectroscopy is very well suited to quantify the enthalpy of dissolution.

Temperature programmed desorption (TPD) experiments were conducted in ultrahigh vacuum. TPA monolayers were first deposited onto a graphite surface by thermal sublimation. Subsequently, the sample temperature was ramped up linearly in time, and the TPA desorption rate was simultaneously recorded by a mass spectrometer. Three sets of experiments were performed with three different heating rates ranging from 0.25 to 0.84 K s^{-1}. The complete analysis method was used to derive the desorption enthalpy because no a priori assumptions either on the desorption order or on the underlying desorption mechanism are required. [164]

4.3.2 Computational methods

Molecular mechanics and molecular dynamics calculations were conducted using the MM3 force field. [118-120] The strength of the 2-fold hydrogen bonds between carboxylic acid groups is considerably enhanced by resonance effects. [143, 165] So-called resonance-assisted hydrogen bonds (RAHB) can occur when the hydrogen bond donor and acceptor are connected by a short π-conjugated segment such as C═O in carboxylic groups. Then enhancement of the π-delocalization synergistically increases the hydrogen bond strength. Thus, in order to obtain accurate enthalpy values for hydrogen bonds, the MM3 force field was modified accordingly. [34]

The lowest energy of TPA bulk structure was found by first optimizing the lattice parameters A, B, and γ for the 2D lattice and then using them as a starting point for optimizing the lattice parameters C, α, and β. The calculated lattice parameters for the optimized triclinic TPA crystal were: A = 9.37Å, B = 7.70Å, C = 3.56Å, α = 83°, β = 74°,

γ = 131°, in good agreement with the X-ray crystal structure (form I): A = 9.54 Å, B = 7.73 Å, C = 3.74 Å, α = 109°9’, β = 73°36’, γ = 137°46’. [121]

A theoretical estimate for the enthalpy of dissolution was obtained from MD simulations of TPA molecules surrounded by 200 solvent molecules in a periodic box. The annealed solvent structure was used as a starting point for building a model of TPA in solution and for the following MD simulations. To create a model of TPA in solution, either one TPA molecule was added to the system of 200 annealed 9A molecules (two “added TPA” structures were used) or one of the 9A molecules was removed and replaced with TPA (four “substituted TPA” structures were used). The MD simulations of the pure solvent and of TPA in solution were conducted using the MM3 force field and, independently, using the CHARMM force field. [122]

4.4 Results and discussion

4.4.1 Monolayer structure

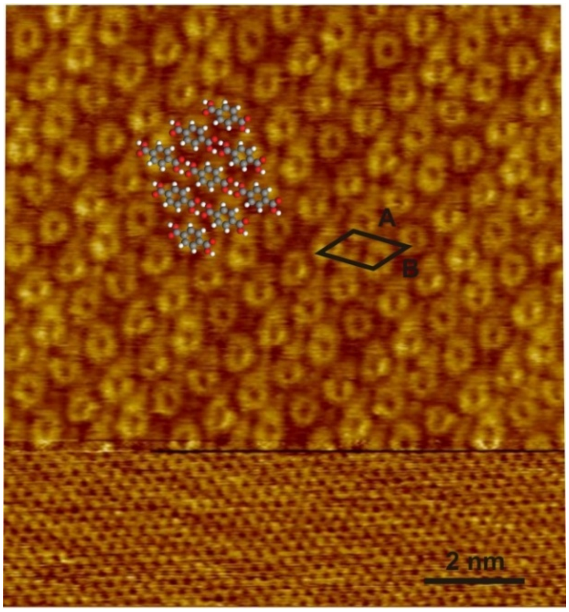

Figure 4.1. STM image of a TPA monolayer at the nonanoic acid−graphite interface. The lower part the graphite substrate was imaged with atomic resolution by decreasing the tunneling gap. With this internal calibration standard precise lattice parameters for the TPA monolayer of A= (9.6 ± 0.1) Å, B= (7.8 ±0.1) Å, γ=130°± 1° were deduced. The arrangement of TPA molecules is indicated by the overlay, and the black lines mark the unit cell (image size 10.9 × 10.2 nm^2, I = 100 pA, V_{sample} = −80.0 mV for TPA; I = 200 pA, V_{sample} = −1.53 mV for graphite).

The TPA monolayer structure at the 9A−graphite interface was determined by in situ Scanning Tunneling Microscopy (STM) experiments, a high-resolution image is depicted in Fig. 4.1. Precise unit cell parameters were obtained by calibration with the underlying graphite lattice. TPA forms well-ordered densely packed monolayers with lattice parameters A = (9.6 ± 0.1) Å, B = (7.8 ± 0.1) Å, γ=130° ± 1° and one molecule per unit cell. As indicated by the overlay, the monolayer structure consists of densely packed linear hydrogen bonded chains, where TPA molecules are interconnected by 2-fold cyclic hydrogen bonds between the carboxyl groups. The STM contrast always exhibited a Moiré pattern indicating a weak interaction between TPA and graphite and incommensurability of the superstructure with the graphite lattice.

4.4.2 Born-Haber cycle.

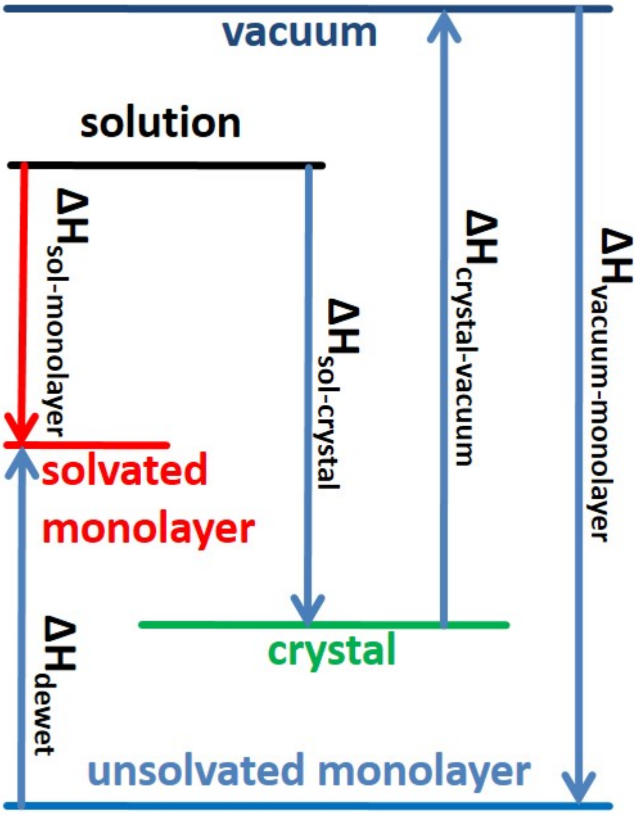

Figure 4.2. Scheme of the proposed Born−Haber cycle. $\Delta H_{sol\text{-}monolayer}$ (red arrow) is not directly accessible, but a detour via crystal, vacuum, and unsolvated monolayer (blue arrows) facilitates quantification of the overall enthalpy difference. There is a notable enthalpy difference for the monolayer at the vacuum−solid interface ("unsolvated monolayer") as compared to the liquid−solid interface ("solvated monolayer") due to solvent contributions.

The overall enthalpy change of TPA monolayer self-assembly is evaluated by the adapted Born−Haber cycle depicted in Fig. 4.2. The well-defined reference states are TPA bulk crystal, unsolvated TPA monolayer, isolated single TPA molecules in vacuum, and solvated single TPA molecules in 9A solution. Since the graphite substrate is initially precovered by an ordered 9A solvent wetting layer (cf. section 4.5), the enthalpy cost of dissolution of the 9A wetting layer and the enthalpy gain due to solvation of the adsorbed TPA monolayer by the solvent are taken into account by a dewetting enthalpy ΔH_{dewet}. Hence, knowledge of the sublimation enthalpy ($\Delta H_{crystal\rightarrow vauum}$), desorption enthalpy from the unsolvated monolayer into vacuum ($\Delta H_{monolayer\rightarrow vauum}$), the enthalpy of dissolution ($\Delta H_{crystal\rightarrow sol}$) and dewetting enthalpy ΔH_{dewet}, enables one to indirectly conclude on the decisive overall enthalpy difference between solution and solvated monolayer($\Delta H_{sol\rightarrow monolayer}$):

$$\begin{aligned}\Delta \mathrm{H}_{\mathrm{sol\rightarrow monolayer}} = {} & \Delta \mathrm{H}_{\mathrm{sol\rightarrow crystal}} + \Delta \mathrm{H}_{\mathrm{crystal\rightarrow vacuum}} \\ & + \Delta \mathrm{H}_{\mathrm{vacuum\rightarrow monolayer}} + \Delta \mathrm{H}_{\mathrm{dewet}} \end{aligned} \tag{4.1}$$

$$\begin{aligned}\Delta \mathrm{H}_{\mathrm{sol\rightarrow monolayer}} = {} & -\Delta \mathrm{H}_{\mathrm{crystal\rightarrow sol}} + \Delta \mathrm{H}_{\mathrm{crystal\rightarrow vacuum}} \\ & - \Delta \mathrm{H}_{\mathrm{monolayer\rightarrow vacuum}} + \Delta \mathrm{H}_{\mathrm{dewet}} \end{aligned} \tag{4.2}$$

The first three terms on the right-hand side of equation (4.1) refer to the experimentally measured enthalpy differences. There it was considered that permutation of initial and final state inverts the sign. In the following it will be demonstrated that all TPA related enthalpy differences can independently and consistently be assessed by both experimental and theoretical approaches.

4.4.3 Sublimation enthalpy.

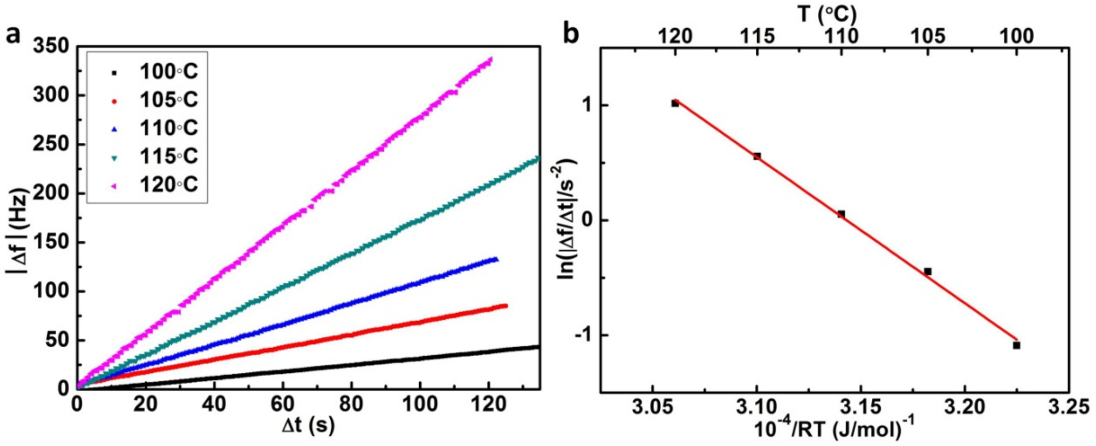

Figure 4.3. Measurement of the TPA effusion rate as a function of temperature: (a) resonant frequency shift Δf of the quartz crystal microbalance vs. time traces for different temperatures of the effusion cell; (b) corresponding Van't Hoff plot; each data set in (a) was fitted with a straight line and is represented by one data point. The slope corresponds to a sublimation enthalpy of +(127.2 ± 3.6) kJ mol^{-1}.

The sublimation enthalpy is derived from temperature-dependent measurements of the effusion rate of TPA with a quartz crystal microbalance in the range between 100 and 120 °C in high vacuum. The effusion rate is proportional to the saturated vapor pressure, thereby providing access to the related thermodynamic quantity. The corresponding Van't Hoff plot in Fig. 4.3b yields a sublimation enthalpy of $\Delta H_{crystal\rightarrow vacuum}$ = +(127.2 ± 3.6) kJ mol^{-1}. TPA sublimation is a strongly endothermic process because bonds within the crystal are broken and single molecules cannot regain this enthalpy in the gas phase. In these kinetic experiments, the sublimation rates of TPA monomers are measured, and a conceivable subsequent dimerization in the gas phase does not affect the experimental result. The binding energy of TPA in the crystal with respect to vacuum was also calculated by molecular mechanics (MM, cf. section 2.4 and section 4.5 for details). The theoretical evaluation of the sublimation enthalpy relies on the computational search for the lowest-energy of TPA bulk crystal structure by varying all lattice parameters and taking the experimental X-ray structure into account as an initial guess.[121] Thus, the aim was not to predict all possible TPA polymorphs, but to verify that the MM description of the TPA crystal structure is accurate and reliably reproduces the experimental structure. The calculated value of the crystal binding energy −129.1 kJ mol^{-1} is in excellent agreement with the measured sublimation enthalpy of +127.2 kJ mol^{-1}. This confirms the suitability of MM simulations and the MM3 force field (with appropriately modified hydrogen bond energy parameters [34]) for a reliable quantitative assessment of enthalpies in resonance enhanced hydrogen bonded structures.

4.4.4 Enthalpy of dissolution.

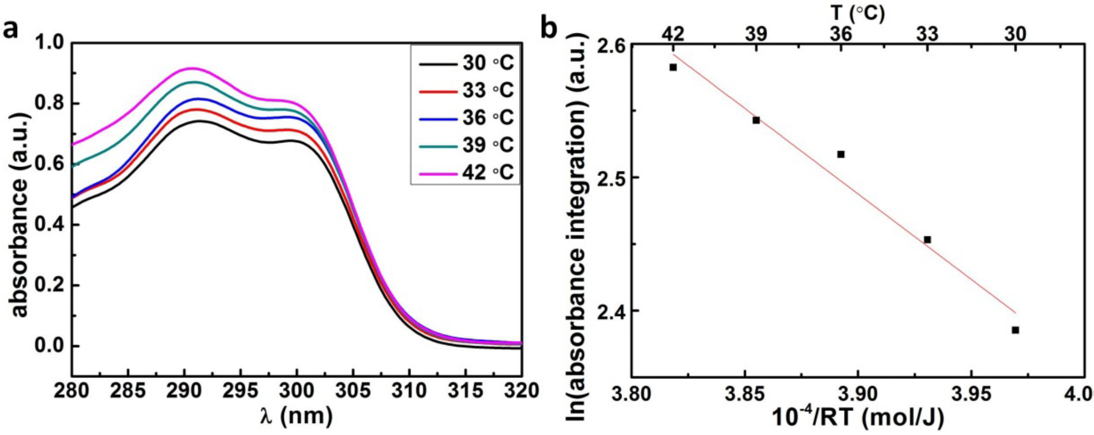

Figure 4.4. Measurement of the TPA solubility in 9A as a function of temperature: (a) UV-vis absorption spectra of saturated TPA in 9A solutions obtained at different temperatures; (b) Van’t Hoff plot of the absorbance integrated in the interval λ=290nm-320nm. The slope yields a value for the enthalpy of dissolution of +(12.8±1.3) kJ mol^{-1}.

In a similar way, solubility measurements of TPA in 9A as a function of temperature yield the enthalpy of dissolution $\Delta H_{crystal\rightarrow sol}$. UV−vis absorption spectra of TPA in 9A were acquired between 30 and 42 °C and are shown in Fig. 4.4a. For the Van’t Hoff plot depicted in Fig. 4.4b the total amount of dissolved TPA molecules was estimated by integrating the absorbance vs. λ curves over the absorption band, yielding an enthalpy of dissolution of +(12.8 ± 1.3) kJ mol^{-1}. The positive enthalpy of dissolution indicates again an endothermic process: the bulk crystal, where TPA molecules are stabilized by hydrogen bonds and additional van der Waals interactions, is the energetically more favorable state. This ideal stabilization is not fully regained in solution and the enthalpic disadvantage corresponds to the measured dissolution enthalpy. However, the dissolution enthalpy is still considerably smaller than the binding enthalpy of a 2-fold hydrogen bond between carboxylic acid groups −67.8 kJ mol^{-1} as obtained from infrared absorption spectra of benzoic acid monomer and dimer [143] or from the corresponding computed value −67.0 kJ mol^{-1}.[34] From the fact that the endothermic enthalpy of dissolution is still smaller than the binding enthalpy of a hydrogen-bonded carboxylic acid dimer, it is concluded that in the dissolved state TPA is again stabilized by hydrogen bonds: for statistical reasons, the TPA molecules are most likely surrounded by and bonded to 9A solvent molecules.

Molecular dynamics simulations with the MM3 force field yield an average solvation energy with respect to isolated TPA in vacuum of −(115.1 ± 39.4) kJ mol^{-1} (cf. section 2.2 and section 4.5). Additional MD simulations with the CHARMM27 force field [122] yield a value of −(118.0 ± 45.5) kJ mol^{-1}. The error bars were determined from several independent MD runs and are large because of very slow convergence of energies in MD simulations. The excellent agreement suggests that the MD results do not depend on the choice of force field. We will use the MM3 value for consistency with the other calculations.

Combination of the calculated energy of dissolved TPA with the calculated cohesive energy of the TPA crystal (−129.1 kJ mol^{-1}, cf. section 4.4) results in a theoretical dissolution enthalpy of +14.0 kJ mol^{-1}, in good agreement with the experimental value of +12.8 kJ mol^{-1}. Despite the large error bars of the MD simulations, theory and experiment agree that dissolution of TPA in 9A is an endothermic process with a small enthalpy of dissolution.

4.4.5 Binding enthalpy of TPA in a monolayer on graphite with respect to vacuum

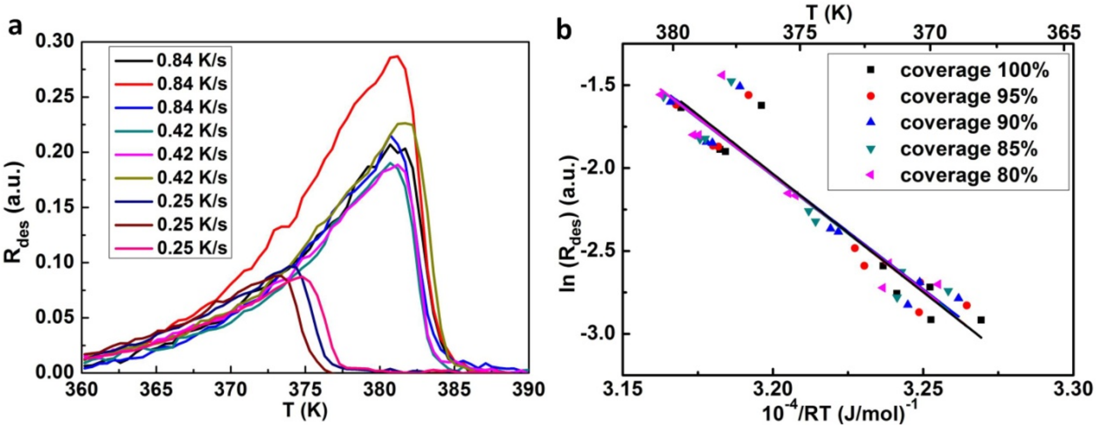

Figure 4.5. Temperature Programmed Desorption of TPA from graphite in ultra-high vacuum: (a) desorption rate vs. sample temperature traces for different heating rates; (b) Corresponding plot obtained from a complete analysis of the desorption traces. The enthalpy of desorption amounts to +(140.2±9.5) kJ mol^{-1}.

The enthalpy difference between TPA in the monolayer and in the gas phase $\Delta H_{\text{monolayer}\rightarrow\text{vacuum}}$ is quantified by thermal desorption of TPA from graphite in temperature-programmed desorption (TPD) experiments as illustrated in Fig. 4.5. This established surface science method results in a desorption enthalpy with respect to vacuum of +(140.2 ± 9.5) kJ mol^{-1}.

The theoretical monolayer binding enthalpy was calculated as the sum of independently acquired contributions from molecule−molecule and molecule−substrate interactions. This partition becomes necessary due to the incommensurability of TPA monolayers with the graphite lattice. A further advantage of this approach is the direct comparability of these two contributions. The approach is based on the reasonable assumption that adsorption does not significantly affect the strength of intermolecular bonds.

Theoretical molecule−molecule binding enthalpies were derived for a free-standing TPA monolayer, where optimized lattice parameters were found by scanning through a range of values of A, B, and γ. In good agreement with the experimental unit cell, only one energy minimum was found with A = 9.38 Å, B = 8.09 Å, γ = 131.5°. The binding energy of TPA in the freestanding monolayer was calculated to be −76.8 kJ mol^{-1}.

The potential energy for a single TPA molecule on graphite was calculated for a regular grid of different adsorption sites, and the corresponding adsorption energies were found to lie in a narrow range between −66.2 and −65.4 kJ mol^{-1} (with the lowest energy and highest energy adsorption configurations corresponding to AB and AA stacking of the benzene ring on the underlying graphite, respectively). The mean value −65.8 kJ mol^{-1} is a good approximation for the varying adsorption sites of TPA in the incommensurate superstructure. The small corrugation of the potential energy surface suggests that the underlying graphite does not strongly influence the registry of the TPA monolayer, as also experimentally corroborated by the Moiré pattern.

Combining the adsorption energy with the monolayer binding energy, the theoretical value for the binding enthalpy of TPA in the monolayer on graphite with respect to vacuum is −142.6 kJ mol^{-1}, again in perfect agreement with the experimental desorption enthalpy.

4.4.6 Dewetting enthalpy

The aliphatic 9A solvent molecules have a high affinity to graphite and likewise form stable ordered monolayers at the liquid−solid interface at room temperature as confirmed by STM imaging (cf. section 4.5). The fatty acid monolayer structures are comprised of lamellae of dimers in the all-trans conformation. [166] Initially, this 9A monolayer forms rapidly, and self-assembly of TPA monolayers requires desorption of this solvent wetting layer. MM calculations of the 9A monolayer desorption enthalpy with respect to vacuum yield a value of 105.7 kJ mol^{-1}, in perfect agreement with the experimental value of 107.5 kJ mol^{-1} as obtained from TPD experiments.[11, 167] When the TPA monolayer is adsorbed at the graphite/solvent interface, the upper side of the monolayer is exposed to the solvent and is solvated. There is no experimental evidence of 9A forming an ordered overlayer on top of the TPA monolayer, therefore this 9A overlayer is likely to be disordered and liquid-like. It is difficult to provide precise estimates of the interaction energy at this disordered and dynamic interface, either experimentally or computationally. As the upper estimate of the TPA/9A interaction, we can use the calculated energy of an ordered 9A monolayer above a TPA monolayer, −84.0 kJ mol^{-1} according to MM calculations. Combining the enthalpy cost of dewetting the graphite surface with the gain due to solvating the TPA monolayer yields a non-negligible enthalpy cost for dewetting of (at least) 21.7 kJ mol^{-1} per 9A molecule. Since the enthalpies in the Born−Haber cycle refer to TPA molecules, ΔH_{dewet} is given by:

$$\Delta \mathrm{H}_{\mathrm{dewet}} = \left(\Delta \mathrm{H}(9\mathrm{A})_{\mathrm{graphite}\rightarrow\mathrm{vacuum}} - \Delta \mathrm{H}(9\mathrm{A})_{\mathrm{TPA}\rightarrow\mathrm{vacuum}}\right) \cdot \frac{A_{TPA}}{A_{9A}} \qquad (4.2)$$

The renormalization factor considers that the area A_{9A} occupied by one 9A molecule of 66.5 Å^2 is slightly larger than the area of 56.8 Å^2 occupied by one TPA molecule. Accordingly, the contribution to the total enthalpy from dewetting per TPA molecule amounts to ΔH_{dewet} = +18.5 kJ mol^{-1}.

4.4.7 Overall enthalpy change for self-assembly of interfacial TPA monolayers

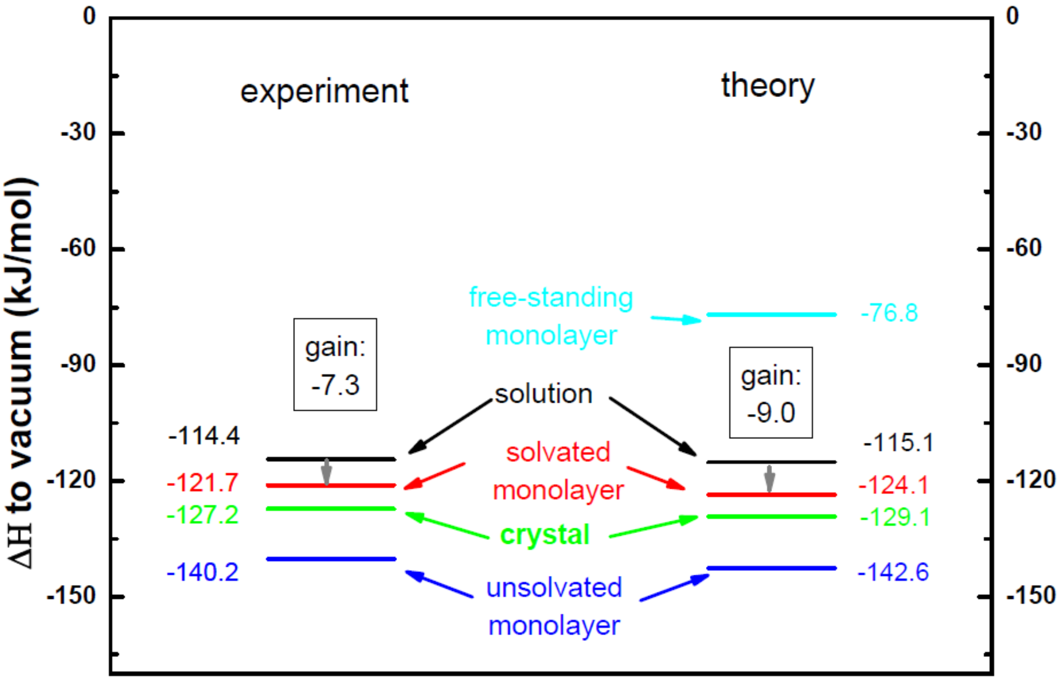

Figure 4.6. Results for the Born−Haber cycle: (left) experimental results; (right) theoretical results; the enthalpy of single TPA molecules in vacuum was used as reference for both theory and experiment.

Eventually, from a combination of all independently assessed enthalpy differences, the desired value for the overall enthalpy difference $\Delta H_{solution \rightarrow monolayer}$ for TPA monolayer self-assembly from solution can be evaluated according to equation 1. For the experimental Born−Haber cycle we obtain −7.3 kJ mol^{-1} and for the theoretical cycle the corresponding value amounts to −9.0 kJ mol^{-1}, in remarkable agreement with the experiment. Both cycles with all contributions are summarized in Fig. 4.6. For the first time the substantial lowering of the monolayer desorption enthalpy by the supernatant liquid phase is quantified. It is noteworthy that dewetting the graphite from the initially adsorbed solvent monolayer significantly reduces the enthalpy gain.

For comparison, the enthalpy of desorption of a TPA monolayer from graphite with respect to vacuum is around +140 kJ mol^{-1}, with negligible differences between experiment and theory. With such high desorption barriers spontaneous desorption of TPA at room temperature remains impossible. Even when an extraordinarily high pre-exponential factor of 10^{18} s^{-1} is assumed for thermally excited desorption, the corresponding desorption rate at room temperature still remains undetectably low in the order of 10^{-8} s^{-1}. Yet, the presence of the solvent significantly lowers the TPA desorption barrier: the value in liquid amounts to only a few percent of the vacuum value. This astonishingly drastic effect is caused by both solvation and solvent wetting. Consequently, thermally stimulated desorption becomes feasible at the liquid−solid interface, whereas it can be fully excluded for the same combination of adsorbate and surface at the vacuum-solid interface. Evidence for desorption even of larger compounds at room temperature at the liquid−solid interface is provided by numerous STM experiments, [168-170] but only here the corresponding enthalpy value has been derived, which for the first time provides a quantitative rationale for this phenomenon.

4.4.8 Concentration threshold for monolayer self-assembly

For spontaneous self-assembly, the enthalpy gain has to overcome the entropy cost, which in solution increases with decreasing solute concentration.[129] This is because the contribution from translational entropy increases with the logarithm of the reciprocal concentration, according to the Sackur−Tetrode equation. Substantial experimental evidence for an increasing entropy cost at lower concentrations is provided by monolayer self-assembly studies at the liquid−solid interface, where either polymorphs with low surface packing densities become favored at lower concentrations [21, 27, 54, 171] or stable monolayer self-assembly is not observed anymore below a certain concentration threshold. Consequently, knowledge of both the overall enthalpy change and the concentration threshold grants experimental access to the entropy cost. For TPA monolayer self-assembly on graphite from 9A solution we find a concentration threshold of (120 ± 15) µmol L^{-1}.

At the concentration threshold the thermodynamic driving force for monolayer self-assembly vanishes, i.e., $\Delta G=0$, and consequently $\Delta H=T\Delta S$. Since the enthalpy gain is now precisely known from the Born−Haber cycle, the entropy cost at the concentration threshold can be experimentally quantified and compared to theoretical estimates.

In conclusion, the experimental determination of the concentration threshold for monolayer self-assembly is relatively straightforward but provides important thermodynamical insights. Interestingly, the experimentally determined concentration threshold exceeds the number of TPA molecules required to just cover the graphite surface by a factor of ~6, further evidence for the significance of entropic effects.

4.4.9 Entropy cost vs. enthalpy gain

From equations (2.5.1) and (2.5.3) the values for ΔS_{trans} and ΔS_{rot} of TPA were calculated and are listed in Table 4.1.The $-T(\Delta S_{trans}+\Delta S_{rot})$ contribution to ΔG, associated with adsorption of a TPA molecule at T=298 K, amounts to +94.5 kJ mol^{-1}.

A further entropy contribution arises from dewetting of the graphite, i.e., replacing the solvent wetting layer with the TPA monolayer, because upon desorption of 9A molecules regain entropy. This favorable entropic contribution is estimated from the entropy of melting ($\Delta S_{crystal \rightarrow liquid}$ = 69.5 Jmol^{-1} [172]) and using the same renormalization factor as in equation (4.2). This approach assumes that the 9A wetting layer on graphite substrate is ordered (in agreement with 9A lamellae seen by STM), but the 9A wetting layer on TPA monolayer is disordered (liquid-like) and that the entropy difference between 9A in a monolayer and liquid is comparable to the difference between the 9A crystal and liquid. This appears justified, since the main contributions arise from translational, conformational, and rotational entropy that are all zero both in the crystal and in the monolayer. Accordingly, dewetting causes a favorable entropy contribution of $-T\Delta S_{dewet}$=+17.7 kJ mol^{-1} (renormalized per 1 TPA molecule). Remarkably, the absolute value of this entropy contribution is only slightly smaller than the renormalized enthalpy cost of dewetting ΔH_{dewet} = +18.5 kJ mol^{-1}. Accordingly, the enthalpy cost associated with dewetting is almost fully compensated by the entropy gain. Hence, the influence of the solvent wetting layer on ΔG is almost negligible.

Yet, the resulting total entropy cost of self-assembly $-T(\Delta S_{trans} + \Delta S_{rot} + \Delta S_{dewet})$ = +76.8 kJ mol^{-1} is significantly larger than the enthalpy gain of -7.3 kJ mol^{-1}, as derived from the experimental Born−Haber cycle. According to this estimate, TPA monolayer self-assembly from 9A on graphite should not be thermodynamically favored.

In this simple first approach, however, it was assumed that TPA is dissolved as a single molecule and no further solvation was considered. Yet, such a scenario appears rather unlikely, given that the 9A solvent molecules can likewise form hydrogen-bonded complexes with TPA. It is also well known that fatty acids form hydrogen-bonded dimers in the liquid phase. [173, 174] Accordingly, we postulate that solvated TPA molecules form stable, hydrogen-bonded 9A−TPA−9A complexes with two solvent molecules. This assumption is in accord with the low enthalpy of dissolution, indicating that the hydrogen bond stabilization of the crystal is regained in solution as already discussed above. We also evaluated the possibility of the existence of solvated TPA dimers in solution, i.e., the formation of 9A−TPA−TPA−9A complexes, but find that this process is thermodynamically less favorable (cf. section 4.5).

Owing to the solvation shell of TPA in 9A, upon adsorption of TPA from solution a 9A−TPA−9A complex is dissociated and the two released 9A molecules recombine into a dimer according to the following scheme:

$$\text{9A-TPA-9A}_{sol} \rightarrow \text{TPA}_{ads} + \text{9A-9A}_{sol} \tag{4.3}$$

This solvation also profoundly affects the entropic cost ΔS_{tot} of self-assembly. Both translational and rotational entropy of the 9A-TPA-9A complex are fully lost, but translational and rotational entropy of the 9A-9A dimer are regained. ΔS_{tot} is then given by:

$$\Delta S_{tot} = \Delta S_{trans}(\text{9A-TPA-9A}) + \Delta S_{rot}(\text{9A-TPA-9A}) - \Delta S_{trans}(\text{9A-9A}) - \Delta S_{rot}(\text{9A-9A}) + \Delta S_{dewet} \tag{4.4}$$

	c (µmol L^{-1})	$-T\Delta S_{rot}$ (kJ mol^{-1})	$-T\Delta S_{trans}$ (kJ mol^{-1})	$-T\Delta S_{tot}$ (kJ mol^{-1})
TPA	120	+36.7	+57.8	+94.5
9A-9A	2.84×106	+43.8	+34.7	+78.5
9A-TPA-9A	120	+47.6	+60.9	+108.5

Table 4.1. Contributions of rotational and translational entropy to the free energy for unsolvated TPA molecules, 9A dimers, and hydrogen bonded complexes of TPA and two 9A solvent molecules; A temperature of 298 K was used.

All translational and rotational entropies in equation (4.4) were evaluated according to equations (2.5.1) and (2.5.2) using half of the concentration of 9A in pure 9A for the dimer. An all-trans conformation of the alkane chains was assumed for evaluation of the rotational entropy of both the 9A-9A dimer and the 9A-TPA-9A complex. Curling of the alkane chains equally decreases and increases moments of inertia; hence, conformational isomerism has only a minor effect on rotational entropy. All entropies are summarized in Table 4.1. Accordingly, solvation of TPA by two 9A solvent molecules reduces $-T\Delta S_{tot}$ to +(108.5 – 78.5 – 17.7) kJ mol^{-1}= +12.3 kJ mol^{-1}. This value is in excellent quantitative agreement with the enthalpic gain from the Born-Haber cycle, and thus provides substantial evidence that both solvation and dewetting are major contributions for reduction of the entropy cost of self-assembly.

4.4.10 Temperature threshold of thermodynamical stability

Temperature-induced phase transitions of self-assembled monolayers have been observed experimentally by a temperature-controlled STM[†] at the liquid solid interface [21, 29]. Self-assembly normally reduces the overall entropy (ΔS<0), i.e. ΔG increases with temperature. Since enthalpies do not change in a narrow temperature range, stable monolayers are not observed at temperatures higher than a critical temperature where the entropy loss exceeds the enthalpy gain of self-assembly. Herein, STM measurements are performed at variable temperatures for monitoring reversible thermal desorption of TPA monolayers at the liquid-solid interface. The solution was diluted to a concentration of ~180±40 µmol L^{-1}. Experimentally, it is observed that TPA monolayers desorb, i.e. can no longer be imaged by the STM, once the surface temperature exceeds the critical temperature. When *T* is reduced below the temperature threshold again, TPA monolayers reassemble on the graphite surface. As illustrated in Fig. 4.7, the TPA monolayer are still stable at a surface temperature of 44°C; when the surface temperature is increased by only 1°C to 45°C, the superstructure disappears, and when the substrate temperature is decreased by only 1°C to 44°C, the superstructure reassembles on the surface.

[†] A temperature controlled STM designed by Stephan Kloft was used for the measurement; graphite samples were heated from the bottom and the temperature was controlled by a Eurotherm 2416. This part of the work has not been published yet.

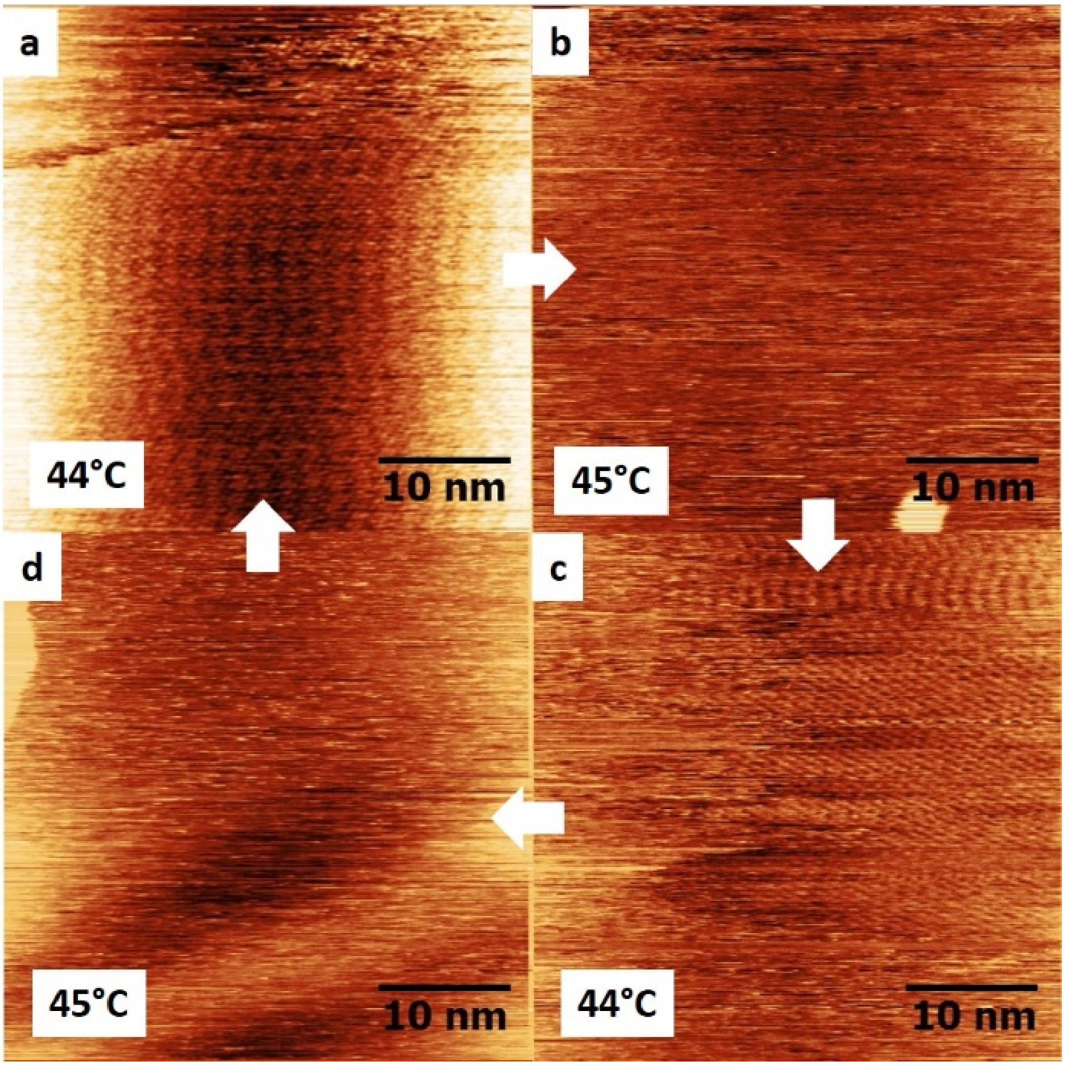

Figure 4.7. STM images obtained at various temperatures. The TPA monolayer disappears when raising the sample temperature by 1°C to 45°C in (b) and (d), and reassembles at 44 °C as shown in (a) and (c). (Images acquired at V_{sample}=-200 mV, *I*=50 pA)

The experimentally determined temperature threshold of self-assembly (317 K) is used to evaluate the corresponding entropy contributions using equations (2.5.1) and (2.5.2); results are listed in Table 4.2. Also, the dewetting entropy gain at the critical temperature is recalculated as -18.8 kJ mol^{-1} (cf. section 4.4), and comes out slightly higher than the dewetting enthalpy loss of +18.5 kJ mol^{-1} (cf. section 4.4). In all experiments, a stable 9A ordered layer was never observed at this temperature. Therefore, the 9A wetting layer on graphite and the adsorption of 9A on top of the TPA monolayer are likely to be disordered and liquid like. Hence, we assume that the difference between 9A-graphite interaction and 9A-TPA interaction is small compared to the overall enthalpy gain. Accordingly, enthalpy gain and entropy cost accompanied by the desorption of the TPA and the wetting of the 9A layer on graphite are not further considered. The free energy change arising from the dewetting of 9A can be neglected. The resulting overall entropy contribution of self-assembly is estimated to be +30.8 kJ mol^{-1}, which is still in very good agreement with the corresponding enthalpy gain of –25.8 kJ mol^{-1} (without dewetting). The higher concentration used in these experiments results in a smaller translational entropy than at the concentration threshold at room temperature. However, the total entropy contribution $-T\Delta S$ increases with temperature. When $-T\Delta S$ exceeds the total enthalpy gain ΔH, monolayers become thermodynamically unstable and desorb from the surface. When the temperature decreases again to point where the entropy contribution $-T\Delta S$ is smaller than ΔH, the superstructure reassembles on the surface (cf. Fig. 4.7 a & c). The process is reversible.

	c (µmol L^{-1})	$-T_{crit}\Delta S_{rot}$ (kJ mol^{-1})	$-T_{crit}\Delta S_{trans}$ (kJ mol^{-1})	$-T_{crit}\Delta S_{tot}$ (kJ mol^{-1})
9A-9A	2.84×10^{6}	+46.6	+36.9	+83.5
9A-TPA-9A	180	+50.6	+63.7	+114.3

Table 4.2. Translational and rotational entropy contribution of 9A-TPA-9A and 9A-9A at the temperature threshold 317K.

For thorough comparison to the case of concentration threshold at the room temperature, we need to consider the dewetting of the 9A solvent. By using the melting entropy of the 9A crystal again, the entropic contribution is increased to $-T_{crit}\Delta S_{dewett}$ = –18.8 kJ mol^{-1} because of the higher temperature as compared to previously used room temperature. The total entropy contribution including the dewetting decreases to $-T\Delta S_{tot}+T\Delta S_{dewett}$ = +30.8–18.8 kJ mol^{-1} = +12.0 kJ mol^{-1}. This value is almost equal to the entropy contribution at the concentration threshold at room temperature, +12.3 kJ mol^{-1}. The difference is negligible, especially when compared to the error bars of the enthalpy measurements. At the critical conditions, i.e at the concentration threshold and the temperature threshold, $\Delta H \approx T\Delta S$. Hence, the perfect agreement of these two entropy contributions provides further confidence for the low temperature dependence of the enthalpy change.

In conclusion, we observed the temperature induced desorption and reassembly of monolayer at the solution-solid interface for the first time. A sharp transition takes place in a narrow temperature range of 1°C. The results provide direct and solid evidence for the relatively low desorption barrier, i.e. the low enthalpy gain from the solution to the interfacial monolayer. For the case of desorption in UHV, the desorption rate is almost negligible at ~90°C, significant desorption was detected by the QMS at ~100°C. The quantitatively thermodynamics provides the rationale of formerly reported dynamic exchange phenomena [175, 176], and the temperature induced phase transition which are normally accompanied by a change of molecular density on the surface [21].

In conclusion, we demonstrated that desorption and reassembly of the self-assembled monolayer at the solution-solid interface can be observed experimentally. The critical temperatures give the access to a quantitative entropy determination. This enables a direct comparison with the entropy contribution estimated based on the concentration threshold at room temperature. The two entropy contributions are in perfect agreement, proving the low temperature dependence of the enthalpy gain of self-assembly.

4.5 Supporting information

4.5.1 Experimental Details

Terephthalic acid (TPA, purity > 98%) and 1-nonanoic acid (9A, purity ≥ 96%) were acquired from Sigma-Aldrich and used without further purification.

STM Experiments

STM experiments were conducted with a home-built drift optimized microscope driven by an ACS500 controller from attocube systems AG. TPA monolayers were prepared by applying 4.0 µL solution onto freshly cleaved graphite and imaged directly at the liquid-solid interface with the STM tip immersed into solution. STM tips were prepared by mechanical cutting a 90/10 Pt/Ir wire (diameter 0.25 mm). Precise unit cell parameters were obtained by calibration with the underlying graphite lattice as described elsewhere in more detail.[11]

The concentration threshold for TPA monolayer self-assembly was determined from large scale STM images (100 × 100 nm²). Four different concentrations 215.0 µmol L^{-1}, 161 µmol L^{-1}, 134 µmol L^{-1}, 108 µmol L^{-1} were probed. Self-assembly of stable TPA monolayers was still observed for 134 µmol L^{-1}, but reliably absent for

108 µm L^{-1}. Since self-assembly can become diffusion limited at lower concentrations, an influence of slow kinetics was excluded by prolonged waiting times.

Effusion Rate vs. Crucible Temperature Measurements (Sublimation Enthalpy)

The TPA sublimation enthalpy was derived from a temperature dependent measurement of the effusion rate from a home-built Knudsen cell in a high-vacuum chamber. To this end, a quartz crystal microbalance (QCMB, nominal eigenfrequency 6 MHz, diameter 1.4 cm) is integrated into the shutter of the Knudsen-cell (cf. section 2.1). [86] The crucible temperature was measured with a type K thermocouple and held constant with a temperature controller (Eurotherm 2416). The close proximity of the quartz crystal and its large size in relation to the aperture size of the Knudsen cell renders the setup highly sensitive. The eigenfrequency shift Δf of the QCMB as a function of time Δt was recorded for 5 different crucible temperatures ranging from 100 °C to 120 °C using commercial circuitry (Q-pod, INFICON).

UV-vis Absorption Spectroscopy (Dissolution Enthalpy)

Solubility measurements of TPA in 9A as a function of temperature yield the enthalpy of dissolution (cf. section 2.3). TPA solubility, i.e. the saturation concentration, is determined by UV-vis absorption spectroscopy using spectra of pure solvent at the respective temperatures as reference. TPA absorption spectra in nonanoic acid were acquired between 30 °C and 42 °C. Therefore, an USB4000 Miniature Fiber Optic Spectrometer from Ocean Optics, an ISS-UV/VIS light source, and a quartz glass cuvette (Hellman 100-QS) with an optical path length of 10 mm were used. The cuvette was heated by two sideways mounted Peltier elements (TEC1-03504). The temperature of the solution was measured by a type K thermocouple that was immersed into the cuvette. The temperature was held constant by a temperature controller (Eurotherm 2416). For all temperatures, the solutions were in equilibrium with a small amount of TPA sediment at the bottom of the cuvette. Equilibration times of 24 h were applied for each temperature.

Temperature Programmed Desorption (Monolayer Binding Energy)

The desorption enthalpy of TPA monolayers with respect to vacuum was determined by temperature programmed desorption (TPD, cf. section 2.2). Experiments were conducted in a dedicated ultra-high vacuum (UHV) system. A QMA 125 quadrupole mass spectrometer from Balzers equipped with a secondary electron multiplier was used for detection of the desorbing TPA molecules at 149 amu, i.e. the strongest peak in the TPA mass spectrum. The surface temperature was measured with a type K thermocouple directly mounted on the graphite surface.

The graphite substrate was prepared by heating at 800 K for 30 minutes prior to each experiment. TPA monolayers were deposited from a Knudsen cell with a crucible temperature of 110 °C for 15 minutes. These deposition parameters reproducibly yielded coverages just below one monolayer. For slightly longer deposition times multilayer peaks appeared in the desorption traces. During deposition the substrate was held at 300 K and cooled to 250 K prior to the desorption experiment with a closed cycle helium cooler. In the desorption experiment, the surface temperature was linearly ramped from 250 K up to 550 K by means of a temperature controller (Eurotherm 2416). Three sets of experiments were performed with three different heating rates of 0.25 K s^{-1}, 0.42 K s^{-1} and 0.84 K s^{-1}. Binding energies were evaluated from the data according to the complete analyze method (cf. section 2.2).[177]

4.5.2 Additional STM Results

This observation of an ordered monolayer of nonanoic acid at the solid-liquid interface, as shown in Fig. 4.8, is in agreement with similar observations of ordered monolayers of longer-chain alkanoic acids reported in the literature. [178-180]

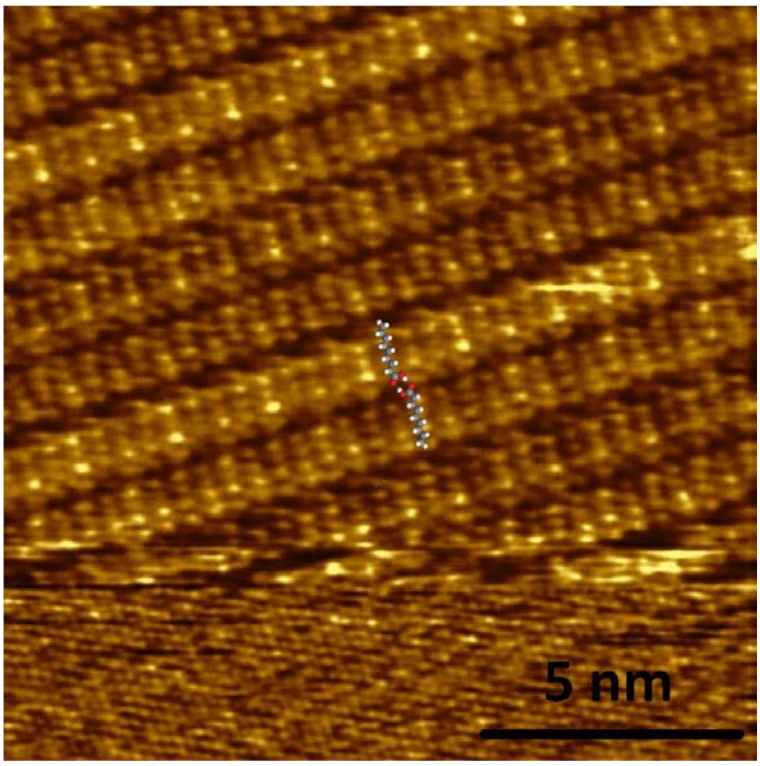

Figure 4.8. STM topography of a self-assembled nonanoic acid monolayer at the graphite-liquid nonanoic acid interface. In this split image the upper part shows the nonanoic acid monolayer, whereas in the lower part the graphite substrate was imaged with decreased tunneling resistance. This image was acquired after applying pure nonanoic acid to a freshly cleaved graphite substrate. The overlay represents a hydrogen bonded nonanoic acid dimer, i.e. the basic motif of this structure.

4.5.3 Computational Details and Additional Results

The energies of two-dimensional (2D) and three-dimensional (3D) TPA assemblies, the energy of TPA adsorbed on graphite, and the energies of nonanoic acid (9A) adsorbed on graphite and on a TPA 2D monolayer were calculated using molecular mechanics (MM). For calculation of the solvation energy of TPA in 9A classical molecular dynamics (MD) was used. The simulations were performed using the Tinker code [118] and the MM3 force field, [119, 120] with the hydrogen bond parameters adjusted to reproduce the energy and length of the double hydrogen bond in a carboxylic acid cyclic dimer (r = 1.75 Å, ε_{HB} = 7.78 kcal mol^{-1}). [120] MD simulations were run in the canonical (NVT) ensemble at 298 K using the Nose-Hoover thermostat, with the integration time step of 1 fs. The “rattle” algorithm was used to constrain all covalent bonds to H atoms to their ideal bond length.

2D Monolayer of TPA

The lowest-energy structure of the TPA 2D monolayer was found by scanning through a range of realistic values of the lattice parameters A, B, and γ. First, the value of the lattice parameter A (the intermolecular distance along the one-dimensional (1D) chains of hydrogen bonded TPA molecules) was optimized; then, at the fixed optimum A value, the lattice parameter B (distance between two TPA molecules in neighboring chains) and the angle γ were varied simultaneously in a range of values similar to the experimental values for the TPA bulk crystal. [121] At first (in the initial scan in the range B = 7.3 Å - 8.5 Å and γ = 115° - 135°), the step was 0.1 Å for varying the B parameter and 1° for γ, then (in the region close to the energy minimum) 0.01 Å for B and 0.5° for γ. Finally, we varied A in a 0.05 Å range to check that the optimum A value is the same in the 1D and 2D structure.

3D Crystal Structure of TPA

The computational search for the lowest-energy 3D TPA structure was based on the optimized 2D structure described above and took into account the experimental X-ray TPA crystal structure. [121] Thus, the aim was not to predict possible TPA polymorphs but to verify that the MM3 description of the TPA crystal structure is accurate and reliably reproduces the experimental structure.

First, the A, B, and γ lattice parameters were fixed at their 2D values, while the parameters α, β, and C were varied simultaneously, first on a coarse grid (in the range of C = 3.5 – 4.75 Å with the step of 0.25 Å and then 0.1 Å, and in the range of α = 70° – 130° and β = 55° – 100° with the step of 5°), then, when close to the energy minimum, on a fine grid (0.01 Å for C, 1° for α and β). Finally, all six lattice parameters were varied simultaneously within ± 0.1 Å and ± 3° from the identified optimum values (a wider range was needed for the B parameter because of the very flat potential energy surface for the intermolecular dispersion interactions) to adjust the lattice vectors of the 2D lattice to the 3D case. The computed lattice parameters were A = 9.37 Å, B = 7.70 Å, C = 3.56 Å, α = 83°, β = 74°, γ = 131°.

A more general approach to the crystal structure search should take into account that a 3D structure is not necessarily based on 2D layers of molecules. Indeed, the experimental X-ray study found two polymorphs of TPA [121]: form I is based on 2D layers of molecules lying in the plane defined by A, B, and γ, while form II does not contain such 2D layers. The approach described above finds form I of TPA. Additionally, we looked for a 3D structure similar to form II. In this search, lattice parameters B, C, α,

β, and γ were varied simultaneously (in a 1.8 Å and 20° – 60° range around the experimental values from Ref. [121]). This necessarily required lower accuracy (0.2 Å, then 0.1 Å for B and C, 5° and then 1° for α, β and γ). In this way, a second energy minimum was found – a 3D structure similar to form II, with computed lattice parameters A = 9.37 Å, B = 5.1 Å, C = 5.4 Å, α = 82°, β = 136°, γ = 106°, cf. experiment: A = 9.54 Å, B = 5.34 Å, C = 5.02 Å, α = 86°57', β = 134°39', γ = 94°98'.[121]

Adsorption Energy of TPA on Graphite

In order to calculate the adsorption energy of TPA on graphite, a TPA molecule was placed on a large (14 × 14 unit cells, 392 C atoms) hydrogen-terminated graphene sheet, large enough to avoid TPA interactions with sheet edges. The carbon atoms of the graphene sheet and the x and y positions of the adsorbate's carbon atoms were fixed. To calculate the potential energy surface for TPA adsorption on graphite, we considered a 2D grid of TPA positions with 0.1 Å spacing, covering the entire graphite unit cell. In addition to varying the position, the orientation of the molecule was varied between 0° and 60° in steps of 5°.

To test the accuracy of the MM3 force field for calculation of adsorption energies of aromatic organic molecules, we also calculated adsorption of benzene on graphite as a well-studied test system. The calculated adsorption energy of benzene in the lowest-energy "stack" adsorption site was -42.4 kJ mol^{-1} (-0.44 eV), in good agreement with experimental energies -0.39 .. -0.50 eV measured by gas chromatography [181] and thermal desorption [182] and with the value -0.495 eV calculated using van der Waals density functional theory (vdW-DFT). [183] However, the corrugation of the potential energy surface in our MM3 calculations is very small: 0.004 eV (0.36 kJ mol^{-1}) difference between the lowest-energy "stack" (similar to graphite AB stacking) and highest-energy "top" (similar to graphite AA stacking) structures, cf. 0.05 eV given by density functional theory (DFT) within the local-density approximation (LDA); [184] we are not aware of calculations of different benzene adsorption sites using higher level of theory, such as vdW-DFT. This test shows that MM3 adsorption energies are of the correct order or magnitude, but the energy difference between high- and low-energy adsorption sites may be underestimated.

Solvation Energy of TPA in 9A

The enthalpy of solvation of TPA in nonanoic acid (9A) was obtained from MD simulations as the energy difference between TPA surrounded by 9A solvent molecules and TPA in the gas phase. The solvent system contained 200 × 9A molecules in a box with periodic boundary conditions. The size of the box was chosen so as to reproduce the literature density of 9A (0.9057 g/cm³). The initial solvent structure was obtained by annealing from 1000 K down to 300 K for 0.7 ns (time step 2 fs).

Two approaches were used to create solvent-solute (9A-TPA) systems: (i) one TPA molecule was added to the box of 200 annealed 9A molecules, and the box size was adjusted to include the volume of the TPA molecule (using the experimental TPA density 1.57 g mol^{-1} [121]), (ii) one 9A molecule was removed and substituted with a TPA molecule, and the box size was adjusted according to the TPA and 9A molecular volume. One “added TPA” and two “substituted TPA” structures were constructed. The TPA:9A ratios of 1:200 and 1:199 correspond to solute concentrations of 28.6 .. 28.8 mMol L^{-1}. These are much larger than the concentrations 0.1 .. 0.2 mMol L^{-1} used in experiment, but the experimental concentrations would require $\approx 6\times10^4$ solvent molecules ($\approx 1.7\times10^6$ atoms) and are not accessible to calculations. The solvent-solute systems were annealed again from 600 K to 300 K in 0.2 ns.

Then, MD simulations (NVT ensemble, 298 K) were performed on the TPA + 200 × 9A and TPA + 199 × 9A structures, on the pure solvent (200 × 9A) systems and on an isolated TPA molecule in a large box. It is known that calculated molecular properties, such as conformations of peptides and carbohydrates, can be dependent on the force field used. [185, 186] To make sure that there is no systematic error in our description of intermolecular interactions, two different force fields were used in the MD calculations: MM3 as described above, and the CHARMM27 force field [122] widely used for simulations of organic and biomolecules (e.g. a recent paper on alkylcatechols at the 9A-graphite interface [123]).

Two separate MD simulations of the pure solvent were done using each force field. Six MD simulations of the solvent with solute were done using MM3 (two “added TPA” and four “substituted TPA” – three structures with and three without the additional annealing step), and four simulations using CHARMM27 (two “added TPA” and two “substituted TPA”).

To monitor the equilibration of the system, the mean values of potential energy were calculated every 0.5 ns. The structures were considered equilibrated if their potential energy changed by ≤ 4 kcal mol^{-1} in 0.5 ns. This required 4 ns - 6 ns long MM3 simulations and 5 ns - 6.5 ns long CHARMM27 simulations. The solvent + solute structures with and without the additional annealing step had very similar energies already after 0.5 ns - 3 ns of MD simulations, while the different starting geometries (substituted or added TPA) lead to noticeably different energies. The energy of an isolated TPA molecule was converged within the first 0.5 ns.

The solvation energy was calculated as $E_{solv} = E_{TPA+9A} - n \times E_{9A}/200 - E_{TPA}$, where E_{TPA+9A} is the solvent-solute potential energy, E_{9A} is the pure solvent potential energy (the mean value of two separate simulations of 200 solvent molecules), E_{TPA} is the isolated (gas-phase) solute energy, and n is the number of solvent molecules (200 or 199) in the solvent + solute system. The final solvation energy was the mean value of E_{solv} for the six solvent + solute systems.

4.5.4 Energy of the 9A Wetting Layer

The energy of the 9A wetting layer was obtained by separately calculating the binding energy of a free standing 2D monolayer of 9A and the adsorption energies of 9A on graphite and on the TPA monolayer, similar to the calculations described above for the TPA monolayer binding and adsorption energy.

9A 2D Monolayer

Two types of 2D monolayers of 9A were considered: lamella containing two hydrogen-bonded 9A molecules in a unit cell (Fig. 4.9a) and interdigitated lamella containing four 9A molecules (two hydrogen-bonded pairs) in a unit cell (Fig. 4.9b). The lowest-energy structures of these monolayers were found by scanning through a range of realistic values of the lattice parameters A, B, and γ.

The MM calculations find that the dimer-based lamella (lattice parameters A = 27.7 Å, B = 5.4 Å, γ = 117°, the surface area occupied by one 9A molecule is 66.48 Å^2) has the binding energy with respect to the gas phase of -43.3 kJ mol^{-1} per one 9A molecule and is slightly more stable than the interdigitated lamella (binding energy -42.5 kJ mol^{-1} per one 9A, lattice parameters A = 28.0 Å, B = 10.0 Å, γ = 99°).

Note that experimental studies of long-chain fatty acids on graphite report interdigitated monolayer structures for 9A and similar molecules, [166],[179] although a non-interdigitated dimer-based lamella structure has been reported as well. [180] On the other hand, 3D crystals of fatty acids are composed of non-interdigitated dimers. [166] This difference in structure suggests that the graphite substrate subtly affects the 9A monolayer self-assembly – a factor not included in these calculations. For simplicity, the calculated structure and energy of the non-interdigitated dimer-based monolayer (Fig. 4.9a) are used in the further analysis.

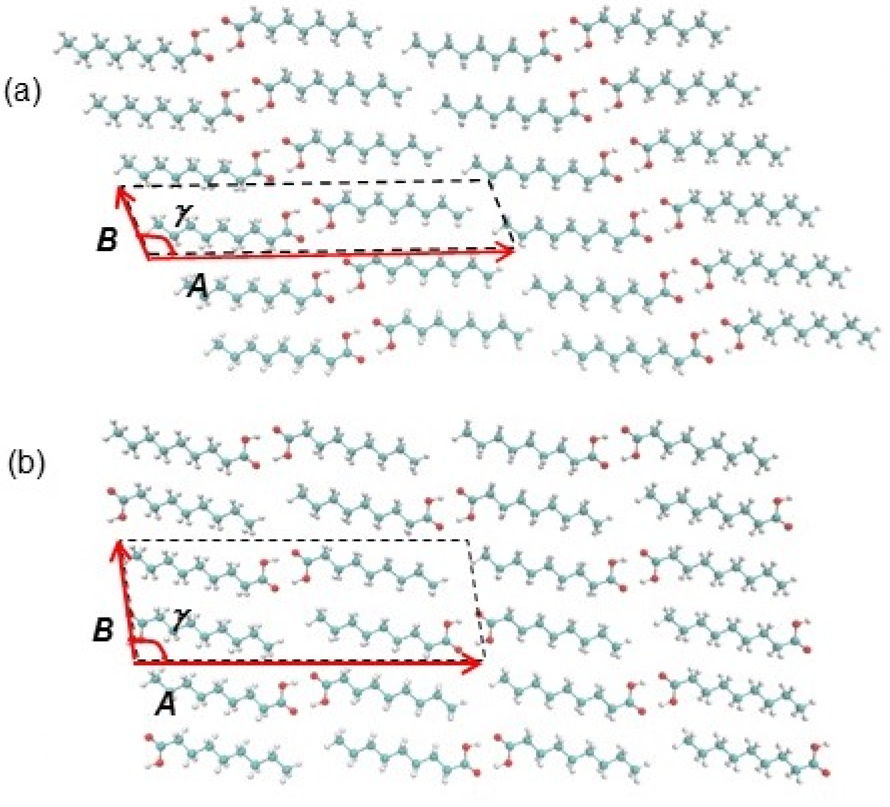

Figure 4.9. Structures of simulated 2D monolayers of 9A: (a) monolayer composed of lamellae with a pair of hydrogen-bonded 9A molecules in a unit cell; (b) monolayer composed of interdigitated lamellae with four 9A molecules in a unit cell.

Adsorption Energy of 9A on Graphite

The adsorption energy of 9A in graphite was calculated in a similar way to the adsorption energy of TPA on graphite. A dimer of 9A (the basic repeat unit of the 9A 2D monolayer in Fig. 4.10) was placed on a large (24 × 24 unit cells, 1152 C atoms) hydrogen-terminated graphene sheet, large enough to avoid the adsorbate's interactions with sheet edges. The adsorption geometry shown in Fig. 4.10 for a single 9A molecule with the carbon atoms' plane parallel to the graphene plane and the alkane tail aligned along the ⟨100⟩ (zigzag) direction of graphite yields the lowest energy.

To calculate the potential energy surface for 9A adsorption on graphite, we considered a 2D grid of 9A dimer positions with 0.2 Å spacing, covering the entire graphite unit cell. The carbon atoms of the graphene sheet and the *x* and *y* positions of the adsorbate's carbon and oxygen atoms were fixed. The mean value of adsorption energy for a 9A dimer was found to be -124.8 ± 1.1 kJ mol^{-1} (equivalently, -62.4 ± 0.6 kJ mol^{-1} per one 9A molecule).

Adding together this adsorption energy and the binding energy of the 9A obtained above (-43.3 kJ mol^{-1}), the total adsorption energy of the 9A wetting layer is -105.7 kJ mol^{-1} per one 9A molecule.

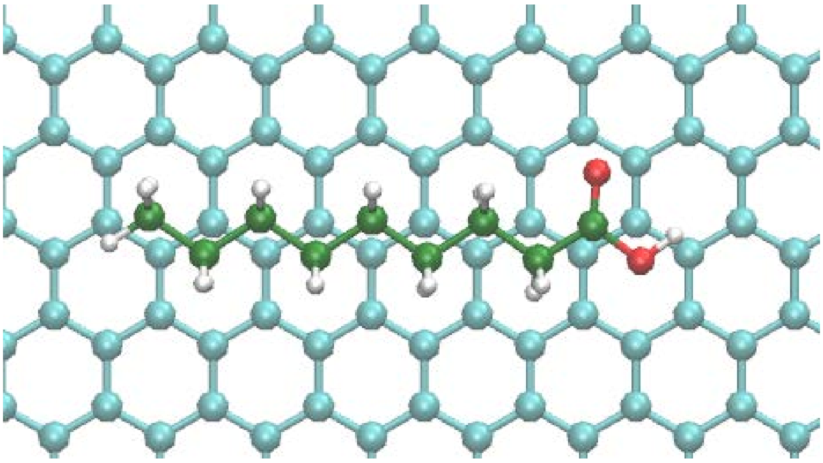

Figure 4.10. Lowest-energy adsorption geometry for a 9A molecule on graphite: Carbon atoms of graphite are in turquoise, carbon atoms of 9A in green, oxygens in red, hydrogens in white.

Adsorption Energy of 9A on TPA

A dimer of 9A was placed on a TPA layer consisting of 8 × 8 periodically repeated TPA molecules, which is large enough to avoid interaction with replica 9A dimers. The TPA layer was fixed; the *x* and *y* positions of the 9A dimer's carbon and oxygen atoms were fixed. The dimer's position with respect to underlying TPA (covering one TPA unit cell with 0.2 Å spacing) and the dimer's orientation (0-180° in steps of 30°) were varied. The mean value of the adsorption energy is -40.7 kJ mol^{-1} per one 9A molecule (the energy varies between -42.7 and -39.9 kJ mol^{-1}, depending on the adsorbate's position and orientation).

There is no experimental or theoretical information on the structure of the 9A solvent above the TPA monolayer, as far as we are aware. It is most likely that this 9A overlayer is disordered and liquid-like. Our MD calculations of bulk 9A on a fixed TPA layer show that 9A molecules tend to be parallel to the TPA layer, but no ordered arrangement of 9A has been obtained. It is difficult to provide a reliable estimate of the interaction energy at this disordered and dynamic interface, either experimentally or computationally. As the upper estimate of the TPA/9A interaction, we use the energy of an ordered 9A monolayer above a TPA monolayer, calculated as a sum of the 9A monolayer binding energy and 9A adsorption energy on TPA: -43.3 + (-40.7) = -84.0 kJ mol^{-1} according to the MM3 calculations.

4.5.5 TPA Dimers Formation in Solution

Partial dissolution, i.e. the formation of solvated complexes consisting of more than one TPA molecule, would substantially affect the entropy balance. In order to evaluate this possibility we estimate the entropy gain associated with formation of solvated 9A-TPA-TPA-9A complexes from TPA crystals according to the following scheme:

$$2\ \mathrm{TPA_{crystal}} + \mathrm{9A\text{-}9A_{solution}} \rightarrow \mathrm{9A\text{-}TPA\text{-}TPA\text{-}9A_{solution}} \qquad (4.7)$$

Analogous to the consideration in section 4.4, translational and rotational entropy of TPA are set zero in the crystal. Hence, upon partial dissolution translational and rotational entropy of the 9A-TPA-TPA-9A complex are gained, whereas translational and rotational entropy of the involved 9A-9A dimer are lost. The overall entropy $\Delta S_{partial}$ of this partial dissolution process is given by:

$$\Delta S_{\mathrm{partial}} = \Delta S_{\mathrm{trans}}(\text{9A-TPA-TPA-9A}) + \Delta S_{\mathrm{rot}}(\text{9A-TPA-TPA-9A}) - \Delta S_{\mathrm{trans}}(\text{9A-9A}) - \Delta S_{\mathrm{rot}}(\text{9A-9A}) \qquad (4.8)$$

Both rotational and translational entropies of the 9A-TPA-TPA-9A complex were estimated by the same method as described in the manuscript using the hard cube approximation for the free volume of the solvent. For the translational entropy half of the TPA concentration was used. All values including those of 9A-TPA-9A complex as well as 9A-9A dimer are summarized in Table 4.3.

Accordingly, the entropy gain for partial dissolution, i.e. the release of 9A-TPA-TPA-9A complexes amounts to 0.5 × (-113.8 kJ mol^{-1} - (-82.8 kJ mol^{-1})) = -15.5 kJ mol^{-1}. The factor 0.5 normalizes this entropy gain to the number of TPA molecules, thereby facilitating a direct comparability to the 9A-TPA-9A complexes.

The corresponding entropy gain for formation of 9A-TPA-9A complexes corresponds to (-103.9 kJ mol^{-1} - (-82.8 kJ mol^{-1})) = -21.1 kJ mol^{-1}.

Since in both types of complexes all carboxylic acid groups of TPA are saturated with hydrogen bonds, it is a reasonable assumption that enthalpies of dissolution per TPA molecule are comparable in both types of complexes. Accordingly, the gain in free energy per TPA molecule for partial dissolution (formation of 9A-TPA-TPA-9A) is significantly lower (~5 kJ mol^{-1}) than for complete dissolution (formation of 9A-TPA-9A). Consequently, partial dissolution is a conceivable competing process, but is thermodynamically less favorable. Based on a similar argumentation, partial dissolution which results in the formation of even larger complexes consisting of more than two TPA molecules becomes even less thermodynamically favorable, because the enthalpy cost scales linearly with the number of TPA molecules, whereas the entropy gain increases sublinearly due to the logarithmic dependence of both rotational and translational entropy.

	c (μmol L^{-1})	$-T\Delta S_{rot}$ (kJ mol^{-1})	$-T\Delta S_{trans}$ (kJ mol^{-1})	$-T\Delta S_{tot}$ (kJ mol^{-1})
9A-9A	2.84×10^{6}	-43.0	-35.2	-82.8
9A-TPA-9A	120	-47.6	-60.9	-103.9
9A-TPA-TPA-9A	60	-49.8	-64.0	-113.8

Table 4.3. Contributions from rotational and translational entropies to the free energy evaluated for different complexes. Note that dissolution is considered, i.e. the entropies are gained upon dissolution and thus $\Delta S>0$. A temperature of 298 K is used for the calculation.

4.6 Conclusion and Summary

An adapted Born-Haber cycle was employed to deduce not only the overall enthalpy change for self-assembly of TPA monolayers at the nonanoic acid-graphite interface, but also the individual enthalpy contributions of the various interactions involved in this process. In their initial state, TPA molecules are solvated in 9A and then become incorporated in the interfacial monolayer, as their final state. Since the associated overall enthalpy change is particularly small, and thus experimentally difficult to assess by calorimetric methods, a detour was taken via well-defined reference states with accessible enthalpy differences. To this end, enthalpy differences between crystal and gas phase, crystal and solution, as well as monolayer and gas phase were both measured and evaluated by MM and MD simulations. For all enthalpy differences the agreement between experiment and theory is remarkable, thereby providing high confidence in the reliability and accuracy. Since the graphite substrate is initially covered by an ordered 9A solvent monolayer, a further enthalpy contribution arises from dewetting and was estimated by MM simulations.

The most surprising result is that the effective driving force – the enthalpy difference between a self-assembled monolayer and an initially solvent-covered substrate and dissolved TPA molecules – is astonishingly low, due to an efficient stabilization of TPA in solution and the enthalpy cost of dewetting. Consequently, the supernatant liquid phase considerably lowers the TPA desorption barrier to only a few percent of the corresponding vacuum desorption barrier. Thereby for the first time a quantitative rationale is provided for abundantly observed phenomena at the liquid-solid interface that are associated with the vertical mobility of adsorbed molecules, i.e. the possibility of desorption, even of larger compounds at room temperature. [168-170]

The precise quantification of the enthalpic driving force also enables a quantitative comparison with the entropy change of self-assembly as estimated by an established partition scheme. This comparison reveals that solvation through formation of hydrogen bonded solute-solvent complexes is an important contribution to lowering the entropy cost. Interestingly, a further significant favorable entropic contribution arises from dewetting the substrate, because released 9A solvent molecules regain entropy. Entropic contributions are extremely important in self-assembly, and we show that the theoretically estimated entropy cost of self-assembly at thermodynamic equilibrium is in excellent agreement with the overall enthalpy gain, as estimated both by experimental and theoretical methods. In summary, the liquid phase not only lowers the enthalpy gain of self-assembly, but by the same token also reduces the entropy cost, and thus renders spontaneous self-assembly thermodynamically favorable.

In addition, we observed the reversible desorption and reassembly of monolayer at the solution-solid interface by temperature-dependent STM measurements. A sharp transition takes place at the temperature of 45°C, in a narrow temperature range of ±1°C. These results provide direct evidence of the low desorption barrier as derived from the Born-Haber cycle, i.e. the low enthalpy gain of self-assembly at the solution-solid interface.

Chapter 5: Thermodynamics of 4, 4’-stilbenedicarboxylic acid monolayer self-assembly at the nonanoic acid-graphite interface

Wentao Song, Natalia Martsinovich, Wolfgang M. Heckl, and Markus Lackinger, Thermodynamics of 4, 4’-stilbenedicarboxylic acid monolayer self-assembly at the nonanoic acid-graphite interface. Phys. Chem. Chem. Phys., 2014. **16**(26): p. 13239-13247, http://dx.doi.org/10.1039/C4CP01147C. Reproduced and adapted by permission from the PCCP Owner Societies.

5.1 Abstract

A direct calorimetric measurement of the overall enthalpy change associated with self-assembly of organic monolayers at the liquid–solid interface is for most systems of interest practically impossible. In chapter 4 we proposed an adapted Born–Haber cycle for an indirect assessment of the overall enthalpy change by using terephthalic acid monolayers at the nonanoic acid–graphite interface as a model system. To this end, the sublimation enthalpy, dissolution enthalpy, the monolayer binding enthalpy in vacuum, and a dewetting enthalpy are combined to yield the total enthalpy change. In the present study the Born–Haber cycle is applied to 4, 4’-stilbenedicarboxylic acid monolayers. A detailed comparison of these two aromatic dicarboxylic acids is used to evaluate and quantify the contribution of the organic backbone for stabilization of the monolayer at the nonanoic acid–graphite interface.

5.2 Introduction

Supramolecular self-assembly is a ubiquitous approach for the bottom-up fabrication of functional nanostructures. As a foundation for a targeted and efficient fabrication it is important to study and understand the mechanisms and driving forces of supramolecular self-assembly. [13-16] Two-dimensional surface supported self-assembly has attracted special interest due to both conceptual and analytical advantages. On the one hand, surfaces provide an interface and support for these nanostructures, an important prerequisite for applications in sensorics, catalysis, and organic electronics. [6, 7, 187] On the other hand, it is relatively straightforward to characterize surface-supported monolayers in real space by high resolution Scanning Probe Microscopy. [9-12]

Owing to the high relevance for applications and the ease of preparation, a great part of self-assembly research is focused on the liquid-solid interface. [18, 19] A number of experiments have demonstrated major influences of the liquid phase on both the thermodynamics and kinetics of interfacial self-assembly. [20-22, 30] For instance, in comparison to the vacuum-solid interface, desorption barriers are considerably lowered, giving rise to vertical mobility of the building blocks. Consequently, self-assembly at liquid-solid interfaces is highly dynamic, and many systems represent the thermodynamically most favourable structure corresponding to the lowest Gibbs free energy. [9, 11, 12, 24, 25] Accordingly, thermodynamical approaches were successfully applied to understand monolayer structure selection and formation processes. The driving force for self-assembly is a gain in free energy, i.e. $\Delta G = \Delta H - T\Delta S < 0$. Thus, for a fundamental understanding of self-assembly, a quantitative assessment of ΔG is inevitable. For the most part, binding enthalpy is gained by forming more and stronger bonds in the self-assembled structure, while entropy is reduced because the building blocks lose degrees of freedom. However, notable contributions to free energy can also arise from desolvation and dewetting processes, and are normally associated with an enthalpic cost and an entropic gain.

A common approach to theoretically determine the thermodynamically most stable structure depending on the solute concentration is based on the equality of the chemical potentials in solution and within the monolayer in thermodynamical equilibrium. By using established concepts for the concentration dependence of the chemical potential, e.g. ideal or regular solutions, the free energy of competing monolayer structures can be evaluated and compared. This approach was successfully employed to explain the concentration dependent transition from a densely packed to a porous polymorph [27] or the emergence of different bimolecular phases. [20] Recently De Feyter *et al.* extended this approach by using the concentration dependence of the transition temperature of a structural phase transitions as additional experimental input for a thermodynamical model that yields monolayer enthalpies and entropies. [29] Alternatively, the monolayer free energy can be assessed by a separate evaluation of ΔH and ΔS, [21] whereby ΔH can be obtained from simulations. Since most molecules of interest for monolayer self-assembly at the liquid-solid interface are relatively large, molecular mechanics (MM) or molecular dynamics (MD) are often the methods of choice. MM and MD simulations have been successfully applied to a wide range of systems. [20, 21, 28, 31, 33, 54] These simulations, however, neglect the supernatant liquid phase and remain limited to the quantification of lattice energies. Moreover, both MD and Monte Carlo (MC) simulations are valuable tools for understanding monolayer formation and selection processes. [33, 35-37, 188] For MC appropriate modelling of the intermolecular interactions is crucial, since the outcome is extremely sensitive to simulation parameters. On the other hand, MD as an atomistic simulation technique, does not require mapping of the molecular building blocks onto a model, but sensitively depends on parameters of the underlying force field. A disadvantage of MD is its comparatively large computational cost, limiting both system size and simulation time spans.

Apart from MD and to some degree MM simulations, most theoretical approaches rely on precise structural data as experimental input. [20, 21, 28] At the liquid-solid interface these data are typically acquired by STM, and especially monolayer structures of larger compounds with recognizable geometric shape can be resolved with high precision. An unsolved simulation challenge arises for porous monolayers due to possible coadsorption of solvent molecules within the pores. [20, 21, 29] Unfortunately, in most cases these solvent molecules cannot be discerned in STM images, hence no structural data is available for a theoretical assessment of the associated non-negligible enthalpy contribution.

Equilibrium approaches, however, are only appropriate if the experimental structure represents the thermodynamically most stable structure. Especially for larger molecules or strongly interacting surfaces, self-assembly can also become kinetically hindered, resulting in the emergence of metastable phases. [22] For such systems, it is advisable to check whether an irreversible conversion from a possible metastable to a more stable phase can be induced by providing additional thermal energy. [189], [190] This does not require exceptional instrumentation, as it can straightforwardly be done by simple ex-situ heating.

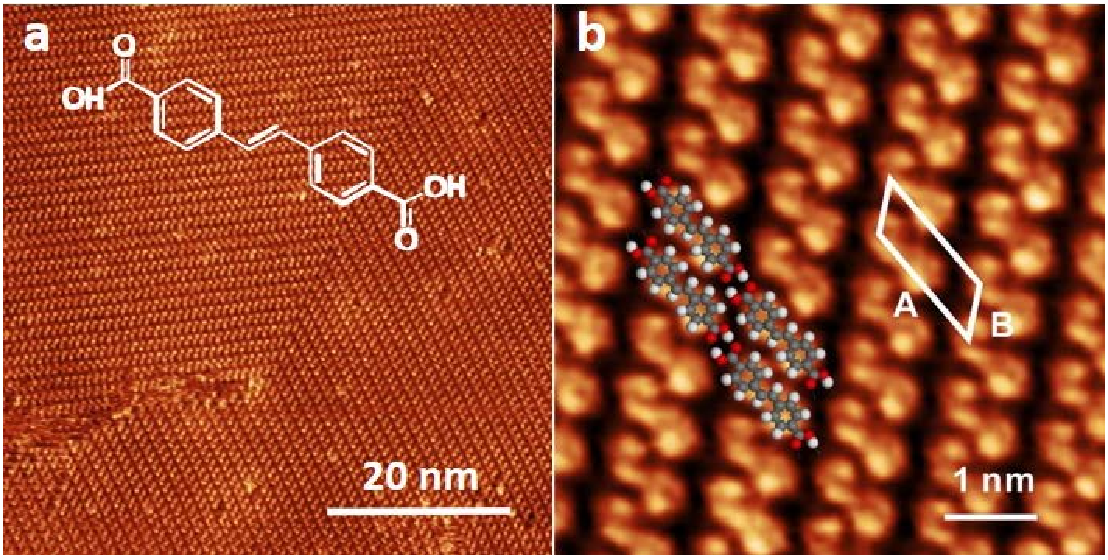

Figure 5.1. STM images of SDA monolayer at the nonanoic acid-graphite interface: (a) overview image 61.5×61.5 nm^2, I= 60 pA, V_{sample}= 300 mV; (b) high resolution image (6.5×6.5 nm^2, I=80 pA, V_{sample}= 250 mV). The unit cell is indicated by the white lines, corresponding to A= (16.1± 0.1) Å, B= (7.5 ±0.1) Å, γ=52° ± 1°. SDA molecules are depicted to scale in the overlay.

In the present study we utilize the Born-Haber cycle method to evaluate the thermodynamics of 4,4'-stilbenedicarboxylic acid (SDA) monolayer self-assembly (cf. inset in Fig. 5.1 for structure) at the nonanoic acid – graphite interface. Similar to previously studied TPA (cf. chapter 4), SDA is a dicarboxylic acid, however, with an extended aromatic backbone, consisting of two phenyl rings interconnected by an ethenyl unit. In this respect it is interesting to quantify the influence of the extended aromatic system on the overall enthalpic stabilization. In the following, each individual enthalpy contribution to the Born-Haber cycle is discussed separately and eventually combined to yield the overall enthalpy change. This can then be compared to the entropy cost of self-assembly, as estimated by using a partition scheme based on established methods. To quantify the influence of polyaromatic systems, it is also instructive to compare the thermodynamics of SDA monolayer self-assembly to previously studied TPA.

5.3 Methods

5.3.1 Experimental

SDA and 1-nonanoic acid (9A) were obtained from ABCR and Sigma Aldrich and used without further purification. STM experiments were carried out with a home-built instrument driven by a commercial ASC500 controller from attocube systems AG. Approximately 40 µL of solution were applied on a freshly cleaved graphite sample. A rimmed sample holder was used in order to avoid concentration changes caused by spilling. Images were acquired directly at the liquid-solid interface with a mechanically cut Pt/Ir (90/10) tip immersed into the liquid.

The sublimation enthalpy was determined by using a home-built Knudsen cell with an integrated Quartz Crystal Microbalance (QCMB) (1.4 cm crystal diameter and 6 MHz nominal eigenfrequency). [86] The shift of resonant frequency (Δf) which is proportional to the effusion rate was measured vs. time for different crucible temperatures. For all temperatures, the slope in Δf vs. t curves is constant, indicating the validity of the chosen approach. [86]

The enthalpy of dissolution was determined from temperature dependent measurements of SDA solubility in 9A by means of UV-vis absorption spectroscopy (USB4000 Miniature Fiber Optic Spectrometer from Ocean Optics with an ISS-UV/VIS light source, and a Hellman 100-QS quartz glass cuvette; 10 mm optical path length). To this end, the cuvette was heated with two sideways mounted Peltier elements and the temperature was measured with a thermocouple in the cuvette and kept constant with a temperature controller (Eurotherm 2416). Spectra of pure 9A solvent at the respective temperatures were used as reference. According to Lambert-Beer’s law, the absorbance of saturated solutions is proportional to the solubility. UV-vis absorption spectra of SDA exhibit three clear absorption bands centered at 320 nm, 335 nm, and 350 nm due to n-π^* and π-π^* transitions as expected for aromatic compounds with double bonds. Since there is no interference with absorption of the 9A solvent in this spectral range, temperature dependent UV-vis absorption spectroscopy is an appropriate method to quantify the enthalpy of dissolution.

TPD experiments were performed in ultra-high vacuum. Monolayers were first deposited onto a graphite surface by thermal sublimation, and subsequently desorbed by linearly ramping the substrate temperature in time. Simultaneously, SDA desorption rates were recorded by a quadrupole mass-spectrometer positioned close to the graphite surface and set to a mass of 179 amu. Eight sets of experiments were performed with different heating rates ranging from 0.48 K s^{-1} to 0.84 K s^{-1}. The complete analysis method was used to calculate the enthalpy of desorption, since no a priori assumptions neither on the desorption order nor on the underlying desorption mechanism are required.[164]

5.3.2 Computational

Theoretical enthalpy values were obtained by MM and MD calculations using the MM3 force field. [118-120] For molecules like SDA, the strength of hydrogen bonds is significantly enhanced by resonance assisted hydrogen bonding (RAHB) due to delocalisation of the electron density across the π-system of the C=O in carboxylic groups.[142, 143] The MM3 force field was modified accordingly to obtain accurate enthalpy values for hydrogen bonds: hydrogen-bond parameters $\varepsilon_{H\cdots O}$ = 33.4 kJ mol^{-1} and $R_{H\cdots O}$ = 2.05 Å reproduce the density-functional theory (B3LYP functional, 6-31G(d) basis set, counterpoise-corrected) values of the hydrogen bond energy of the carboxylic acid dimer (-66.9 kJ mol^{-1} for TPA as model system) and the TPA-TPA distance in the dimer (9.64 Å).

The theoretical binding enthalpy of SDA in bulk crystals was calculated in two steps. Firstly, STM results were used as a starting point to optimise the theoretical lattice parameters A, B, and γ for the 2D lattice. Based on these values the lattice parameters C, α, and β were varied until the lowest-energy 3D structure of SDA was obtained.

Adsorption energies were calculated for an SDA molecule on a large (800 C atoms) hydrogen-terminated graphene sheet, for a regular grid of the molecule's positions and azimuthal orientations.

5.4 Results and discussion

5.4.1 Monolayer structure

At the nonanoic acid – graphite interface SDA self-assembles into long-range ordered monolayers with low defect density and large domain size, an overview STM image is depicted in Fig. 5.1(a). Owing to the high stability of the monolayer, submolecular details can routinely be resolved by STM, a representative image is shown in Fig. 5.1(b). The structure contains one molecule per unit cell. Precise lattice parameters of $A = (16.1 \pm 0.1)$ Å, $B = (7.5 \pm 0.1)$ Å, $\gamma = 52° \pm 1°$ and the corresponding superstructure matrix were obtained from split images (cf. section 5.5). The experimental lattice parameters and the orientation to the graphite substrate are perfectly reproduced by a commensurate $\begin{pmatrix} 6 & 1 \\ 0 & 3 \end{pmatrix}$ superstructure, corresponding to $A = 16.13$ Å, $B = 7.38$ Å, $\gamma = 52.4°$. Commensurability of the SDA monolayer is in accord with the absence of a Moiré pattern, i.e. a large scale STM contrast modulation due to inequivalent adsorption sites, as typically observed for incommensurate superstructures on graphite. [191, 192] From the STM contrast single SDA molecules can be unambiguously identified. As indicated by the overlay to Fig. 5.1(b), SDA molecules are interconnected into 1D chains by twofold cyclic hydrogen bonds between their carboxylic groups. The 2D monolayer structure is comprised of a densely packed arrangement of 1D hydrogen bonded chains, most likely stabilized by weaker interchain C-H···O hydrogen bonds. This precise assessment of the monolayer structure facilitates a detailed comparison with the geometry optimized structure from MM calculations (vide infra).

5.4.2 Born-Haber cycle

To obtain a precise value of the total enthalpy change of SDA monolayer self-assembly, we propose an adapted Born-Haber cycle as introduced in chapter 4 using the dicarboxylic acid terephthalic acid (TPA) as a model system. The basic idea is to combine sublimation enthalpy, dissolution enthalpy, and the binding enthalpy of SDA in the monolayer to derive a precise value for the enthalpy difference between molecules dissolved in solution and incorporated into the monolayer. Additional contributions from the solvent are taken into account by a dewetting enthalpy. Enthalpy differences between crystal and vacuum, monolayer and vacuum, crystal and solution are measured by the experimental techniques described in the experimental section, the results are presented in the following.

5.4.3 Binding enthalpy of monolayer on graphite with respect to vacuum

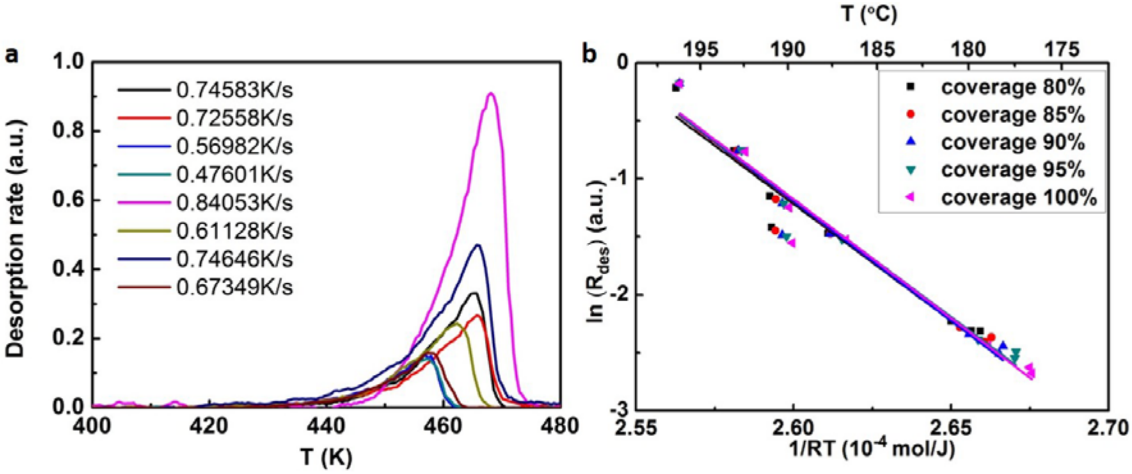

Figure 5.2. Temperature Programmed Desorption of SDA from graphite: (a) desorption rate vs. surface temperature for different heating rates; (b) Corresponding plots at different monolayer coverages obtained from a complete analysis. The enthalpy of desorption derived from linear fitting of the obtained plots amounts to +(203.8±9.1) kJ mol^{-1}.

The binding enthalpy of SDA in the monolayer on graphite with respect to isolated molecules in vacuum $\Delta H_{monolayer \rightarrow vacuum}$ was determined by temperature programmed desorption (TPD) experiments. Samples with monolayer coverage were prepared by sublimation of SDA from a Knudsen cell onto graphite with a crucible temperature of 190 °C and a deposition time of ~20 min. TPD experiments were carried out by heating with a linear temperature ramp, applying different heating rates. Individual desorption spectra are depicted in Fig. 5.2a. The experiments were evaluated with the complete analysis method, the corresponding results are shown in Fig. 5.2b and yield a monolayer binding enthalpy of -(203.8±9.1) kJ mol^{-1}. This energy includes both SDA-SDA interactions in the monolayer and SDA adsorption energy on graphite.

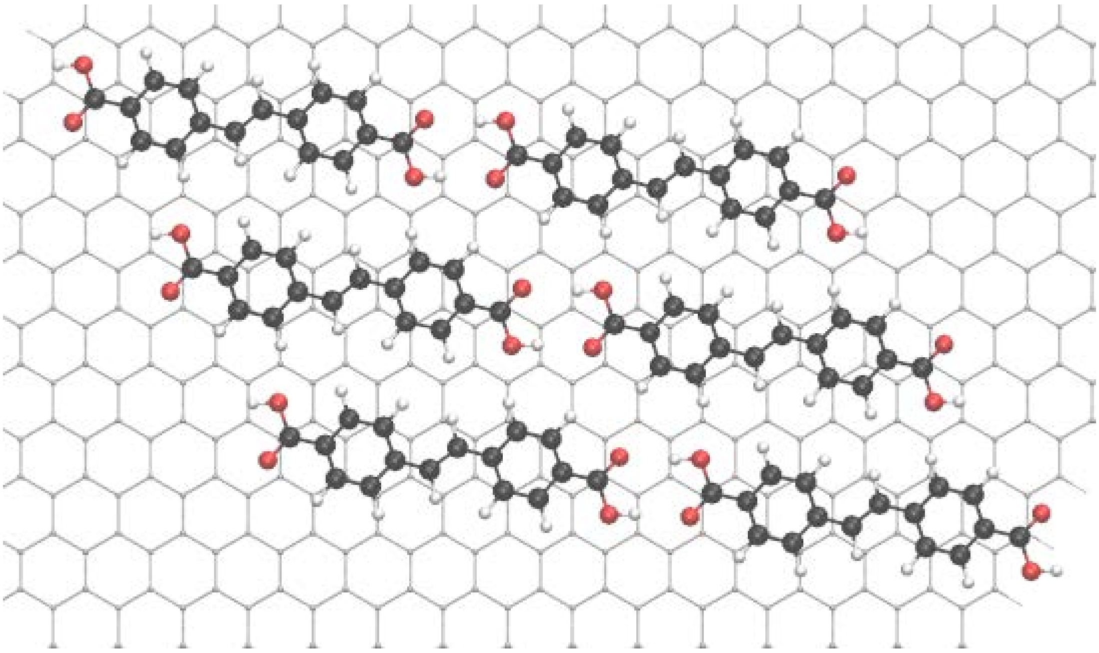

Figure 5.3. Model of the lowest energy SDA monolayer structure based on the experimental commensurate superstructure. (black: carbon, red: bromine, white: hydrogen)

The monolayer binding energy was also theoretically assessed by MM calculations with a modified MM3 force field as described in the computational section. These MM calculations also allow for a partition of the total binding energy into molecule-molecule and molecule-substrate interactions, thereby providing deeper insights into the relative strengths and interplay of these interactions. To evaluate substrate influences on the monolayer structure, first a free standing SDA monolayer comprised of densely packed hydrogen bonded chains was optimized, resulting in a SDA binding energy of -82.7 kJ mol^{-1}. The corresponding lattice parameters of A = 16.00 Å, B = 8.15 Å, γ = 49.7° are already close to those of the experimental commensurate superstructure (16.1 Å, 7.38 Å, 52.4°). Consequently, the lattice parameters of the free-standing SDA monolayer which are controlled only by molecule-molecule interactions can be maintained upon adsorption on graphite with only slight adjustments. Hence, the SDA monolayer can easily realize the energetic advantage of a commensurate superstructure on the graphite surface, where each molecule can occupy its preferred adsorption site. Additional MM calculations showed that constraining the SDA lattice to the experimental values of the commensurate superstructure reduces the binding energy to -73.0 kJ mol^{-1}, i.e. causes an energy penalty of +9.7 kJ mol^{-1}.

The molecule-substrate interaction was evaluated by optimizing a single SDA molecule on graphite. Different sites within the graphite unit cell and azimuthal orientations were probed on a regular grid. The geometry of SDA permits similar adsorption sites for both phenyl rings on graphite, and the highest and lowest binding energy configurations correspond to AB (highest binding) and AA (lowest binding) stacking with corresponding adsorption energy values of -116.4 kJ mol^{-1} and -115.2 kJ mol^{-1}, respectively. The energy difference between the most favourable and least favourable adsorption site may be somewhat underestimated in these calculations: for comparison, the diffusion barrier for benzene on graphite calculated with MM3 is 0.004 eV, [16] while this property was experimentally measured to be 0.017+0.012 eV. [193] The value of the energy minimum is likely to be more reliable than the energy barrier.

However, the commensurate superstructure corresponds to a different orientation of SDA on graphite (Fig. 5.3), where the phenyl rings are not ideally stacked on graphite. In the actual orientation the adsorption energy is still large, but the range between maximum and minimum is smaller (only between -116.0 and -115.8 kJ mol^{-1}). The calculated total binding energy of SDA in a monolayer on graphite is obtained as the sum of molecule-molecule and molecule-substrate interactions (in the adsorption configuration that corresponds to the experimental commensurate structure, Fig. 5.3) and amounts to -189.0 kJ mol^{-1}, in quantitative agreement with the TPD experiment.

5.4.4 Sublimation enthalpy

The sublimation enthalpy $\Delta H_{crystal \rightarrow vacuum}$ is derived from temperature dependent measurements of the effusion rate in high vacuum by means of a Quartz Crystal Microbalance (QCMB).[86] The shift of resonant frequency Δf vs. time t is depicted in Fig. 5.4a for nine different crucible temperatures in a range from 125 °C to 165 °C. The slope corresponds to the effusion rate, which is constant for a given crucible temperature. The effusion rate is proportional to the saturated vapour pressure of SDA at the respective crucible temperature, accordingly $\Delta H_{crystal \rightarrow vacuum}$ can be derived from the slope in a Van’t Hoff plot. As shown in Fig. 5.4b the corresponding Van’t Hoff plot is perfectly linear, resulting in a value of $\Delta H_{crystal \rightarrow vacuum} = +(169.0 \pm 2.8)$ kJ mol^{-1}.

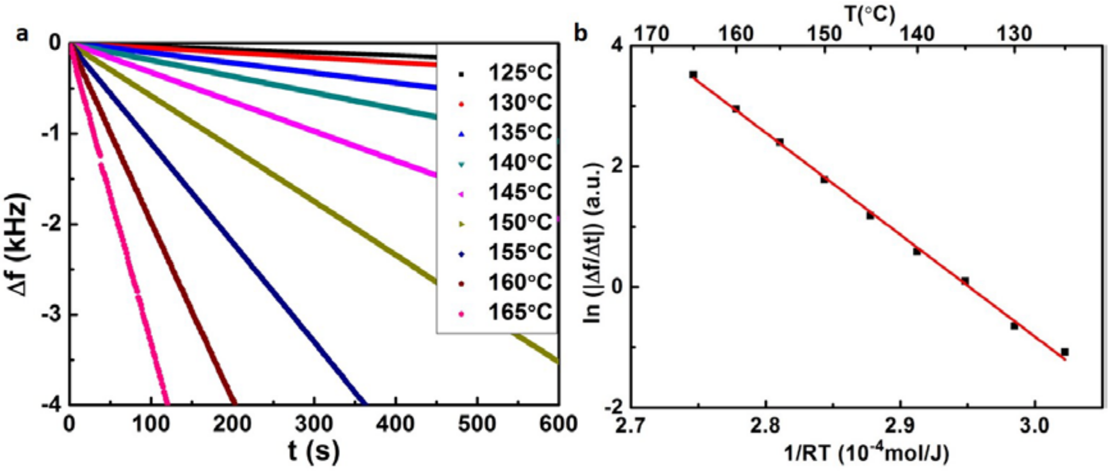

Figure 5.4. Measurement of the SDA effusion rate from a Knudsen-cell by a Quartz Crystal Microbalance: (a) resonant frequency shift Δf vs. time t traces for crucible temperatures from 125 °C up to 165 °C; (b) Corresponding Van't Hoff plot; each dataset in (a) is represented by one data point. From the slope a sublimation enthalpy of +(169.0±2.8) kJ mol^{-1} is deduced.

For a theoretical evaluation of $\Delta H_{crystal \rightarrow vacuum}$ the crystal structure is required. An experimentally determined crystal structure is unfortunately not available for SDA. However, by analogy with crystal structures from other carboxylic acids, [194, 195] it can be safely assumed that both carboxylic groups of SDA take part in two-fold cyclic hydrogen bonds, and SDA molecules, most likely, form 2D layers. To evaluate the contribution of these hydrogen bonds, MM calculations of 1D hydrogen bonded SDA chains were performed, resulting in a binding energy of -67.0 kJ mol^{-1}. To obtain a theoretical estimate of $\Delta \mathrm{H}_{\mathrm{crystal} \rightarrow \mathrm{vacuum}}$ a hypothetic SDA crystal structure was constructed as a stacked arrangement of 2D monolayers. MM geometry optimization results in a triclinic structure with one molecule per unit cell and lattice parameters of A = 16.0 Å, B = 7.9 Å, C = 4.3 Å, α = 132°, β = 73°, γ = 131°. The full geometry optimization of the bulk structure has not affected the intrachain spacing of SDA within the hydrogen bonded chains, but resulted in a slight change of the interchain spacing as compared to a pure 2D structure. The binding enthalpy of SDA in this hypothetic structure of -178.0 kJ mol^{-1} is nevertheless in excellent agreement with the experimental value. Comparison of the total binding energy with that of the 1D chain, i.e. the contribution from the intermolecular hydrogen bonds, reveals a contribution of ~100 kJ mol^{-1} of additional intermolecular interactions, as the weak interchain hydrogen bonds and van der Waals interactions both within and between 2D layers of SDA. Interestingly, for the large SDA molecule the strength of van der Waals forces in the 3D structure already exceeds the strong two-fold hydrogen bonds.

5.4.5 Dissolution enthalpy

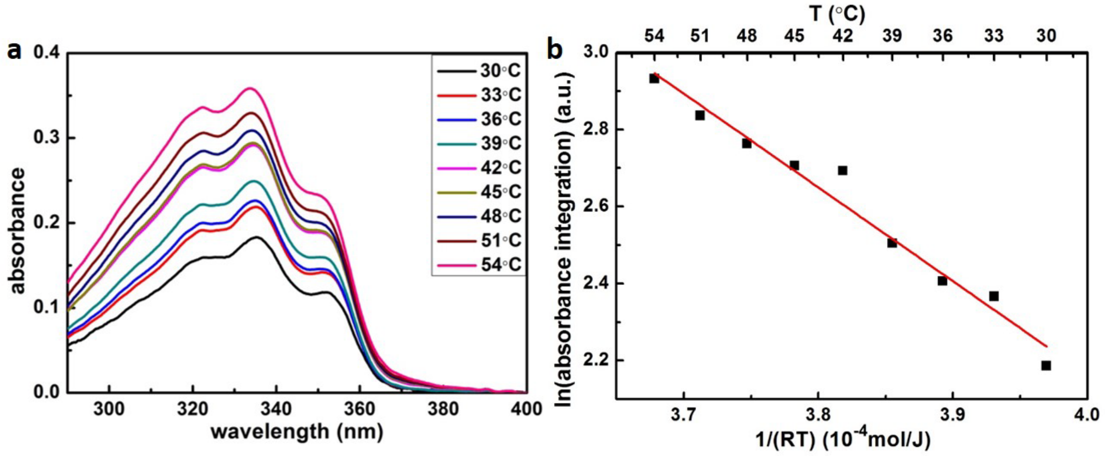

Figure 5.5. SDA solubility measurements in 9A as a function of temperature: (a) UV-vis absorption spectra of saturated SDA in 9A solutions obtained at different temperatures; (b) Corresponding Van't Hoff plot; the integral absorbance for each temperature was obtained from the spectra in (a) by integration between λ=290nm-400nm. The derived enthalpy of dissolution is +(24.4±1.5) kJ mol^{-1}.

The enthalpy of dissolution $\Delta H_{crystal \rightarrow sol}$ was derived from measurements of SDA solubility in 9A as a function of temperature in the range 30 °C to 54 °C by UV-vis absorption spectroscopy. Single UV-vis absorption spectra of saturated solutions for different temperatures are depicted in Fig. 5.5(a). The absorbance increases with increasing temperature, indicating an endothermic process. For the corresponding Van't Hoff plot in Fig. 5.5(b) the spectra were integrated between λ = 290nm-400nm, and the slope corresponds to an endothermic dissolution enthalpy of +(24.4±1.5) kJ mol^{-1}. For comparison, the binding energy of a two-fold cyclic hydrogen bonded carboxylic acid dimer is in the range of -67.8 kJ mol^{-1}, as determined from IR absorption spectra of benzoic acid.[143] Since the experimental dissolution enthalpy is smaller than the binding enthalpy of two-fold carboxylic acid groups, we conclude that solvated SDA molecules bind to two 9A solvent molecules by two-fold hydrogen bonds. As outlined in section 5. 2 (cf. section 4.5), the computational cost of a theoretical solvation enthalpy determination by MD is relatively high, while the error bars are quite large, we thus use the experimental value for the Born-Haber cycle.

5.4.6 Dewetting Enthalpy

Larger fatty acids are solvents with a high affinity to graphite. Accordingly, the formation of stable ordered solvent monolayers can be observed and has to be considered in the overall enthalpy balance. The 9A monolayer structure consists of an interdigitated dense packing of hydrogen bonded dimers.[166] Consequently, self-assembly of a solute monolayer requires prior desorption of this stably adsorbed solvent monolayer. The associated enthalpy cost of dewetting is very difficult to assess: on the experimental side, because it cannot directly be measured; on the theoretical side because the required system size renders a thorough calculation computationally very challenging, and their results not easily tractable. Albeit it is known that 9A forms quasi-static ordered monolayers on graphite,[16] additional complications arise due to the fact that the precise thickness of the interfacial solvent layer, i.e. contributions from second and third layers, and its precise structure are not known.

Both the initial ordered 9A solvent and the subsequently self-assembled SDA solute monolayers are in direct contact with the supernatant liquid 9A. Stable adsorption of a second 9A monolayer on top of a 9A or SDA monolayer has never been observed by STM measurements. The particularly strong interaction between alkane tails and graphite is indispensable for the stabilization of 9A monolayers. Consequently, neither the ordered 9A nor the SDA monolayer provides a suitable template for stable adsorption of a second 9A layer. In order to estimate the dewetting enthalpy, it is assumed that the interaction energy per unit area of the respective monolayers with liquid 9A, i.e. the interface tensions, are comparable within the experimental error of this approach, and the structures of the second, third and further solvent layers are approximately similar both above SDA and above 9A monolayers. Therefore, when comparing SDA and 9A interfacial monolayers, the energies of these near-interface layers would cancel out. Accordingly, for dewetting only the first 9A monolayer needs to be taken into account.

Based on this simplifying assumption, the enthalpy contribution from desorption of the first 9A monolayer into the liquid is evaluated from two contributions: (i) the enthalpy difference between 9A on graphite and in vacuum, and (ii) the evaporation enthalpy, i.e. the enthalpy difference between 9A in vacuum and liquid. According to MM simulations the desorption enthalpy of 9A from graphite into vacuum amounts to $\Delta H(9A)_{graphite \rightarrow vacuum} = +107.5\ \mathrm{kJ\ mol^{-1}}$, [16] in good agreement with TPD experiments. [86] The evaporation enthalpy amounts to $\Delta H(9A)_{liquid \rightarrow vacuum} = +82.4\ \mathrm{kJ\ mol^{-1}}$. [196] Consequently, the enthalpy difference between adsorbed and liquid 9A corresponds to $\Delta H(9A)_{graphite \rightarrow liquid} = +25.1\ \mathrm{kJ\ mol^{-1}}$. Yet, desorption of the first 9A monolayer is also associated with a favourable entropic contribution to the total free energy. A reasonable estimate can be obtained from the entropy of melting, i.e. the transition from crystalline to liquid 9A. Since 9A molecules are fully immobilized and constrained to a specific orientation and conformation both in the crystal and in the monolayer, the entropies of 9A are comparable within the accuracy of this approach. The entropy of melting corresponds to +69.4 J mol^{-1} K^{-1}, [85] consequently, for dewetting a 9A monolayer, the entropic contribution to the free energy $-T\Delta S$ at room temperature corresponds to -20.7 kJ mol^{-1}. Accordingly, ΔG for formation of an ordered 9A monolayer at the liquid-graphite interface is only -4.4 kJ mol^{-1}, or, in other words, the 9A monolayer is thermodynamically not very stable. This provides evidence that only the first monolayer of solvent on graphite is stable, because the enthalpic stabilization in a second layer would be inferior and would not be able to compensate the entropy cost of trapping 9A into a quasi-static structure.

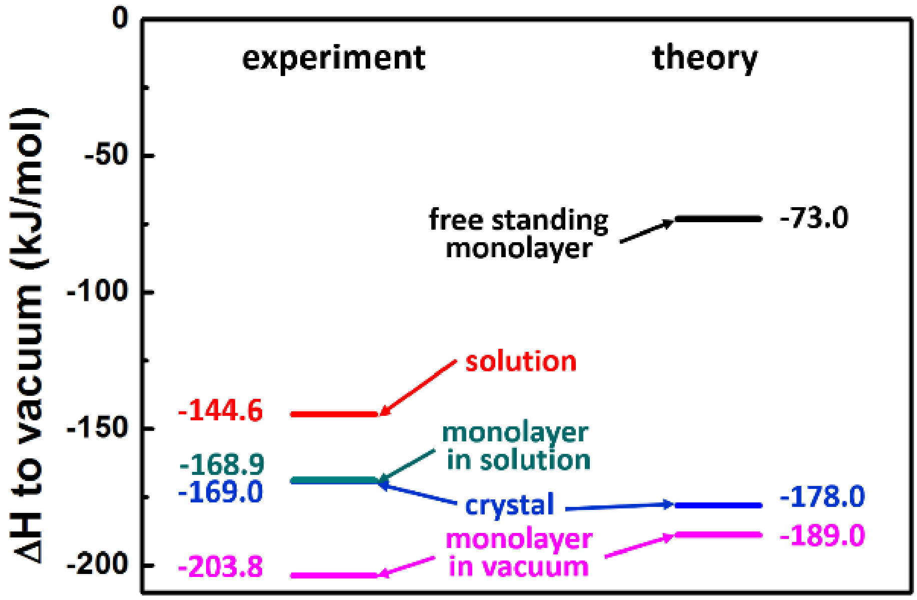

Figure 5.6. Results for the Born-Haber cycle for SDA with respect to vacuum, i.e. with respect to free single molecule: left side represents the experimental results; right side represents the theoretical results.

In order to use the dewetting enthalpy for the Born-Haber cycle, a renormalization to the number of SDA molecules becomes necessary. The renormalization factor is obtained from the area per molecule ratio of SDA and 9A, respectively. The 9A monolayer structure on graphite is known from both X-ray and neutron diffraction, resulting in an area per 9A molecule of 67.9 Å². [166] Based on the commensurate superstructure, the area per SDA molecule amounts to 94.3 Å². Accordingly, the dewetting enthalpy ΔH_{dewet} of 9A per SDA molecule corresponds to +34.9 kJ mol^{-1}.

5.4.7 Total binding energy and entropy

All individual enthalpy values are summarized in Fig. 5.6. Combination according to the scheme depicted in Fig. 5.1 results in a value for the total enthalpy change of -24.3 kJ mol^{-1} for SDA monolayer self-assembly on graphite from 9A solution.

To understand the thermodynamics of self-assembly it is also instructive to contrast the enthalpy gain with the entropy cost. The entropy of immobilizing molecules from solution depends on the concentration and increases with increasing dilution. Accordingly, a critical concentration exists, below which monolayer self-assembly becomes thermodynamically unfavorable. This critical concentration can be determined experimentally in a dilution series and for SDA monolayer self-assembly from 9A a value of (4.1 ± 0.3) µmol L^{-1} was found. The amount of SDA in solution at the critical concentration still exceeds the number of SDA molecules required for monolayer coverage by approximately a factor of 4. At the critical concentration $\Delta G = 0$, accordingly $T\Delta S = \Delta H$ and a direct comparison between enthalpy and entropy becomes feasible.

To evaluate the entropic cost of self-assembly, a partition scheme is used similarly to our previous study on TPA (cf. section 4.4). [16] First, contributions from rotational and translational entropy are considered and estimated by approaches from statistical mechanics as proposed by Whitesides and coworkers (cf. section 2.5). [129] For the translational entropy the Sackur-Tetrode equation is used. Since it was originally conceived for the gas phase, the solvent is taken into account by referring the concentration to the free volume of the solvent. The results are summarized in Table 5.1, details of the entropy calculation are given in section 2.5.

	$-T\Delta S_{trans}$	$-T\Delta S_{rot}$	$-T\Delta S_{tot}$
SDA	+67.4	+41.3	+108.7
9A-SDA-9A	+70.3	+49.4	+119.7
9A-9A	+34.7	+43.8	+78.5

Table 5.1. Contributions of rotational and translational entropy to the free energy for unsolvated SDA molecules, 9A dimers, and hydrogen bonded complexes of SDA and two 9A solvent molecules at 298 K. All in kJ mol^{-1}

Similar to previously studied TPA, $-T\Delta S$ i.e. the entropy contribution to ΔG associated with adsorption of a single unsolvated SDA molecule of +108.7 kJ mol^{-1} notably exceeds the enthalpy gain. However, as also indicated by the relatively small dissolution enthalpy, SDA molecules are solvated by 9A molecules in solution. Accordingly, a plausible model for SDA adsorption from 9A is the release of SDA from 9A-SDA-9A complex and subsequent formation of a hydrogen bonded 9A-9A dimer. This desolvation has profound consequences for the entropy balance, since both translational and rotational entropy of the 9A-SDA-9A complex are fully lost, whereas translational and rotational entropy of the 9A-9A dimer are regained, resulting in a reduced entropy cost of +41.2 kJ mol^{-1} (cf. section 4.4). The total entropy contribution to free energy of +12.5 kJ mol^{-1} is obtained by adding the entropy cost of SDA adsorption to the entropy gain of dewetting (-28.7 kJ mol^{-1}, normalized to the number of SDA molecules), in good quantitative agreement with the total enthalpy gain of -24.3 kJ mol^{-1}.

5.5 Supporting information

STM Split image.

Precise lattice parameters of SDA monolayers were obtained from several so called split-images where within the same frame both the adsorbate structure and the graphite lattice were imaged, an example is depicted in Fig. 5.8. Based on the adsorbate lattice parameters and the orientation of the unit cell with respect to the graphite lattice, the closest commensurate superstructure corresponds to the following matrix (referring to the graphite lattice):

$$\begin{pmatrix} 6 & 1 \\ 0 & 3 \end{pmatrix}$$

The match between experimental lattice parameters from STM images (A = (16.1±0.1) Å, B = (7.5±0.1) Å, γ = 52°±1°) and those of the postulated commensurate lattice (A = 16.13 Å, B= 7.38 Å, γ = 52.4°) is excellent.

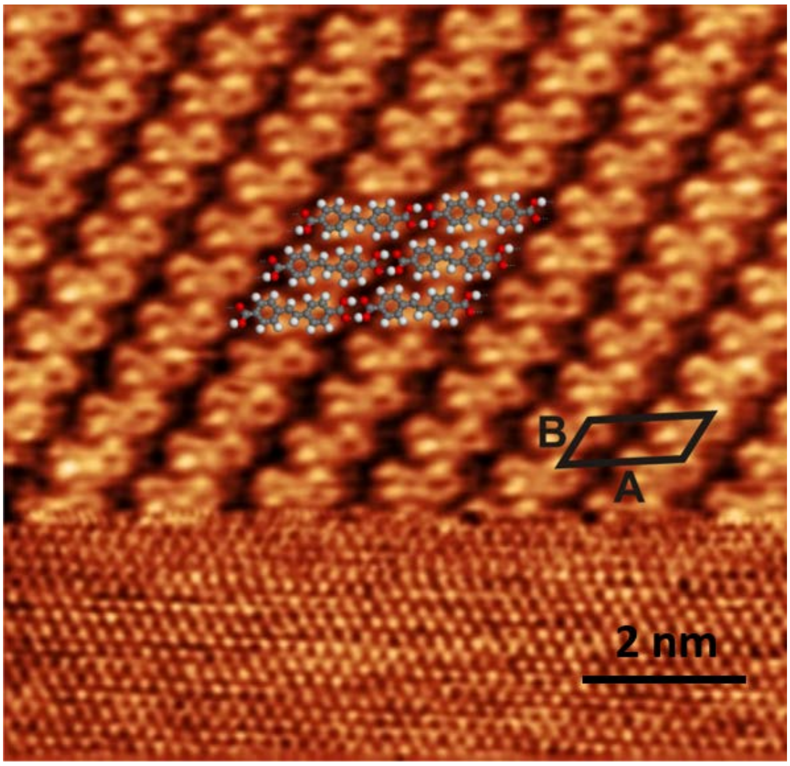

Figure 5.7. STM split-image of a SDA monolayer at the nonanoic acid-graphite interface. In the lower part the graphite substrate was imaged with atomic resolution by decreasing the tunneling gap. Calibration with this internal standard yields precise lattice parameters for the SDA monolayer of A = (16.1 ± 0.1) Å, B = (7.5 ±0.1) Å, γ=52° ± 1°. The overlay indicates the arrangement of SDA molecules and the black lines mark the unit cell. (Image size 16.2×15.6 nm², I = 50 pA, V_{sample} = -300.0 mV for SDA; I = 200 pA, V_{sample}= -1.53 mV for graphite)

5.6 Conclusion and Summary

A previously proposed adapted Born-Haber cycle was employed to assess the total enthalpy change of self-assembly of SDA monolayers on graphite from 9A solution. A direct comparison between experimental and theoretical values of the binding energies in the monolayer again demonstrated the suitability of MM calculations with suitably parameterised force fields for carboxylic acids on graphite. In addition, the theoretical and experimental sublimation enthalpies came out similar, even though the actual SDA crystal structure was not available. This suggests that the theoretically predicted SDA crystal structure closely corresponds to the real SDA crystal structure; an alternative explanation for this agreement in sublimation enthalpies is that the van der Waals contribution is not very sensitive to the exact arrangement of SDA molecules, as long as the packing densities are comparable.

The overall enthalpy change of SDA monolayer self-assembly as deduced from the Born-Haber cycle of -24.3 kJ mol^{-1} slightly exceeds the entropic cost of +12.5 kJ mol^{-1} at the critical concentration. Besides the summation of experimental errors, neglect of conformational entropy and inaccuracies of the rather simple free volume approximation can be possible key factors for uncertainties in the entropic contribution. On the other hand, inaccuracies in the enthalpy assessment, especially in the rather crude model of the dewetting enthalpy may also account for the overall relatively small deviation.

Since the original motivation of this study was to reveal the influence of the extended aromatic system of SDA on the thermodynamical stability of the monolayer, it is instructive to compare the Gibbs free energy of SDA monolayer self-assembly to previously studied TPA, i.e. the influence of the extra phenyl ring on total enthalpy and entropy change. The sublimation enthalpy of TPA is +127.2 kJ mol^{-1}, i.e. about ~42 kJ mol^{-1} smaller than that of SDA. Yet, the binding energy of TPA molecules in the adsorbed (unsolvated) monolayer is -140 kJ mol^{-1}, i.e. already ~64 kJ mol^{-1} weaker than that of SDA. From this direct comparison it can be concluded that the second phenyl ring of SDA increases this molecule’s binding energy on graphite almost 50 % more than the binding energy in the crystal. In other words, the extended aromatic system of SDA leads to a significant increase of the adsorbed monolayer binding energy.

The second important factor that determines the solution-monolayer equilibrium is the energy of the solute in solution. The dissolution enthalpy of TPA in 9A is +12.8 kJ mol^{-1}, whereas that of SDA is almost twice as large. Since in both cases the dissolution enthalpy is positive, i.e. dissolution is endothermic, a high value for SDA means that this molecule in solution is less stable, and crystallization (or monolayer formation) of SDA from solution is more favourable than in the case of TPA. This additionally enhances the enthalpic stabilization of the interfacial SDA monolayer.

For the overall entropy change differences between TPA and SDA are less pronounced: $-T\Delta S_{tot}$ amounts to +12.3 kJ mol^{-1} for TPA [16] as compared to +12.5 kJ mol^{-1} for SDA. Interestingly, the overall entropy change is almost equal to TPA. This is because the regain of entropy caused by 9A dewetting strongly corresponds to the molecular size. Therefore, the elimination to SDA entropy change is significantly higher. The summation of experimental errors, neglect of conformational entropy and inaccuracies originate in the simplification of the free volume calculations and inaccuracy of the dewetting enthalpy assessments are the possible reasons caused the difference between the total enthalpy and entropy contributions of SDA self-assembly. Both the enthalpic aspects – the stronger adsorption on graphite and the more endothermic dissolution of SDA – and the scaling behavior of the entropy cost contribute to the comparatively high thermodynamic stability of SDA monolayers, as experimentally expressed in a low critical concentration required for SDA monolayer formation ((4.1 ± 0.3) µmol L^{-1}, i.e. more than an order of magnitude lower than for TPA (120 ± 15) µmol L^{-1}).

Chapter 6: Thermodynamics of halogen bonded monolayer self-assembly at the liquid–solid interface

Wentao Song, Natalia Martsinovich, Wolfgang M. Heckl, and Markus Lackinger, Thermodynamics of halogen bonded monolayer self-assembly at the liquid-solid interface. Chem. Commun., 2014, http://dx.doi.org/10.1039/C4CC06251E. Reproduced and adapted by permission from the Royal Society of Chemistry.

6.1 Abstract

Monolayer self-assembly of a hexabrominated, three-fold symmetric aromatic molecule is studied at the heptanoic acid–graphite interface. Thermodynamical insights are obtained from an adapted Born–Haber cycle that is utilized to derive the overall enthalpy change including solvent effects. Comparison with theoretical entropy estimates suggests a minor influence of solvation.

6.2 Introduction

Halogen bonds have gained attention in crystal engineering, supramolecular self-assembly, and even computer aided drug design. [3, 197-199] Halogen bonds are viewed as a separate class of donor–acceptor type interactions that originate in the anisotropic charge distribution around halogen substituents, most importantly Br and I. The so called σ-hole gives rise to a positive electrophilic cap at the opposing pole of the σ-bond that is balanced by a nucleophilic equatorial ring of negative charge. [200-202] A halogen bond is formed through a net attraction between the electrophilic cap of the halogen with either the nucleophilic part of a different entity, as for instance the nitrogen electron lone pair, or the nucleophilic ring of another halogen. This characteristics results in directionality and selectivity, whereas the halogen bond strength decreases as the halogen electronegativity increases. Moreover, a single halogen substituent can simultaneously act as both halogen bond acceptor and donor – an important distinction from the in other aspects quite comparable hydrogen bonds. A triangular arrangement of three halogen atoms with three cyclic halogen bonds is a frequently encountered motif both in bulk crystals and on surfaces,[150, 151] but alternative configurations were similarly reported.[38]

Supramolecular self-assembly of halogen bonded systems on surfaces was recently studied by scanning tunneling microscopy (STM) both under ultra-high vacuum [39, 150, 203] and ambient conditions. [38, 204-206] Accompanying density functional theory simulations based on experimental structures provided insights into the energetics. [38-40] While this is an important first step, a fundamental understanding of self-assembly from solution requires a full thermodynamical assessment, including the role of the solvent. As a model system hexabromotriphenylene (HBTP, cf. Fig. 6.1) is studied at the heptanoic acid (7A)–graphite interface with the aim to quantify all relevant contributions to ΔG. At the liquid–solid interface, the adsorption energy becomes significantly lowered as compared to vacuum by the supernatant liquid phase. This important solvent influence is quantified for the proposed model system by applying an adapted Born–Haber cycle derived from sublimation, dissolution, and monolayer binding enthalpy in vacuum.[16]

6.3 Results and discussion

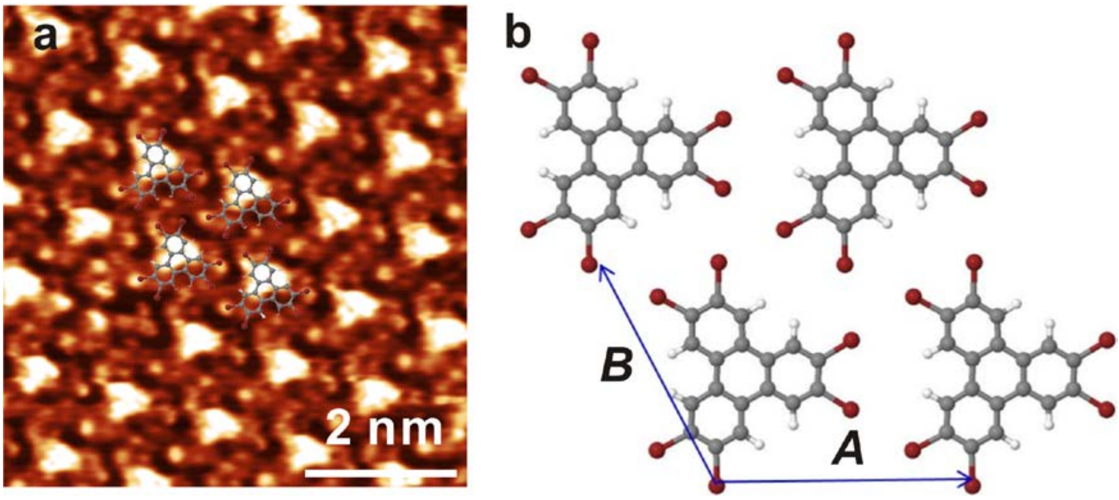

Figure. 6.1. (a) High resolution STM image of a HBTP monolayer at the 7A-graphite interface. V_{sample} = -0.40 V, I = 80 pA, (b) DFT optimized geometry of a free standing HBTP monolayer (grey: carbon, red: bromine, white: hydrogen)

At the 7A–graphite interface HBTP self-assembles into a densely packed structure, a high resolution STM image is presented in Fig. 6.1a. The lattices of HBTP and graphite are aligned (cf. section 6.4) and the experimental lattice parameters of $A = B = (12.5\pm0.2)$ Å, $\gamma = 59°\pm2°$ match well with a 5×5 graphite superstructure. Moreover, the absence of a Moiré pattern in these images with pronounced submolecular contrast strongly indicates commensurability. To obtain a detailed structural model, dispersion-corrected DFT simulations of a free-standing HBTP monolayer constrained to a hexagonal lattice were carried out using both empirical dispersion correction (PBE+D) and a van der Waals functional (vdW-DF) (cf. section 6.6 for details). The optimized structure is shown in Fig. 6.1b. Simulations with unconstrained length of the lattice parameter yield an optimized value of 12.5 Å, i.e. only 1.5 % larger than 12.3 Å of the 5×5 graphite superstructure. The structure belongs to planar space group p31m, and all bromines take part in the prototypical triangular cyclic arrangement of halogen bonds with a Br-Br distance of 3.70 Å, in good agreement with literature. [151] Interestingly, the symmetry of high resolution STM images is significantly lower than that of the DFT structure and does not even reflect the three-fold symmetry of HBTP. This clearly indicates an adsorption site of HBTP with lower local symmetry. Nevertheless, in an overlay STM protrusions can be matched with bromine positions (cf. Fig. 6.1a). The vdW-DF derived monolayer binding energy per molecule with respect to vacuum of -48.3 kJ mol^{-1} is rather small. Compressing the structure to the experimental 5×5 graphite superstructure reduces the binding energy to -43.5 kJ mol^{-1}. A very similar binding energy was obtained using PBE+D: -45.5 kJ mol^{-1} for the unconstrained free-standing structure and -42.7 kJ mol^{-1} for the constrained 5×5 superstructure; VdW-DF was also employed to calculate the total binding energy comprised of molecule-molecule and molecule-surface interaction of HBTP in the adsorbed monolayer on graphite and results in ΔH_{mono}=-229.6 kJ mol^{-1} (cf. section 6.4). Similarly, these calculations yield an adsorption energy of HBTP on graphite of -186.1 kJ mol^{-1} per molecule, i.e. the molecule-surface interactions are approximately a factor of 4 larger than the intermolecular interactions.

In the actual experimental situation at the liquid-solid interface HBTP adsorbs from solution, whereby the effective enthalpy difference $\Delta H_{sol\rightarrow mono}$ is significantly lowered due to solvent interactions. Since a direct measurement is intricate, $\Delta H_{sol\rightarrow mono}$ is indirectly evaluated by combining ΔH_{mono} with experimentally determined sublimation ($\Delta H_{cryst\rightarrow vac}$) and dissolution enthalpy ($\Delta H_{cryst\rightarrow sol}$) as illustrated in Fig. 6.2.[16, 17, 86]

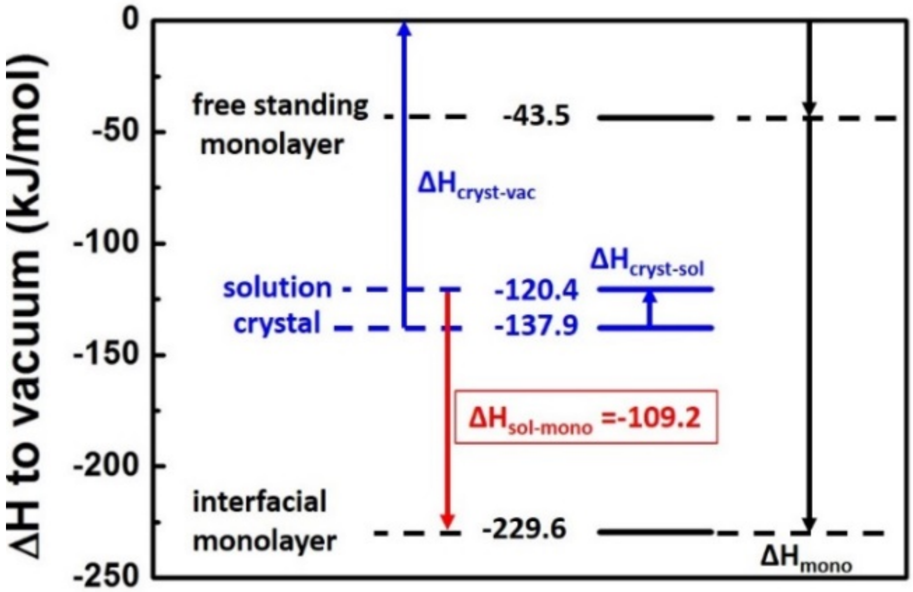

Figure. 6.2. Enthalpy diagram of the HBTP–7A–graphite system. Black and blue depicted values and arrows correspond to computational and experimental results, respectively. Vertical arrows denote the respective enthalpies.

$\Delta H_{cryst\rightarrow vac}$ was determined from the temperature dependence of the effusion rate from a Knudsen cell as measured with a Quartz Crystal Microbalance (cf. section 6.6 for details). [86] The eigenfrequency decline Δf vs. time t traces are shown in Fig. 6.3a for crucible temperatures between 225 °C and 270 °C. The rate $\Delta f/\Delta t$ is proportional to the vapour pressure at the respective temperature. The data yield a perfectly linear Van't Hoff plot with a slope corresponding to $\Delta H_{cryst\rightarrow vac} = +137.9\pm1.6$ kJ mol^{-1}.

$\Delta H_{cryst\rightarrow sol}$ was determined from the temperature dependence of the solubility as measured by UV-vis absorption spectroscopy of saturated solutions (cf. section 6.6 for details). Individual absorption spectra are shown in Fig. 6.3b for temperatures between 22 °C and 54 °C. The absorbance, hence the solubility, increases with temperature indicating endothermic dissolution. The total amount of dissolved HBTP molecules was estimated by integrating over the absorption band from λ = (270...340) nm. The data yield a perfectly linear Van't Hoff plot with a slope corresponding to $\Delta H_{cryst\rightarrow sol} = +17.5\pm0.6$ kJ mol^{-1}.

The theoretical (ΔH_{mono}) and both experimental ($\Delta H_{cryst\rightarrow vac}$ and $\Delta H_{cryst\rightarrow sol}$) enthalpies are compiled in Fig. 6.2 with isolated molecules in vacuum as a common reference state. From this $\Delta H_{sol\rightarrow mono}$ of -109.2 kJ mol^{-1} can be inferred. In principle, this enthalpy difference between solution and monolayer may be overestimated due to a possible contribution from dewetting. [16, 17] Self-assembly of a solute monolayer can require desorption of an initially assembled solvent monolayer, resulting in an enthalpy cost and an entropy gain for dewetting. However, an ordered quasi-static monolayer of 7A has never been observed at room temperature, suggesting that it is thermodynamically unstable ($\Delta G>0$). Based on the assumption that the differences in interfacial tension between 7A–graphite and 7A–HBTP monolayer are small in comparison to $\Delta H_{sol\rightarrow mono}$ contributions of solvent dewetting are not further considered, as they do not significantly affect ΔG.

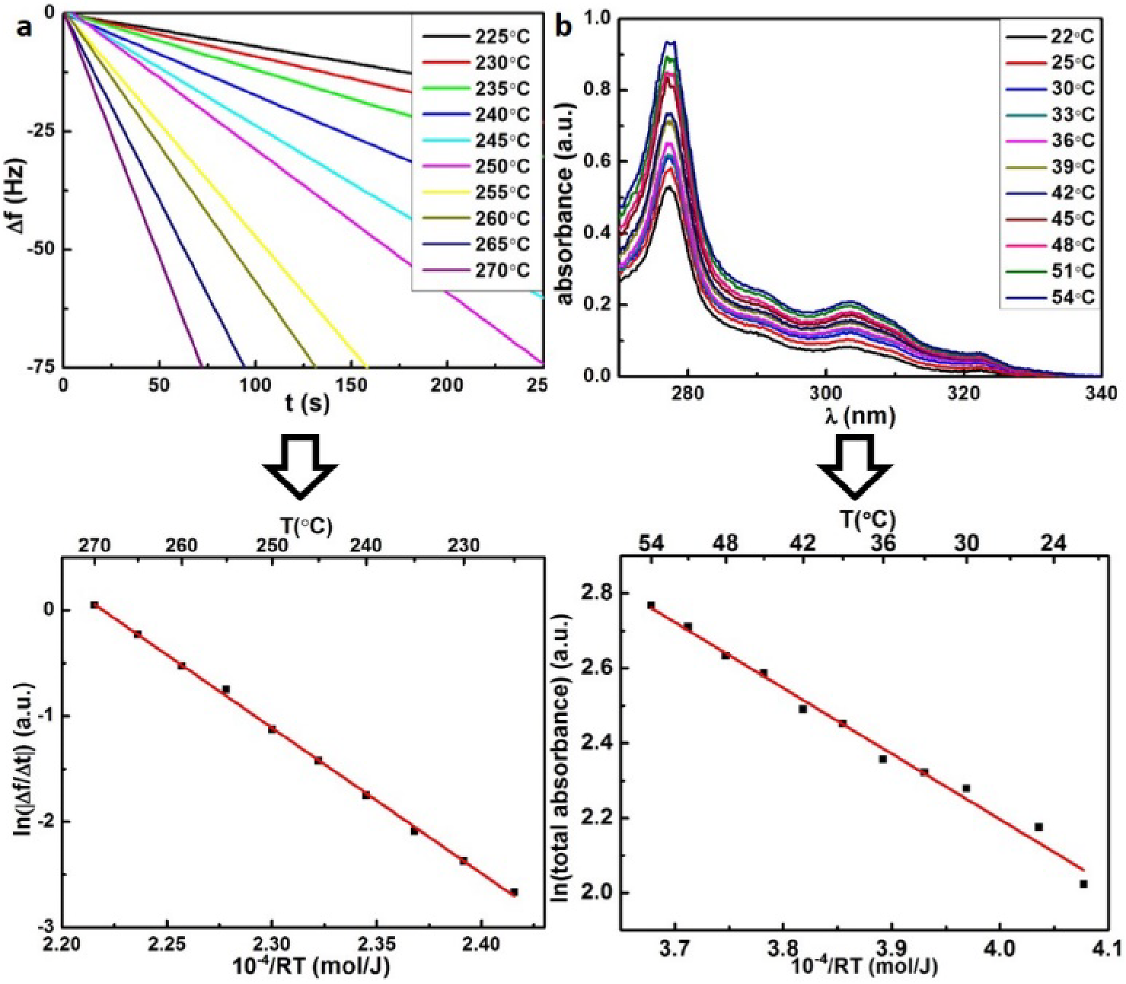

Figure. 6.3. Experimental determination of $\Delta H_{cryst\rightarrow vac}$ and $\Delta H_{cryst\rightarrow sol.}$(a) Δf vs. t traces for different crucible temperatures; (b) UV/Vis absorption spectra of saturated solutions for different solution temperatures; the lower panels depict the corresponding Van't Hoff plots; the slopes yield $\Delta H_{cryst\rightarrow vac}$ = (+137.9±1.6) kJ mol^{-1} and $\Delta H_{cryst\rightarrow sol}$ = (+17.5±0.6) kJ mol^{-1}.

For a complete thermodynamical understanding consideration of entropy contributions is inevitable. Since a direct measurement of ΔS is not possible, we propose an indirect evaluation via the critical concentration c_{crit}, i.e. the lowest solute concentration where self-assembled monolayers are still thermodynamically stable. Since ΔG becomes zero at c_{crit}, the overall entropy change can be determined from: $\Delta S=\Delta H/T$. For HBTP monolayers at the 7A–graphite interface dilution experiments result in c_{crit}= 28.8±3.7 µmol

L^{-1} (cf. section 6.6). Generally, ΔS has several contributions, yet for a rigid molecule such as HBTP translational (S_{trans}) and rotational (S_{rot}) entropy dominate. For molecules within the monolayer S_{rot} and S_{trans} are negligible as compared to the dissolved state, accordingly ΔS can be estimated as the total loss of S_{rot} and S_{trans}. Whitesides *et al.* propose to estimate S_{rot} with the rigid rotator model, and S_{trans} with the Sackur-Tetrode equation. [129] Since the latter was originally derived for gases, the solvent influence has to be implicitly taken into account, e.g. by free volume corrections. Table 6.1 summarizes S_{rot} and S_{trans} contributions evaluated according to this approach (cf. section 6.6 for details). Interestingly, the entropic contribution $-T\Delta S = +111.2$ kJ mol^{-1} is almost similar to the absolute value of $|\Delta H_{sol \rightarrow mono}| = 109.2$ kJ mol^{-1}. This perfect match implies that for HBTP self-assembly no further relevant thermodynamic contributions arise from desolvation. These results stand in vast contrast to interfacial monolayer self-assembly of 1, 4-benzenedicarboxylic acid and stilbene dicarboxylic acid likewise from fatty acid solution (cf. chapter 4 and chapter 5). [16, 17] In both cases $|\Delta H_{sol \rightarrow mono}|$ was significantly smaller than $-T\Delta S$ for the adsorption of unsolvated solute molecules. Therefore, it was only possible to explain spontaneous self-assembly by including a favourable entropy contribution from desolvation upon solute adsorption, whereby the released solvent molecules regain S_{trans} and S_{rot}. Dicarboxylic acid solute molecules strongly interact with fatty acid solvent molecules through two-fold hydrogen bonds. Accordingly, solute-solvent and solvent-solvent interactions are of comparable strength in these systems. Owing to the high strengths of carboxylic acid hydrogen bonds, formation of a quasi-static solvation shell can be anticipated for dicarboxylic acids dissolved in fatty acids.

$-T\Delta S_{trans}$(kJ mol^{-1})	$-T\Delta S_{rot}$(kJ mol^{-1})	$-T\Delta S_{tot}$(kJ mol^{-1})
+66.3	+44.9	+111.2

Table 6.1. Estimation of entropy contributions of HBTP in 7A to ΔG. The entropies are evaluated for c_{crit} at $T = 298$ K (cf. section 4.3.6 for details).

Yet, an entirely different type of solvation can be expected for HBTP in 7A. DFT simulations of HBTP + 7A aggregates provide semi-quantitative values of the solvent-solute interaction strength (cf. Section 6.6). Two different configurations were compared: a structure where simultaneously the 7A hydroxyl forms a hydrogen bond with bromine and the carbonyl oxygen a weak hydrogen bond with a phenyl-hydrogen has a bond strength of -34.1 kJ mol^{-1} (cf. Fig. 6.6b); an alternative structure with 7A on top of HBTP bound only by dispersion forces has a higher bond strength of -49.8 kJ mol^{-1} (cf. Fig. 6.6a); The bond strength for both configurations is significantly lower than -67.8

kJ mol^{-1} for the hydrogen bonds between carboxylic acids. [143] Consequently, for HBTP in 7A, solvent-solvent interactions are significantly stronger than solute-solvent interactions, rendering formation of a strongly bound solvation shell unfavorable. These calculations suggest that the predominant interaction for solvation is van der Waals rather than hydrogen bonding. Also, adsorbed HBTP does not need to lose its “on-top” bound 7A molecules and therefore it can partly retain its solvation shell.

6.4 Supporting information

2,3,6,7,10,11-Hexabromotriphenylene (HBTP) was purchased from TCI Europe N.V. with a purity of >98%. 1-Heptanoic acid (7A) was purchased from Sigma-Aldrich with a purity of ≥99%. Both compounds were used as received without further purification.

6.4.1 STM experiments

Scanning Tunneling Microscopy (STM) experiments were conducted with a home-built low-drift instrument operated with a commercial ASC500 control electronics (attocube Systems AG, Munich). Highly Oriented Pyrolytic Graphite (ZYB grade, Optigraph GmbH, Berlin) was used and freshly cleaved prior to each experiment. Images were acquired directly at the liquid-solid interface with mechanically cut Pt/Ir tips. To avoid inaccuracies in the concentration dependent experiments due to spilling of solution or solvent evaporation, a rimmed sample holder was used with a relatively high solution volume (~40 µL).

The critical concentration c_{crit} was determined by probing solutions with different concentrations in STM experiments. The samples were obtained by diluting a stock solution prepared from 3.41 mg ± 0.10 mg HBTP and 10.0 mL heptanoic acid, corresponding to a concentration of 486 µmol L^{-1}. The relative volume error for the dilution is estimated as 4 %. Accordingly, the total concentration error related to solution preparation amounts to ~ 7 %.

In the STM experiments full monolayer coverage was still observed for a concentration of 30.4 µmol L^{-1}, whereas no adsorbed structures could be discerned anymore for a concentration of 27.0 µmol L^{-1}. Using a concentration of 30.4 µmol L^{-1} the self-assembled monolayer could be imaged in less than one minute. Consequently, slow kinetics is ruled out as a possible reason for the absence of self-assembled structures at the slightly lower concentration of 27.0 µmol L^{-1}.

Taking the above discussed concentration uncertainty of ~7 % into account results in an upper and lower boundary for c_{crit} of 32.5 µmol L^{-1} and 25.1 µmol L^{-1}, respectively. For evaluation of translational entropy the average value of 28.8 µmol was used, and section 6.3 an error margin of ± 3.7 µmol L^{-1} was stated.

6.4.2 Additional STM data

Split image

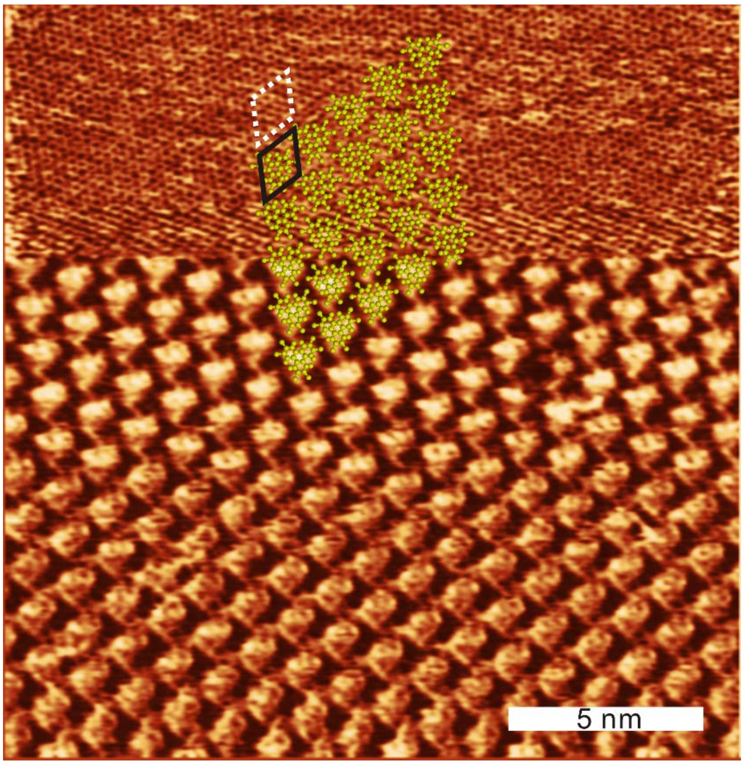

Figure. 6.4. High-resolution STM image of a HBTP monolayer acquired at the 7A-graphite interface. In the lower part, the HBTP superstructure was imaged with typical tunneling parameters of V_{sample} = -300 mV, I = 60 pA. In the upper part, the tunneling resistance was reduced by two orders of magnitude through switching the tunneling voltage to -3.0 mV. Consequently, the underlying graphite substrate could be imaged with atomic resolution. This so called “split-image” reveals an alignment of the graphite with the HBTP lattice vectors. The black rhombus indicates the HBTP unit cell. The white dashed rhombus also indicates the HBTP unit cell, but has been laterally shifted to illustrate the alignment between HBTB and graphite lattice vectors.

Overview image

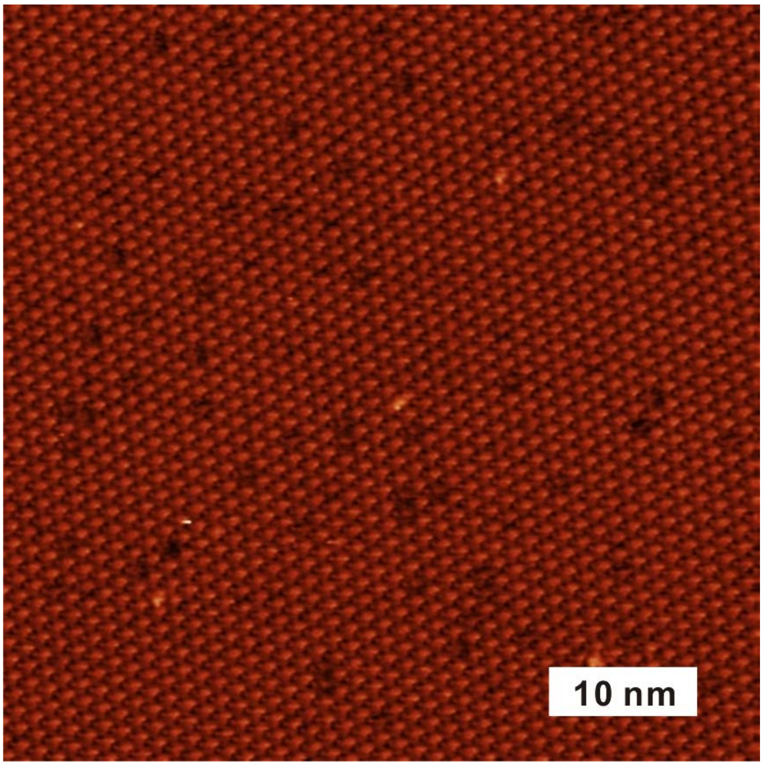

Figure. 6.5. Overview STM image of a HBTP monolayer acquired at the 7A–graphite interface (V_{sample} = -200 mV, I = 60 pA). The monolayer appears with uniform STM contrast. The absence of a periodic contrast modulation, i.e. a Moiré pattern, indicates similar adsorption sites of all HBTB molecules in a commensurate superstructure.

6.4.3 Density Functional Theory

Calculational Details

Initially, a free standing HBTP monolayer was simulated and optimized with the Quantum ESPRESSO program [207], using two density functional theory (DFT) based approaches: **(I)** a GGA-PBE functional [114] with an empirical dispersion correction (D2) proposed by Grimme (PBE+D), [115] and **(II)** a van der Waals density functional (vdW-DF).8 All DFT calculations were conducted with periodic boundary conditions. The accuracy of DFT derived energies for halogen bonds was first tested against higher level calculations: the PBE+D binding energy of a Br···N halogen bond in a pyridine-bromobenzene dimer (-11.4 kJ mol^{-1}) was very similar to the value obtained using MP2 (-8.9 kJ mol^{-1}) and to a published CCSD(T) value (-9.1 kJ mol^{-1}). [208] The energetic minimum for a free standing HBTP monolayer was found for a lattice parameter of $a = b = (12.48 \pm 0.01)$ Å, $\gamma = 120°$ (PBE+D calculations) and $a = b = (12.50 \pm 0.05)$ Å, $\gamma = 120°$ (vdW-DF calculations). The binding energy per molecule with respect to vacuum corresponds to -45.5 kJ mol^{-1} (PBE+D) or -48.3 kJ mol^{-1} (vdW-DF). The structure was constrained to a hexagonal lattice, but no further symmetry constraints were applied.

The underlying graphite was included in further calculations to estimate the total binding energy of HBTP in the adsorbed monolayer. In the first step a free standing HBTP monolayer was optimized with its lattice parameters constrained to the commensurate superstructure, i.e. $A = B = 5 \times a_{graphite} = 12.32$ Å and $\gamma = 120°$. This optimized HBTP structure was then adsorbed on a two layer graphite slab such that the positions of the HBTP triphenylene cores mimic the AB-stacking of graphite. For the final optimization of the combined system only the atomic coordinates of the lower graphite layer were fixed, while all atoms of the HBTP monolayer were free to relax laterally and vertically. However, there was no substantial lateral relaxation, indicating either a relatively flat potential energy hypersurface or that this configuration already corresponds to an energy minimum.

The total binding energy of HBTP in the adsorbed monolayer on graphite including molecule-molecule and molecule-surface interactions was calculated as:

$$\Delta H_{mono} = E_{graphite+monolayer} - E_{graphite} - E_{molecule} = -229.6 \text{ kJ mol}^{-1} \quad (6.3)$$

The adsorption energy of HBTP on graphite, i.e. the contribution of molecule-surface interactions, was calculated as:

$$E_{ads} = E_{graphite+monolayer} - E_{graphite} - E_{monolayer} = -186.1 \text{ kJ mol}^{-1} \quad (6.4)$$

$E_{molecule}$ corresponds to the energy of a single isolated HBTP molecule in the gas phase with similar structure as in the adsorbed monolayer; $E_{graphite+monolayer}$ / $E_{monolayer}$ and $E_{graphite}$ are referred to one HBTP unit cell and 5×5 graphite unit cells, respectively.

Additional results

However, the conformation of the 7A solvation shell around HBTP is expected to be entirely different from the 9A solvation shell around TPA and SDA. Further DFT simulations of the 7A-HBTP interactions were also conducted to compare the bond strength with binding energy of 7A-7A dimers. The energetic optimum of 7A-HBTP interaction is obtained with a binding energy of -49.8 kJ mol^{-1} for a 7A molecule adsorbed on top of a HBTP molecule. An energy of a hydrogen-bond conformation amounts to -34.1 kJ mol^{-1}. The bond strength is much lower than the highest binding energy of the two-fold hydrogen bonds -67.0 kJ mol^{-1}. Accordingly, predominant type of solvation is likely to be mediated by dispersion forces between 7A and the triphenylene core. However, a rigid adsorption of 7A is entropically less favorable. A rigid adsorbed 7A on HBTP results in an entropy loss of the system. As shown in Table 6.2, total entropy loss upon the formation of a rigid adsorbed HBTP-7A complex results in an unfavorable contribution to ΔG, i.e., $-T\Delta S_{tot} = -T\Delta S_{tot}(HBTP\text{-}7A) + T\Delta S_{tot}(7A) + T\Delta S_{tot}(HBTP)$ = +60.6 kJ mol^{-1}.

	$-T\Delta S_{trans}$(kJ mol^{-1})	$-T\Delta S_{rot}$(kJ mol^{-1})	$-T\Delta S_{tot}$ (kJ mol^{-1})
HBTP	+66.3	+44.9	+111.2
HBTP-7A	+66.9	+45.7	+113.0
HBTP-7A dimer	+67.4	+47.2	+114.6
7A	+29.1	+33.3	+62.4
7A-7A	+33.4	+42.3	+75.9

Table 6.2. Estimation of entropy contributions of HBTP, HBTP-7A, HBTP-7A-7A complexes, isolated 7A molecules, and 7A dimers. The entropies are evaluated for c_{crit} at T = 298 K.

On the other hand, the enthalpy gain upon formation of HBTP-7A complexes with respect to the solution phase is smaller than the binding enthalpy of an adsorbed HBTP-7A complex with respect to vacuum -49.8 kJ mol^{-1}. The energy of 7A in liquid state can be evaluated by the evaporation enthalpy of 7A liquid. However, since the dimer is not broken upon formation of HBTP-7A, the interaction related to the 2-fold hydrogen bonds is excluded. The evaporation enthalpy of 7A amounts to 72.9 kJ mol^{-1} [196], and the strength of hydrogen bonding interaction per 7A molecule can be considered as half the strength of 2-fold hydrogen bonds, i.e. 33.9 kJ mol^{-1} [143]. The difference of these two values yields a binding enthalpy of 7A liquid excluding hydrogen bonds amounts to 39.0 kJ mol^{-1} per 7A molecule. Accordingly, the total enthalpy gain upon formation of HBTP-7A complex amounts to -49.8+39.0 = -10.8 kJ mol^{-1}, which is much smaller than the unfavorable entropy contribution +60.6 kJ mol^{-1}. In other words, the formation of rigid HBTP-7A complex results in an increase of Gibbs free energy of ~50 kJ mol^{-1}. Hence, a rigid conformation of HBTP-7A is thermodynamically unfavorable. The 7A solvent shell around HBTP is more likely to be liquid like.

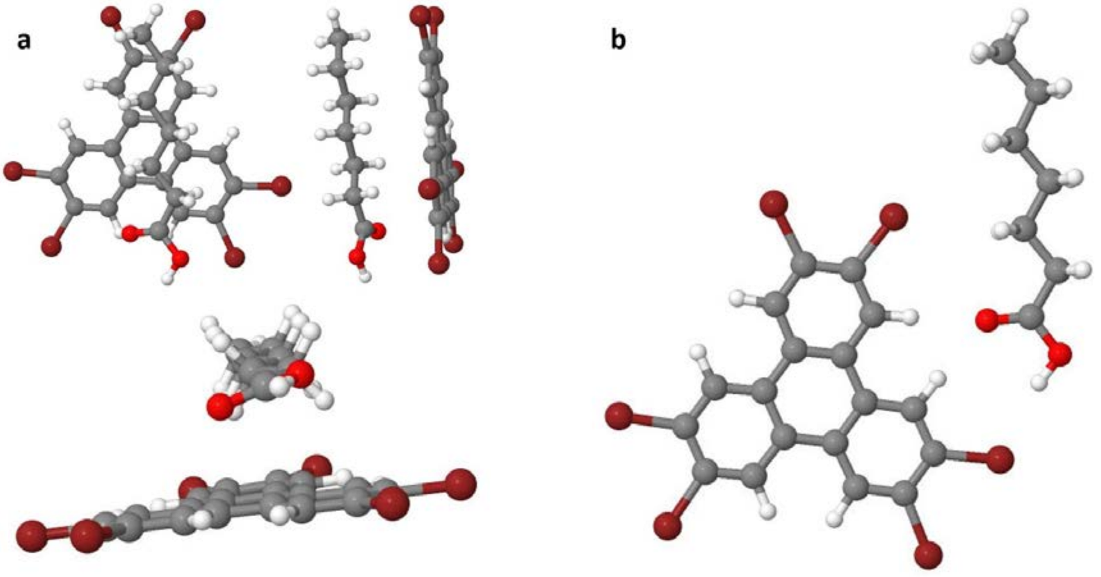

Figure. 6.6. Optimized structures of 7A + HBTP aggregates simulated with periodic boundary conditions using a 22 × 22 × 22 Å³ large super-cell. These simulations were carried out to estimate the strength of solute-solvent interactions for a semi-quantitative comparison to solvent-solvent interactions. (a) Different views of a configuration with 7A on top of HBTP; binding energy: -49.8 kJ mol^{-1}. (b) Configuration with 7A attached side-wise to HBTP through the combination of hydrogen bonds: 7A-carbonyl ⋯ HBTP-hydrogen and 7A-hydroxyl ⋯ HBTP-bromine; binding energy: -34.1 kJ mol^{-1}.

Since 7A molecules exist as dimers in the liquid phase, further entropy estimation is performed for a rigidly adsorbed 7A dimer on top of a HBTP molecule. The unfavorable entropy contribution related to a rigid adsorption of a 7A dimer on top of a HBTP is estimated as $-T\Delta S_{tot} = -T\Delta S_{tot}(HBTP\text{-}7A\text{-}7A) + T\Delta S_{tot}(7A\text{-}7A) + T\Delta S_{tot}(HBTP)$ = +72.5 kJ mol^{-1}. Although the interaction between 7A dimer and HBTP molecule was not simulated, the upper bound was estimated as twice the HBTP-7A interaction, since the second 7A molecule of the 7A dimer is not likely at the position of the energy minimum.

Accordingly, $\Delta H < 2 \times 10.8$ kJ mol^{-1}=21.6 kJ mol^{-1}, which is much smaller than the estimated entropy loss of 72.5 kJ mol^{-1}. Hence, the adsorption of a dimer is still thermodynamically unfavorable.

In conclusion, none of the possible rigid conformations are thermodynamically favorable, since the enthalpy gain of forming rigid complexs can not compensate the unfavorable entropy loss. Hence, we assume that the solvation of HBTP in 7A is dynamic and liquid-like. It only influences the binding enthalpy but has negligible influence on entropy.

6.5 Conclusion and summary

In conclusion, HBTP self-assembles into densely packed monolayers at the 7A-graphite interface, where each bromine forms intermolecular halogen bonds in a prototypical triangular cyclic arrangement. Simulations clearly indicate that by far the largest contribution to the stabilization of the monolayer arises from molecule-surface interactions through π-π bonds between graphite and the aromatic triphenylene core. The overall enthalpy difference for monolayer self-assembly from the supernatant liquid phase was deduced from a Born-Haber cycle. Accordingly, the solvent reduces the binding enthalpy gain to about 50% of the vacuum value, whereas for dicarboxylic acids a significantly more drastic effect was found in chapter 4 and 5. [16, 17] Based on a quantitative comparison of the overall enthalpy and entropy changes, we propose that the contributions from dewetting the substrate and stripping the weakly bound solvation shell cancel each other such that there are no significant net contributions to ΔG. This hypothesis is supported by energetic arguments: 7A-7A solvent-solvent hydrogen bond interactions are markedly stronger than the dispersive 7A-HBTP solvent-solute interactions. The predominant type of solvation is likely to be mediated by the solvent's interaction with the π-system of HBTP which is not fully lost after adsorption. This profoundly affects ΔG: there is no favourable entropy contribution due to desolvation; since the intermolecular halogen bonds are comparatively weak, strong molecule-surface interactions are required to render self-assembly of halogen bonded monolayers thermodynamically favourable.

Chapter 7: Conclusions and outlook

The quantitative understanding of the thermodynamic driving force of monolayer self-assembly provides important information for the targeted bottom-up fabrication of functional nanostructures. In the initial state, molecules are dissolved and solvated in the solvent. In the final state, molecules are desolvated and incorporated into an adsorbed monolayer on the surface. Since the overall enthalpy change of this monolayer self-assembly at the liquid-solid interface is difficult to measure directly using conventional calorimetry, a detour was taken via well-defined reference states with accessible enthalpy differences. To this end, enthalpy differences between the crystal and gas phase, crystal and solution, as well as the monolayer and gas phase were assessed by experimental methods, theoretical methods, or a hybrid of both. The respective enthalpy differences are then combined into an adapted Born-Haber cycle to deduce the overall enthalpy change. The quantification of the enthalpic driving force also enables a quantitative comparison with the theoretically estimated of the entropy contribution of self-assembly. Entropies are estimated using a theoretical model proposed by Whitesides *et al.* evaluated at the concentration threshold of self-assembly. For solutions with a lower concentration than the threshold, stable monolayers are not observed anymore.

In this work, two hydrogen bonded networks and one halogen bonded network were studied as model systems using the proposed method. Self-assembly of terephthalic acid (TPA) is studied at the 9A-graphite interface; self-assembly of 4, 4’-stilbenedicarboxylic acid (SDA) at the 9A-graphite interface; and hexabromotriphenylene (HBTP) self-assembly at the 7A-graphite interface. Based on thorough comparisons between the different systems, influences on self-assembly related to the solvation of monolayer, the solvation of solutes in solution, the temperature, the aromatic backbone as well as the type of intermolecular interactions were quantitatively evaluated:

1. Based on the Born-Haber cycle, overall enthalpy gains upon self-assembly of hydrogen bonded networks at the interfaces of fatty acids and graphite are found to be astonishingly small. The overall enthalpy change is lowered by the supernatant solution to only a few percent of the respective vacuum value for both TPA and SDA. This originates from the solvation of the monolayer and the enthalpy cost for desorption of the pre-adsorbed solvent layer. Since the desorption rate depends exponentially on the desorption energy, molecules in the interfacial monolayer are highly dynamic and exhibit a high vertical mobility. These results provide a quantitative rationale for abundantly observed dynamic exchange [175, 176] and concentration-induced phase transitions at the liquid-solid interface [168-170].

The overall enthalpy gain of HBTP self-assembly was deduced from a hybrid Born–Haber cycle. The solution reduces the total enthalpy gain to -109.2 kJ mol^{-1}, i.e. about 50% of the vacuum value of -229.6 kJ mol^{-1}. Based on a direct comparison, the enthalpy lowering related to the supernatant solution is remarkably weaker as compared to the cases of TPA and SDA self-assembly at the interface of 9A and graphite (95% for TPA and 90% for SDA). DFT results in an intermolecular interaction enthalpy of -43.5 kJ mol^{-1} per HBTP molecule, i.e. significantly weaker as compared to the cases of TPA and SDA (-76.8 kJ mol^{-1} and -73.0 kJ mol^{-1}, respectively). Hence, stronger surface-molecule interactions are required for the stabilization of the HBTP networks. Indeed, DFT simulations indicated that the largest contribution to the stabilization of the monolayer arises from molecule–surface interactions through π–π bonds between the graphite and the aromatic triphenylene core (-189 kJ mol^{-1} per HBTP molecule).

2. For both TPA and SDA, the estimated entropy of an unsolvated isolated molecule in solution is found to be significantly higher than the derived enthalpy gain upon monolayer self-assembly. This obvious contradiction to the experimental observation of stable monolayers indicates a significant solvation effect of molecules in solution. Hence, we propose a solvation model, where TPA and SDA solutes break fatty acid dimers and bond with solvent monomers via two 2-fold cyclic hydrogen bonds. Further entropy estimates based on the formation of hydrogen bonded solute-solvent complexes reveals that the entropy loss is reduced owing to the formation of the solvation shell in solution. Therefore, release of the solvation shell actually renders self-assembly a thermodynamically favorable process. On the other hand, the 2-fold cyclic hydrogen bonds that have to be broken by the dissolution from bulk crystals are regained upon solvation by the formation of solute-solvent complexes in solution. This also explains the relatively low dissolution enthalpies of dicarboxylic acids in fatty acid solvents.

   However, for the case of HBTP networks, a quantitative comparison of the overall enthalpy and entropy changes suggests that solvation makes no significant net contributions to ΔS. This hypothesis is supported by further DFT derived binding energies: 7A–7A solvent–solvent hydrogen bond interactions are markedly stronger than dispersive 7A–HBTP solvent-solute interactions. Further entropy estimations suggest that static adsorption of 7A molecules on HBTP in solution is thermodynamically unfavorable. This leads to the conclusion that the HBTP solvation shell is not stably bound, and hence does not give rise to a significant entropy contribution by desolvation.

3. The influence of an extended aromatic system on the thermodynamic stability of monolayers is quantified by a thorough comparison of SDA with TPA. All individual enthalpy contributions and the entropies were compared independently. The Born-Haber cycle yields a total enthalpy change of SDA self-assembly of -24.3 kJ mol^{-1} more than 3 times as large as that the -7.3 kJ mol^{-1} of TPA The measured sublimation enthalpy of TPA is ~42 kJ mol^{-1} lower than that of SDA. Yet, the binding energy of TPA molecules in the adsorbed (unsolvated) monolayer is ~64 kJ mol^{-1} weaker than that of SDA. This means the second phenyl ring of SDA increases the binding energy in the monolayer on graphite by almost 50 % more than the binding energy in the crystal. Hence, the extended aromatic system of SDA leads to a significant increase of the adsorbed monolayer binding energy. For the case of HBTP, this enhancement is even more significant. The sublimation enthalpy +137.9 kJ mol^{-1} is somewhat weaker than that of SDA +169.0 kJ mol^{-1}, due to the weaker intermolecular interaction of HBTP in the bulk crystal. However, the monolayer binding enthalpy per HBTP molecule of -229.6 kJ mol^{-1} is significantly larger than the value of SDA -189.0 kJ mol^{-1} (MM simulations) owing to the even larger aromatic system of HBTP.

   On the other hand, the dissolution enthalpy of SDA in 9A is almost twice as large as for TPA. Since in both cases, the dissolution is endothermic, a high value for SDA means that molecules in solution phase are less stable, and crystallization (or monolayer formation) of SDA from solution results in a higher energy gain than in the case of TPA. This additionally enhances the stability of interfacial SDA monolayers.

4. Temperature dependent STM measurements show the reversible desorption and reformation of TPA monolayers around a sharply defined transition temperature of 44°C±1°C. These results provide direct and solid evidence of a low desorption barrier, i.e. the low enthalpy gain of self-assembly at the solution-solid interface. Without considering the entropy gain of desorbing the pre-adsorbed 9A layer, the entropy contribution upon is evaluated using the critical temperature (44°C) as +30.8 kJ mol^{-1}. Yet, considering the dewetting entropy gain of desorbing the pre-adsorbed 9A layer, the entropy cost was obtained to be +12.0 kJ mol^{-1}, in perfect agreement with the entropy loss at room temperature of +12.3 kJ mol^{-1}using the concentration threshold of self-assembly. Since $\Delta H \approx T\Delta S$ at these critical conditions, this agreement also proves the low temperature dependence of the total enthalpy gain upon self-assembly.

In conclusion, the proposed Born-Haber cycle is applicable to different systems of interest and provides quantitative thermodynamic insights into monolayer self-assembly with a clear account of individual enthalpy contributions. The direct comparison between experimental and theoretical results provides important benchmarking for simulations. The energetic accuracy obtained with parameterized force fields gives confidence for broader studies of hydrogen bonded systems. By evaluating and comparing the free energy gain of various polymorphs in different solvents, the Born-Haber cycle method has the potential to also explain solvent-induced polymorphism quantitatively. Meanwhile, hybrid Born-Haber cycles constructed from a combination of experiments and simulations are proven to be an efficient method and have the potential to evaluate the thermodynamics of more complex systems. However, further improvements in the proposed approach are required for an assessment of the dewetting enthalpy. Also, for self-assembly with phase coexistence, the implementation of a Born−Haber cycle might become intricate.

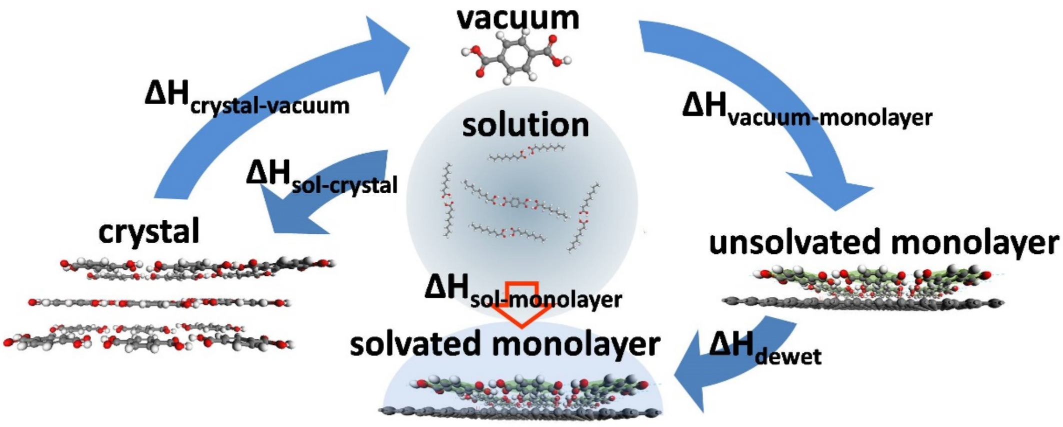
vacuum
ΔH crystal-vacuum
solution
ΔH vacuum-monolayer
ΔH sol-crystal
crystal
unsolvated monolayer
ΔH sol-monolayer
solvated monolayer
ΔH dewet

Figure 7.1. TOC graphic of Chapter 4. A scheme of the Born-Haber cycle for TPA self-assembly at the 9A-graphite interface. By directly assessing the enthalpy changes indicated by the blue arrows, the total enthalpy change upon self-assembly (red arrow) is obtained indirectly. [16]

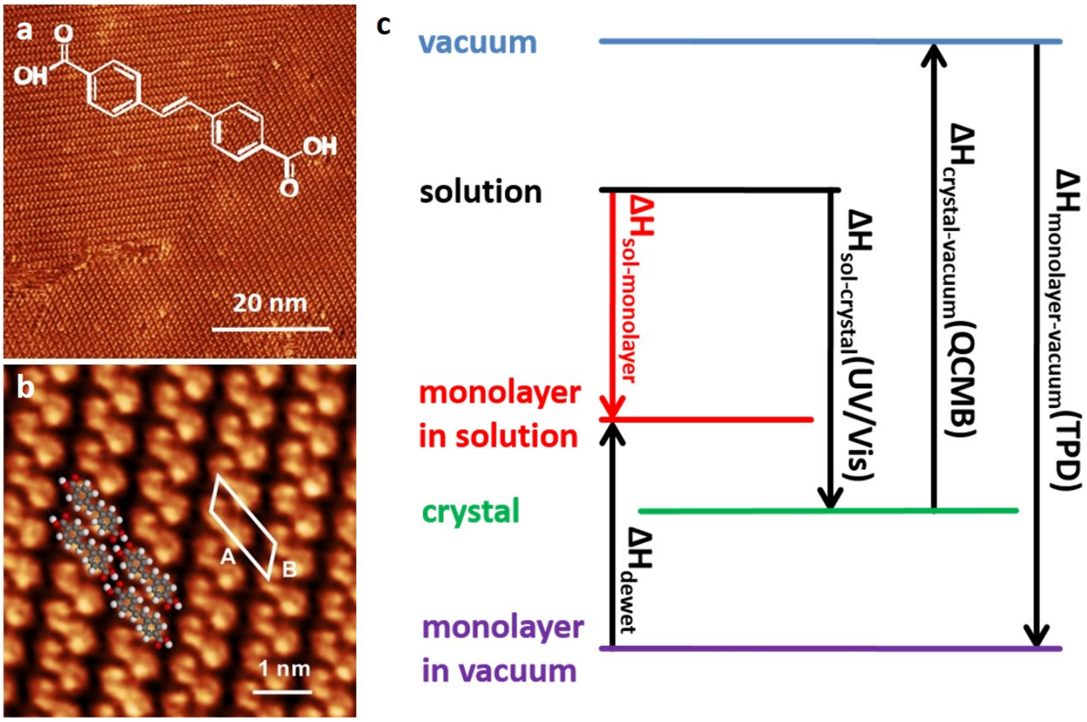
a
O
OH
OH
O
20 nm
b
A
B
1 nm
c
vacuum
solution
monolayer in solution
crystal
monolayer in vacuum
ΔH sol-monolayer
ΔH sol-crystal (UV/Vis)
ΔH crystal-vacuum (QCMB)
ΔH monolayer-vacuum (TPD)
ΔH dewet

Figure 7.2. TOC graphic of Chapter 5. STM images and the Born-Haber cycle of SDA self-assembly at the 9A-graphite interface. An overview STM image and a high resolution STM image is given in (a) and (b). A scheme of the Born-Haber cycle is illustrated in (c). In this work the influence of the extended aromatic system of SDA on self-assembly is quantified. [17]

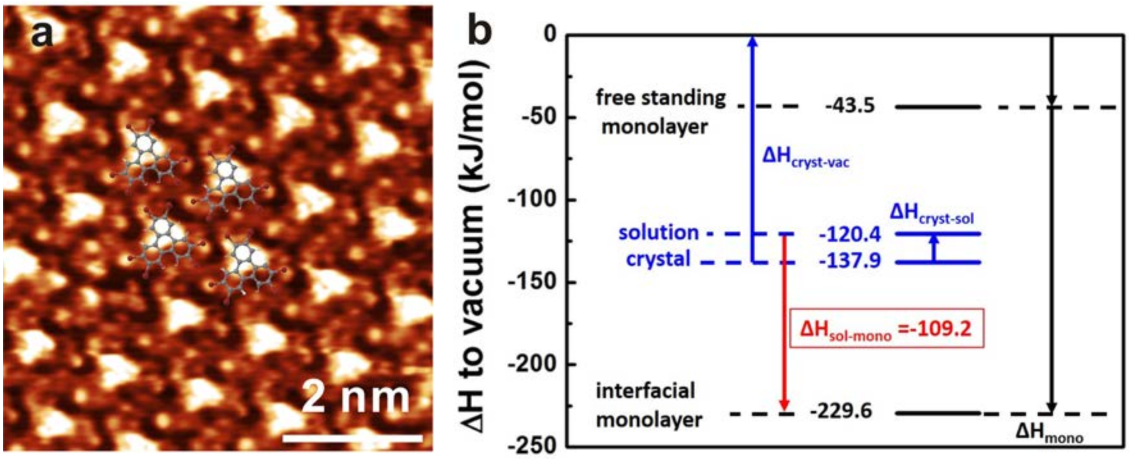

Figure 7.3. TOC graphic of Chapter 6. Thermodynamic driving force of halogen bonded networks at the 7A-graphite interface is determined using a hybrid Born-Haber cycle. (a) high resolution STM image of HBTP monolayer at 7A-graphite interface; (b) hybrid Born-Haber cycle of HBTP self-assembly at the 7A-graphite interface. [45]

References

1. Lehn, J.M., *Supramolecular chemistry—scope and perspectives molecules, supermolecules, and molecular devices (Nobel Lecture).* Angew. Chem. Int. Ed., 1988. **27**(1): p. 89-112. http://dx.doi.org/10.1002/anie.198800891.

2. Desiraju, G.R., *Chemistry beyond the molecule.* Nature, 2001. **412**(6845): p. 397-400. http://dx.doi.org/10.1038/35086640.

3. Desiraju, G.R., *Supramolecular synthons in crystal engineering—a new organic synthesis.* Angew. Chem. Int. Ed., 1995. **34**(21): p. 2311-2327. http://dx.doi.org/10.1002/anie.199523111.

4. Kuduva, S.S., et al., *Cubanecarboxylic Acids. Crystal Engineering Considerations and the Role of CH···O Hydrogen Bonds in Determining OH···O Networks.* J. Am. Chem. Soc., 1999. **121**(9): p. 1936-1944. http://dx.doi.org/10.1021/ja981967u.

5. Li, H., et al., *Design and synthesis of an exceptionally stable and highly porous metal-organic framework.* Nature, 1999. **402**(6759): p. 276-279. http://dx.doi.org/10.1038/46248.

6. Knoll, W., et al., *Streptavidin arrays as supramolecular architectures in surface-plasmon optical sensor formats.* Colloid Surf. A-Physicochem. Eng. Asp., 2000. **161**(1): p. 115-137. http://dx.doi.org/10.1016/s0927-7757(99)00331-3.

7. Piot, L., et al., *Long-Range Alignments of Single Fullerenes by Site-Selective Inclusion into a Double-Cavity 2D Open Network.* J. Am. Chem. Soc., 2009. **131**(36): p. 12864. http://dx.doi.org/10.1021/ja902621t.

8. Bigioni, T.P., et al., *Kinetically driven self assembly of highly ordered nanoparticle monolayers.* Nat. Mater., 2006. **5**(4): p. 265-270. http://dx.doi.org/10.1038/nmat1611.

9. De Feyter, S. and F.C. De Schryver, *Two-dimensional supramolecular self-assembly probed by scanning tunneling microscopy*. Chem. Soc. Rev., 2003. **32**(3): p. 139-150. http://dx.doi.org/10.1039/B206566P.

10. Wan, L.-J., *Fabricating and Controlling Molecular Self-Organization at Solid Surfaces: Studies by Scanning Tunneling Microscopy.* Acc. Chem. Res., 2006. **39**(5): p. 334-342. http://dx.doi.org/10.1021/ar0501929.

11. Lackinger, M. and W.M. Heckl, *Carboxylic Acids: Versatile Building Blocks and Mediators for Two-Dimensional Supramolecular Self-Assembly*. Langmuir, 2009. **25**(19): p. 11307-11321. http://dx.doi.org/10.1021/la900785f.

12. Elemans, J., S.B. Lei, and S. De Feyter, *Molecular and Supramolecular Networks on Surfaces: From Two-Dimensional Crystal Engineering to Reactivity*. Angew. Chem. Int. Ed., 2009. **48**(40): p. 7298-7332. http://dx.doi.org/10.1002/anie.200806339.

13. Lehn, J.M., *Perspectives in supramolecular chemistry - from molecular recognition towards molecular information-processing and self-organization.* Angew. Chem. Int. Ed., 1990. **29**(11): p. 1304-1319. http://dx.doi.org/10.1002/anie.199013041.

14. Lehn, J.M., *Supramolecular chemistry: from molecular information towards self-organization and complex matter.* Rep. Prog. Phys., 2004. **67**(3): p. 249-265. http://dx.doi.org/10.1088/0034-4885/67/3/r02.

15. Datta, A. and S.K. Pati, *Dipolar interactions and hydrogen bonding in supramolecular aggregates: understanding cooperative phenomena for 1st hyperpolarizability.* Chem. Soc. Rev., 2006. **35**(12): p. 1305-1323. http://dx.doi.org/10.1039/b605478a.

16. Song, W., et al., *Born–Haber Cycle for Monolayer Self-Assembly at the Liquid–Solid Interface: Assessing the Enthalpic Driving Force.* J. Am. Chem. Soc., 2013. **135**(39): p. 14854-14862. http://dx.doi.org/10.1021/ja407698t.

17. Song, W., et al., *Thermodynamics of 4,4'-stilbenedicarboxylic acid monolayer self-assembly at the nonanoic acid-graphite interface.* Phys. Chem. Chem. Phys., 2014. **16**(26): p. 13239-13247. http://dx.doi.org/10.1039/C4CP01147C.

18. Giancarlo, L.C. and G.W. Flynn, *Raising Flags: Applications of Chemical Marker Groups To Study Self-Assembly, Chirality, and Orientation of Interfacial Films by Scanning Tunneling Microscopy.* Acc. Chem. Res., 2000. **33**(7): p. 491-501. http://dx.doi.org/10.1021/ar970261m.

19. Cyr, D.M., B. Venkataraman, and G.W. Flynn, *STM Investigations of Organic Molecules Physisorbed at the Liquid−Solid Interface.* Chem. Mater., 1996. **8**(8): p. 1600-1615. http://dx.doi.org/10.1021/cm960113a.

20. Kampschulte, L., et al., *Thermodynamical equilibrium of binary supramolecular networks at the liquid-solid interface.* J. Am. Chem. Soc., 2008. **130**(26): p. 8502-8507. http://dx.doi.org/10.1021/ja801883t.

21. Gutzler, R., et al., *Reversible Phase Transitions in Self-Assembled Monolayers at the Liquid-Solid Interface: Temperature-Controlled Opening and Closing of Nanopores.* J. Am. Chem. Soc., 2010. **132**(14): p. 5084-5090. http://dx.doi.org/10.1021/ja908919r.

22. Bellec, A., et al., *Solution-growth kinetics and thermodynamics of nanoporous self-assembled molecular monolayers.* J. Chem. Phys., 2011. **134**(12): p. 124702. http://dx.doi.org/10.1063/1.3569132.

23. De Feyter, S. and F.C. De Schryver, *Two-dimensional supramolecular self-assembly probed by scanning tunneling microscopy.* Chem. Soc. Rev., 2003. **32**(6): p. 393-393. http://dx.doi.org/10.1039/B206566P.

24. Friesen, B.A., et al., *Single Molecule Imaging of Oxygenation of Cobalt Octaethylporphyrin at the Solution/Solid Interface: Thermodynamics from Microscopy.* J. Am. Chem. Soc., 2012. **134**(36): p. 14897-14904. http://dx.doi.org/10.1021/ja304431b.

25. Bouteiller, L., *Assembly via hydrogen bonds of low molar mass compounds into supramolecular polymers*, in *Hydrogen Bonded Polymers*, 2007, Springer-Verlag Berlin: Berlin. p. 79-112. http://dx.doi.org/10.1007/12_2006_110.

26. Bellec, A., et al., *Solution-growth kinetics and thermodynamics of nanoporous self-assembled molecular monolayers.* J. Chem. Phys., 2011. **134**(12): p. 124702. http://dx.doi.org/10.1063/1.3569132.

27. Lei, S.B., et al., *One building block, two different supramolecular surface-confined patterns: Concentration in control at the solid-liquid interface.* Angew. Chem. Int. Ed., 2008. **47**(16): p. 2964-2968. http://dx.doi.org/10.1002/anie.200705322.

28. Meier, C., et al., *Concentration and Coverage Dependent Adlayer Structures: From Two-Dimensional Networks to Rotation in a Bearing.* J. Phys. Chem. C, 2010. **114**(2): p. 1268-1277. http://dx.doi.org/10.1021/jp910029z.

29. Blunt, M.O., et al., *Temperature-Induced Structural Phase Transitions in a Two-Dimensional Self-Assembled Network.* J. Am. Chem. Soc., 2013. **135**(32): p. 12068-12075. http://dx.doi.org/10.1021/ja405585s.

30. Dienstmaier, J.F., et al., *On the Scalability of Supramolecular Networks - High Packing Density vs. Optimized Hydrogen Bonds in Tricarboxylic Acid Monolayers.* Langmuir, 2010. **26**(13): p. 10708-10716. http://dx.doi.org/10.1021/la101634w.

31. Eder, G., et al., *Incorporation Dynamics of Molecular Guests into Two-Dimensional Supramolecular Host Networks at the Liquid-Solid Interface.* Langmuir, 2011. **27**(22): p. 13563-13571. http://dx.doi.org/10.1021/la203054k.

32. Lackinger, M., et al., *Dynamics of grain boundaries in two-dimensional hydrogen-bonded molecular networks.* Small, 2005. **1**(5): p. 532-539. http://dx.doi.org/10.1002/smll.200400078.

33. Uemura, S., et al., *Molecular Dynamics in Two-Dimensional Supramolecular Systems Observed by STM.* Materials, 2010. **3**(8): p. 4252-4276. http://dx.doi.org/10.3390/ma3084252.

34. Martsinovich, N. and A. Troisi, *Modeling the Self-Assembly of Benzenedicarboxylic Acids Using Monte Carlo and Molecular Dynamics Simulations.* J. Phys. Chem. C, 2010. **114**(10): p. 4376-4388. http://dx.doi.org/10.1021/jp911671b.

35. Adisoejoso, J., et al., *One building block, two different nanoporous self-assembled monolayers: a combined STM and Monte Carlo study.* ACS Nano, 2011. **6**(1): p. 897-903. http://dx.doi.org/10.1021/nn204398m.

36. Weber, U.K., et al., *Role of Interaction Anisotropy in the Formation and Stability of Molecular Templates.* Phys. Rev. Lett., 2008. **100**(15): p. 156101. http://dx.doi.org/10.1103/PhysRevLett.100.156101.

37. Lei, S., et al., *Mixing Behavior of Alkoxylated Dehydrobenzo[12]annulenes at the Solid–Liquid Interface: Scanning Tunneling Microscopy and Monte Carlo Simulations.* ACS Nano, 2011. **5**(5): p. 4145-4157. http://dx.doi.org/10.1021/nn200874k.

38. Gutzler, R., et al., *Halogen bonds as stabilizing interactions in a chiral self-assembled molecular monolayer.* Chem. Commun., 2011. **47**(33): p. 9453-9455. http://dx.doi.org/10.1039/C1CC13114A.

39. Chung, K.-H., et al., *Polymorphic porous supramolecular networks mediated by halogen bonds on Ag (111).* Chem. Commun., 2011. **47**(41): p. 11492-11494. http://dx.doi.org/10.1039/C1CC14679C

40. Voth, A.R., et al., *Halogen bonds as orthogonal molecular interactions to hydrogen bonds.* Nat. Chem., 2009. **1**(1): p. 74-79. http://dx.doi.org/10.1038/nchem.112.

41. Groszek, A.J., *Selective adsorption at graphite/hydrocarbon interfaces.* Proc. R. Soc. Lond. A, Math. Phys. Sci., 1969. **314**(1519): p. 473-498. http://dx.doi.org/10.1098/rspa.1970.0019.

42. Tahara, K., et al., *Two-dimensional porous molecular networks of dehydrobenzo [12] annulene derivatives via alkyl chain interdigitation.* J. Am. Chem. Soc., 2006. **128**(51): p. 16613-16625. http://dx.doi.org/10.1021/ja0655441.

43. Yang, Y.L. and C. Wang, *Solvent effects on two-dimensional molecular self-assemblies investigated by using scanning tunneling microscopy.* Curr. Opin.

Colloid Interface Sci., 2009. **14**(2): p. 135-147. http://dx.doi.org/10.1016/j.cocis.2008.10.002.

44. Jahanbekam, A., et al., *Temperature Stability of Three Commensurate Surface Structures of Coronene Adsorbed on Au(111) from Heptanoic Acid in the 0 to 60 °C Range*. J. Phys. Chem. C, 2013. **117**(6): p. 2914-2919. http://dx.doi.org/10.1021/jp3115435.

45. Song, W., et al., *Thermodynamics of halogen bonded monolayer self-assembly at the liquid-solid interface.* Chem. Commun., 2014. **50**(88): p. 13465-13468. http://dx.doi.org/10.1039/C4CC06251E.

46. Binnig, G., et al., *Surface studies by scanning tunneling microscopy*. Phys. Rev. Lett., 1982. **49**(1): p. 57. http://dx.doi.org/10.1103/PhysRevLett.49.57.

47. Bhushan, B., *Springer handbook of nanotechnology*. 2010: Springer.

48. Griessl, S.J., et al., *Incorporation and manipulation of coronene in an organic template structure.* Langmuir, 2004. **20**(21): p. 9403-9407. http://dx.doi.org/10.1021/la049441c.

49. Lackinger, M., et al., *Self-assembly of benzene-dicarboxylic acid isomers at the liquid solid interface: Steric aspects of hydrogen bonding.* J. Phys. Chem. B, 2004. **108**(36): p. 13652-13655. http://dx.doi.org/10.1021/jp048248o.

50. Kambara, H., et al., *Construction of a versatile ultralow temperature scanning tunneling microscope.* Rev. Sci. Instrum., 2007. **78**(7): p. 5. http://dx.doi.org/10.1063/1.2751095.

51. Besocke, K., *An easily operable scanning tunneling microscope.* Surf. Sci., 1987. **181**(1–2): p. 145-153. http://dx.doi.org/10.1016/0039-6028(87)90151-8.

52. Frohn, J., et al., *Coarse Tip Distance Adjustment And Positioner For A Scanning Tunneling Microscope.* Rev. Sci. Instrum., 1989. **60**(6): p. 1200-1201. http://dx.doi.org/10.1063/1.1140287.

53. Wilms, M., et al., *New and versatile ultrahigh vacuum scanning tunneling microscope for film growth experiments.* Rev. Sci. Instrum., 1998. **69**(7): p. 2696-2703. http://dx.doi.org/10.1063/1.1149001.

54. Lackinger, M., et al., *Self-assembly of trimesic acid at the liquid-solid interface - a study of solvent-induced polymorphism.* Langmuir, 2005. **21**(11): p. 4984-4988. http://dx.doi.org/10.1021/la0467640.

55. Schlögl, S., Influence of Reaction Parameters on the Bottom-Up Synthesis of Two-Dimensional Polymers, PhD Thesis, 2013, Tech. Univ. Munich, Germany, http://mediatum.ub.tum.de/doc/1135575/1135575.pdf.

56. Sirtl, T., Influences on Structure Formation in Surface-Supported Organic Nanostructures, PhD Thesis, 2013, Tech. Univ. Munich, Germany, http://d-nb.info/1047471930/34.

57. Dienstmaier, J., From Supramolecular Self-Assembly to Two-Dimensional Covalent Organic Frameworks, PhD Thesis, 2012, University of Munich, Germany, http://edoc.ub.uni-muenchen.de/15662/1/Dienstmaier_Juergen_F.pdf.

58. Binnig, G., et al., *Tunneling through a controllable vacuum gap.* Appl. Phys. Lett., 1982. **40**(2): p. 178-180. http://dx.doi.org/10.1063/1.92999

59. Mark, G.I., L.P. Biro, and P. Lambin, *Modeling and interpretation of STM images of carbon nanosystems*. Frontiers of Multifunctional Nanosystems, 2002, Dordrecht: Springer. 43-58. http://dx.doi.org/10.1007/978-94-010-0341-4_4.

60. Bardeen, J., *Transfer Hamiltonian of solid tunneling structure.* Phys. Rev. Lett., 1961. **6**: p. 57. http://dx.doi.org/10.1103/PhysRevLett.6.57.

61. Meyer, E., H.J. Hug, and R. Bennewitz, *Scanning probe microscopy: the lab on a tip*. 2004: Springer.

62. Tersoff, J. and D. Hamann, *Theory and application for the scanning tunneling microscope.* Phys. Rev. Lett., 1983. **50**(25): p. 1998. http://dx.doi.org/10.1103/PhysRevLett.50.1998.

63. Tersoff, J. and D. Hamann, *Theory of the scanning tunneling microscope*. Phys. Rev. B, 1985. **31**: p. 805-813. http://dx.doi.org/10.1103/PhysRevB.31.805.

64. Wintterlin, J., et al., *Atomic-resolution imaging of close-packed metal surfaces by scanning tunneling microscopy*. Phys. Rev. Lett., 1989. **62**(1): p. 59. http://dx.doi.org/10.1103/PhysRevLett.62.59.

65. Binnig, G. and H. Rohrer, *Scanning tunneling microscopy—from birth to adolescence*. Rev. Mod. Phys., 1987. **59**(3): p. 615-625. http://dx.doi.org/10.1103/RevModPhys.59.615.

66. Binnig, G., et al., *7× 7 reconstruction on Si (111) resolved in real space*. Phys. Rev. Lett., 1983. **50**(2): p. 120. http://dx.doi.org/10.1103/PhysRevLett.50.120.

67. Ritter, E., et al., *Direct observation of a nucleation and growth process on an atomic scale*. Surf. Sci., 1987. **181**(1): p. 403-411. http://dx.doi.org/10.1016/0039-6028(87)90184-1.

68. Kopatzki, E. and R.J. Behm, *STM imaging and local order of oxygen adlayers on Ni(100)*. Surf. Sci., 1991. **245**(3): p. 255-262. http://dx.doi.org/10.1016/0039-6028(91)90028-q.

69. Ramos, M., *Can STM be used to image molecules on surfaces?* J. Phys.: Condens. Matter, 1993. **5**(18): p. 2843. http://dx.doi.org/10.1088/0953-8984/5/18/005.

70. Hallmark, V.M. and S. Chiang, *Predicting STM images of molecular adsorbates*. Surf. Sci., 1995. **329**(3): p. 255-268. http://dx.doi.org/10.1016/0039-6028(95)00047-x.

71. Lippel, P.H., et al., *High-resolution imaging of copper-phthalocyanine by scanning-tunneling microscopy*. Phys. Rev. Lett., 1989. **62**(2): p. 171-174. http://dx.doi.org/10.1103/PhysRevLett.62.171.

72. Smith, D.P.E., et al., *Structure, registry and imaging mechanism of alkylcyanobiphenyl molecules by tunneling microscopy.* Nature, 1990. **344**(6267): p. 641-644. http://dx.doi.org/10.1038/344641a0.

73. Lang, N., *Vacuum tunneling current from an adsorbed atom.* Phys. Rev. Lett., 1985. **55**(2): p. 230-233. http://dx.doi.org/10.1103/PhysRevLett.55.230.

74. Lang, N., *Theory of Single-Atom Imaging in the Scanning Tunneling Microscope.* Phys. Rev. Lett., 1986. **56**(11): p. 1164-1167. http://dx.doi.org/10.1103/PhysRevLett.56.1164.

75. Eigler, D., et al., *Imaging Xe with a low-temperature scanning tunneling microscope.* Phys. Rev. Lett., 1991. **66**(9): p. 1189. http://dx.doi.org/10.1103/PhysRevLett.66.1189.

76. Chen, C.J., *Tunneling matrix elements in three-dimensional space: The derivative rule and the sum rule.* Phys. Rev. B, 1990. **42**(14): p. 8841. http://dx.doi.org/10.1103/PhysRevB.42.8841.

77. Chen, C.J., *Microscopic view of scanning tunneling microscopy.* J. Vac. Sci. Technol. A-Vac. Surf. Films, 1991. **9**(1): p. 44-50. http://dx.doi.org/10.1116/1.577128.

78. Chen, C.J., *Origin of atomic resolution on metal-surfaces in scanning tunneling microscopy.* Phys. Rev. Lett., 1990. **65**(4): p. 448-451. http://dx.doi.org/10.1103/PhysRevLett.65.448.

79. Sautet, P. and C. Joachim, *Electronic transmission coefficient for the single-impurity problem in the scattering-matrix approach.* Phys. Rev. B, 1988. **38**(17): p. 12238-12247. http://dx.doi.org/10.1103/PhysRevB.38.12238.

80. Sautet, P., *Images of adsorbates with the scanning tunneling microscope: Theoretical approaches to the contrast mechanism.* Chem. Rev., 1997. **97**(4): p. 1097-1116. http://dx.doi.org/10.1021/cr9600823.

81. Sautet, P., J.C. Dunphy, and M. Salmeron, *The origin of STM contrast differences for inequivalent S atoms on a Mo(100) surface.* Surf. Sci., 1996. **364**(3): p. 335-344. http://dx.doi.org/10.1016/0039-6028(96)00622-x.

82. Sautet, P. and C. Joachim, *Calculation of the benzene on rhodium STM images.* Chem. Phys. Lett., 1991. **185**(1–2): p. 23-30. http://dx.doi.org/10.1016/0009-2614(91)80133-I.

83. Gottlieb, A.D. and L. Wesoloski, *Bardeen's tunnelling theory as applied to scanning tunnelling microscopy: a technical guide to the traditional interpretation.* Nanotechnology, 2006. **17**(8): p. R57. http://dx.doi.org/10.1088/0957-4484/17/8/R01.

84. Binnig, G. and D.P.E. Smith, *Single-tube 3-dimensional scanner for scanning tunneling microscopy.* Rev. Sci. Instrum., 1986. **57**(8): p. 1688-1689. http://dx.doi.org/10.1063/1.1139196.

85. Schaake, R.C.F., J.C. van Miltenburg, and C.G. de Kruif, *Thermodynamic properties of the normal alkanoic acids I. Molar heat capacities of seven odd-numbered normal alkanoic acids.* J. Chem. Thermodyn., 1982. **14**(8): p. 763-769. http://dx.doi.org/10.1016/0021-9614(82)90172-0.

86. Gutzler, R., W.M. Heckl, and M. Lackinger, *Combination of a Knudsen effusion cell with a quartz crystal microbalance: In situ measurement of molecular evaporation rates with a fully functional deposition source.* Rev. Sci. Instrum., 2010. **81**(1): p. 015108. http://dx.doi.org/10.1063/1.3292510.

87. Sauerbrey, G., *Verwendung von Schwingquarzen zur Wägung dünner Schichten und zur Mikrowägung.* Z. Phys., 1959. **155**(2): p. 206-222. http://dx.doi.org/10.1007/BF01337937.

88. Freedman, A., et al., *Apparatus for determination of vapor pressures at ambient temperatures employing a Knudsen effusion cell and quartz crystal microbalance.* Meas. Sci. Technol., 2008. **19**(12): p. 125102. http://dx.doi.org/10.1088/0957-0233/19/12/125102.

89. Busca, G., et al., *Chemical and mechanistic aspects of the selective catalytic reduction of NOx by ammonia over oxide catalysts: A review.* Appl. Catal., B, 1998. **18**(1-2): p. 1-36. http://dx.doi.org/10.1016/s0926-3373(98)00040-x.

90. Engelhardt, H.A. and D. Menzel, *Adsorption of oxygen on silver single-crystal surfaces.* Surf. Sci., 1976. **57**(2): p. 591-618. http://dx.doi.org/10.1016/0039-6028(76)90350-2.

91. Kahlich, M.J., H.A. Gasteiger, and R.J. Behm, *Kinetics of the Selective CO Oxidation in H_2-Rich Gas on Pt/Al_2O_3.* J. Catal., 1997. **171**(1): p. 93-105. http://dx.doi.org/10.1006/jcat.1997.1781.

92. Mhadeshwar, A.B. and D.G. Vlachos, *A catalytic reaction mechanism for methane partial oxidation at short contact times, reforming, and combustion, and for oxygenate decomposition and oxidation on platinum.* Ind. Eng. Chem. Res., 2007. **46**(16): p. 5310-5324. http://dx.doi.org/10.1021/ie070322c.

93. Jin, W.Q., et al., *Efficient catalytic decomposition of CO2 to CO and O2 over Pd/mixed-conducting oxide catalyst in an oxygen-permeable membrane reactor.* Environ. Sci. Technol., 2008. **42**(8): p. 3064-3068. http://dx.doi.org/10.1021/es702913f.

94. Ota, H., et al., *TPD-GC/MS analysis of the solid electrolyte interface (SEI) on a graphite anode in the propylene carbonate/ethylene sulfite electrolyte system for lithium batteries.* J. Power Sources, 2001. **97-8**: p. 107-113. http://dx.doi.org/10.1016/s0378-7753(01)00738-8.

95. Madey, T.E. and J.T. Yates, *Adsorption of cycloparaffins on Ru(001) as studied by temperature programmed desorption and electron stimulated desorption.* Surf. Sci., 1978. **76**(2): p. 397-414. http://dx.doi.org/10.1016/0039-6028(78)90105-x.

96. Sault, A.G., R.J. Madix, and C.T. Campbell, *Adsorption of oxygen and hydrogen on Au(110)-(1×2).* Surf. Sci., 1986. **169**(2-3): p. 347-356. http://dx.doi.org/10.1016/0039-6028(86)90616-3.

97. Taylor, P.A., et al., *Adsorption and decomposition of acetylene on Si(100)-(2 × 1).* J. Am. Chem. Soc., 1992. **114**(17): p. 6754-6760. http://dx.doi.org/10.1021/ja00043a020.

98. Walch, H., Molecular Networks Through Surface-Mediated Reactions-From Hydrogen Bonds to Covalent Links, PhD Thesis, 2011, University of Munich, Germany, http://nbn-resolving.de/urn:nbn:de:bvb:19-127102.

99. Redhead, P.A., *Thermal desorption of gases.* Vacuum, 1962. **12**(4): p. 203-211211. http://dx.doi.org/10.1016/0042-207x(62)90978-8.

100. DeBoer, J., *Adsorption phenomena.* Adv. Catal., 1956. **8**: p. 17-161. http://dx.doi.org/10.1016/s0360-0564(08)60538-6.

101. Masel, R.I., *Principles of adsorption and reaction on solid surfaces*. 1996: John Wiley & Sons.

102. Redhead, P.A., *Thermal desorption of gases.* Vacuum, 1962. **12**(4): p. 203-211.

103. Habenschaden, E. and J. Küppers, *Evaluation of flash desorption spectra.* Surf. Sci., 1984. **138**(1): p. L147-L150. http://dx.doi.org/10.1016/0167-2584(84)90346-3.

104. Liberman, V., G. Haase, and R.M. Osgood, *Light-induced interaction of CCl4 with GaAs(110).* Surf. Sci., 1992. **268**(1-3): p. 307-318. http://dx.doi.org/10.1016/0039-6028(92)90970-h.

105. King, D.A., *Thermal desorption from metal surfaces: A review.* Surf. Sci., 1975. **47**(1): p. 384-402. http://dx.doi.org/10.1016/0039-6028(75)90302-7.

106. Martínez, F. and A. Gómez, *Thermodynamic study of the solubility of some sulfonamides in octanol, water, and the mutually saturated solvents.* J. Solution Chem., 2001. **30**(10): p. 909-923. http://dx.doi.org/10.1023/A:1012723731104.

107. Burawoy, A., *Licht-Absorption und Konstitution, I. Mitteil.: Homöopolare organische Verbindungen.* Berichte der deutschen chemischen Gesellschaft (A

and B Series), 1930. **63**(11): p. 3155-3172. http://dx.doi.org/10.1002/cber.19300631130.

108. Sun, S.-S., et al., *Introduction to Organic Electronic and Optoelectronic Materials and Devices (Optical Science and Engineering Series)*. 2008: CRC Press, Inc.

109. Scott, A.P. and L. Radom, *Harmonic Vibrational Frequencies: An Evaluation of Hartree−Fock, Møller−Plesset, Quadratic Configuration Interaction, Density Functional Theory, and Semiempirical Scale Factors*. J. Phys. Chem., 1996. **100**(41): p. 16502-16513. http://dx.doi.org/10.1021/jp960976r.

110. Brandbyge, M., et al., *Density-functional method for nonequilibrium electron transport*. Phys. Rev. B, 2002. **65**(16): p. 17. http://dx.doi.org/10.1103/PhysRevB.65.165401.

111. Nazeeruddin, M.K., et al., *Combined experimental and DFT-TDDFT computational study of photoelectrochemical cell ruthenium sensitizers*. J. Am. Chem. Soc., 2005. **127**(48): p. 16835-16847. http://dx.doi.org/10.1021/ja052467l.

112. Kumar, S., et al., *The weighted histogram analysis method for free-energy calculations on biomolecules .1. the method*. J. Comput. Chem., 1992. **13**(8): p. 1011-1021. http://dx.doi.org/10.1002/jcc.540130812.

113. Brooks, B.R., et al., *CHARMM: The Biomolecular Simulation Program*. J. Comput. Chem., 2009. **30**(10): p. 1545-1614. http://dx.doi.org/10.1002/jcc.21287.

114. Perdew, J.P., K. Burke, and M. Ernzerhof, *Generalized gradient approximation made simple*. Phys. Rev. Lett., 1996. **77**(18): p. 3865. http://dx.doi.org/10.1103/PhysRevLett.78.1396.

115. Grimme, S., *Semiempirical GGA‐type density functional constructed with a long‐range dispersion correction*. J. Comput. Chem., 2006. **27**(15): p. 1787-1799. http://dx.doi.org/10.1002/jcc.20495.

116. Burkert, U. and N.L. Allinger, *Molecular mechanics*. 1982: American Chemical Society Washington, DC.

117. Rosei, F., et al., *Properties of large organic molecules on metal surfaces.* Prog. Surf. Sci., 2003. **71**(5-8): p. 95-146. http://dx.doi.org/10.1016/s0079-6816(03)00004-2.

118. Ponder, J.W. and F.M. Richards, *An efficient newton-like method for molecular mechanics energy minimization of large molecules.* J. Comput. Chem., 1987. **8**(7): p. 1016-1024. http://dx.doi.org/10.1002/jcc.540080710.

119. Allinger, N.L., Y.H. Yuh, and J.H. Lii, *Molecular mechanics. The MM3 force field for hydrocarbons. 1.* J. Am. Chem. Soc., 1989. **111**(23): p. 8551-8566. http://dx.doi.org/10.1021/ja00205a001.

120. Lii, J.H. and N.L. Allinger, *Directional hydrogen bonding in the MM3 force field: II.* J. Comput. Chem., 1998. **19**(9): p. 1001-1016. http://dx.doi.org/10.1002/(sici)1096-987x(19980715)19:9<1001::aid-jcc2>3.0.co;2-u.

121. Bailey, M. and C.J. Brown, *Crystal structure of terephthalic acid.* Acta Crystallogr., 1967. **22**: p. 387. http://dx.doi.org/10.1107/s0365110x67000751.

122. Foloppe, N. and J.A.D. MacKerell, *All-atom empirical force field for nucleic acids: I. Parameter optimization based on small molecule and condensed phase macromolecular target data.* J. Comput. Chem., 2000. **21**(2): p. 86-104. http://dx.doi.org/10.1002/(SICI)1096-987X(20000130)21:2<86::AID-JCC2>3.0.CO;2-G.

123. Saiz-Poseu, J., et al., *Self-assembly of alkylcatechols on HOPG investigated by scanning tunneling microscopy and molecular dynamics simulations.* CrystEngComm, 2012. **14**(1): p. 264-271. http://dx.doi.org/10.1039/c1ce06010d.

124. Hohenberg, P. and W. Kohn, *Inhomogeneous electron gas.* Phys. Rev. B, 1964. **136**(3B): p. 864-871. http://dx.doi.org/10.1103/PhysRev.136.B864.

125. Kohn, W. and L.J. Sham, *Self-consistent equations including exchange and correlation effects*. Phys. Rev., 1965. **140**(4A): p. 1133-1138. http://dx.doi.org/10.1103/PhysRev.140.A1133.

126. Delley, B., *From molecules to solids with the DMol(3) approach*. J. Chem. Phys., 2000. **113**(18): p. 7756-7764. http://dx.doi.org/10.1063/1.1316015.

127. Schwabe, T. and S. Grimme, *Double-hybrid density functionals with long-range dispersion corrections: higher accuracy and extended applicability*. Phys. Chem. Chem. Phys., 2007. **9**(26): p. 3397-3406. http://dx.doi.org/10.1039/b704725h.

128. Grimme, S., *Accurate description of van der Waals complexes by density functional theory including empirical corrections*. J. Comput. Chem., 2004. **25**(12): p. 1463-1473. http://dx.doi.org/10.1002/jcc.20078.

129. Mammen, M., et al., *Estimating the entropic cost of self-assembly of multiparticle hydrogen-bonded aggregates based on the cyanuric acid center dot melamine lattice*. J. Org. Chem., 1998. **63**(12): p. 3821-3830. http://dx.doi.org/10.1021/jo970944f.

130. Murray, C.W. and M.L. Verdonk, *The consequences of translational and rotational entropy lost by small molecules on binding to proteins*. J. Comput. Aided Mol. Des., 2002. **16**(10): p. 741-753. http://dx.doi.org/10.1023/a:1022446720849.

131. Xu, B., et al., *Fast and accurate computation schemes for evaluating vibrational entropy of proteins*. J. Comput. Chem., 2011. **32**(15): p. 3188-3193. http://dx.doi.org/10.1002/jcc.21900.

132. Ohkubo, Y.Z. and C.L. Brooks, *Exploring Flory's isolated-pair hypothesis: Statistical mechanics of helix–coil transitions in polyalanine and the C-peptide from RNase A*. Proc. Natl Acad. Sci., 2003. **100**(24): p. 13916-13921. http://dx.doi.org/10.1073/pnas.2334257100.

133. Prins, L.J., D.N. Reinhoudt, and P. Timmerman, *Noncovalent synthesis using hydrogen bonding*. Angew. Chem. Int. Ed., 2001. **40**(13): p. 2382-2426.

http://dx.doi.org/10.1002/1521-3773(20010702)40:13<2382::AID-ANIE2382>3.0.CO;2-G.

134. Tsubomura, H., *Nature of the Hydrogen Bond. II. The Effect of Hydrogen Bonding and Other Solute‐Solvent Interactions upon the Shape and Intensity of the Infrared OH Band of Phenol.* J. Chem. Phys., 1955. **23**(11): p. 2130-2133. http://dx.doi.org/10.1063/1.1740682.

135. Tsubomura, H., *Nature of the Hydrogen Bond. III. The Measurement of the Infrared Absorption Intensities of Free and Hydrogen‐Bonded OH Bands. Theory of the Increase of the Intensity Due to the Hydrogen Bond.* J. Chem. Phys., 1956. **24**(5): p. 927-931. http://dx.doi.org/10.1063/1.1742717.

136. Larson, J.W. and T.B. McMahon, *Gas-phase bihalide and pseudobihalide ions. An ion cyclotron resonance determination of hydrogen bond energies in XHY- species (X, Y = F, Cl, Br, CN).* Inorg. Chem., 1984. **23**(14): p. 2029-2033. http://dx.doi.org/10.1021/ic00182a010.

137. Singh, S., A.S.N. Murthy, and C.N.R. Rao, *Spectroscopic studies of hydrogen bonding in donor-acceptor systems.* Trans. Faraday Society, 1966. **62**(0): p. 1056-1066. http://dx.doi.org/10.1039/TF9666201056.

138. Cottrell, T.L., *The strengths of chemical bonds*. 1958: Butterworths.

139. Singhal, A., *Physical chemistry for the IIT JEE*. 2009: Pearson Education India.

140. Darwent, B., *Bond dissociation energies in simple molecules*. 1970: NSRDS-NBS No. 31, U. S. Dept. Commerce, Washington, D. C. 48 p.

141. Desiraju, G.R., *The C−H···O Hydrogen Bond: Structural Implications and Supramolecular Design.* Acc. Chem. Res., 1996. **29**(9): p. 441-449. http://dx.doi.org/10.1021/ar950135n.

142. Gilli, G., et al., *Resonance-assisted hydrogen-bonding. 3. Formation of intermolecular hydrogen-bonded chains in crystals of beta-diketone enols and its relevance to molecular association.* Acta Crystallogr., Sect. B: Struct. Sci, 1993. **49**: p. 564-576. http://dx.doi.org/10.1107/s0108768192012278.

143. Allen, G., J.G. Watkinson, and K.H. Webb, *An infrared study of the association of benzoic acid in the vapour phase, and in dilute solution in non-polar solvents.* Spectrochim. Acta, 1966. **22**(5): p. 807-814. http://dx.doi.org/10.1016/0371-1951(66)80110-8.

144. Brinck, T., J.S. Murray, and P. Politzer, *Surface electrostatic potentials of halogenated methanes as indicators of directional intermolecular interactions.* Int. J. Quantum Chem, 1992. **44**(S19): p. 57-64. http://dx.doi.org/10.1002/qua.560440709.

145. Auffinger, P., et al., *Halogen bonds in biological molecules.* Proc. Natl. Acad. Sci. U.S.A., 2004. **101**(48): p. 16789-16794. http://dx.doi.org/10.1073/pnas.0407607101.

146. Awwadi, F.F., et al., *The Nature of Halogen···Halogen Synthons: Crystallographic and Theoretical Studies.* Chem. Eur. J., 2006. **12**(35): p. 8952-8960. http://dx.doi.org/10.1002/chem.200600523.

147. Wilcken, R., et al., *Principles and Applications of Halogen Bonding in Medicinal Chemistry and Chemical Biology.* J. Med. Chem., 2012. **56**(4): p. 1363-1388. http://dx.doi.org/10.1021/jm3012068.

148. Tang, M.L. and Z. Bao, *Halogenated Materials as Organic Semiconductors†.* Chem. Mater., 2010. **23**(3): p. 446-455. http://dx.doi.org/10.1021/cm102182x.

149. Fourmigué, M. and P. Batail, *Activation of Hydrogen- and Halogen-Bonding Interactions in Tetrathiafulvalene-Based Crystalline Molecular Conductors.* Chem. Rev., 2004. **104**(11): p. 5379-5418. http://dx.doi.org/10.1021/cr030645s.

150. Walch, H., et al., *Material- and Orientation-Dependent Reactivity for Heterogeneously Catalyzed Carbon−Bromine Bond Homolysis.* J. Phys. Chem. C, 2010. **114**(29): p. 12604-12609. http://dx.doi.org/10.1021/jp102704q.

151. Bosch, E. and C.L. Barnes, *Triangular Halogen−Halogen−Halogen Interactions as a Cohesive Force in the Structures of Trihalomesitylenes.* Cryst. Growth Des., 2002. **2**(4): p. 299-302. http://dx.doi.org/10.1021/cg025517w.

152. Chung, K.-H., et al., *Polymorphic porous supramolecular networks mediated by halogen bonds on Ag(111).* Chem. Commun., 2011. **47**(41): p. 11492-11494. http://dx.doi.org/10.1039/C1CC14679C.

153. Grimme, S., *Do special noncovalent π–π stacking interactions really exist?* Angew. Chem. Int. Ed., 2008. **47**(18): p. 3430-3434. http://dx.doi.org/10.1002/anie.200705157.

154. Hunter, C.A. and J.K. Sanders, *The nature of π-π interactions.* J. Am. Chem. Soc., 1990. **112**(14): p. 5525-5534. http://dx.doi.org/10.1021/ja00170a016.

155. Sinnokrot, M.O. and C.D. Sherrill, *Substituent Effects in π−π Interactions: Sandwich and T-Shaped Configurations.* J. Am. Chem. Soc., 2004. **126**(24): p. 7690-7697. http://dx.doi.org/10.1021/ja0049434a.

156. Björk, J., et al., *Adsorption of Aromatic and Anti-Aromatic Systems on Graphene through π−π Stacking.* J. Phys. Chem. Lett., 2010. **1**(23): p. 3407-3412. http://dx.doi.org/10.1021/jz101360k.

157. Moradian-Oldak, J., W. Leung, and A.G. Fincham, *Temperature and pH-dependent supramolecular self-assembly of amelogenin molecules: A dynamic light-scattering analysis.* J. Struct. Biol., 1998. **122**(3): p. 320-327. http://dx.doi.org/10.1006/jsbi.1998.4008.

158. Albrecht, M., *Dicatechol ligands: novel building-blocks for metallo-supramolecular chemistry.* Chem. Soc. Rev., 1998. **27**(4): p. 281-287. http://dx.doi.org/10.1039/a827281z.

159. Stepanow, S., et al., *Deprotonation-Driven Phase Transformations in Terephthalic Acid Self-Assembly on Cu(100).* J. Phys. Chem. B, 2004. **108**(50): p. 19392-19397. http://dx.doi.org/10.1021/jp046766t.

160. Clair, S., et al., *STM study of terephthalic acid self-assembly on Au(111): Hydrogen-bonded sheets on an inhomogeneous substrate.* J. Phys. Chem. B, 2004. **108**(38): p. 14585-14590. http://dx.doi.org/10.1021/jp049501n.

161. Canas-Ventura, M.E., et al., *Coexistence of one- and two-dimensional supramolecular assemblies of terephthalic acid on Pd(111) due to self-limiting deprotonation.* J. Chem. Phys., 2006. **125**(18): p. http://dx.doi.org/10.1063/1.2364478.

162. Prauzner-Bechcicki, J.S., et al., *High-Resolution STM Studies of Terephthalic Acid Molecules on Rutile TiO2(110)-(1 × 1) Surfaces.* J. Phys. Chem. C, 2009. **113**(21): p. 9309-9315. http://dx.doi.org/10.1021/jp901184t.

163. Fortuna, S. and A. Troisi, *Agent-Based Modeling for the 2D Molecular Self-Organization of Realistic Molecules.* J. Phys. Chem. B, 2010. **114**(31): p. 10151-10159. http://dx.doi.org/10.1021/jp103950m.

164. De Jong, A.M. and J.W. Niemantsverdriet, *Thermal desorption analysis: comparative test of 10 commonly applied procedures.* Surf. Sci., 1990. **233**(3): p. 355-365. http://dx.doi.org/10.1016/0039-6028(90)90649-s.

165. Gilli, G., et al., *Evidence for resonance-assisted hydrogen-bonding from crystal-structure correlations on the enol form of the beta-diketone fragment.* J. Am. Chem. Soc., 1989. **111**(3): p. 1023-1028. http://dx.doi.org/10.1021/ja00185a035.

166. Bickerstaffe, A.K., et al., *The crystalline structures of carboxylic acid monolayers adsorbed on graphite.* J. Phys. Chem. B, 2006. **110**(11): p. 5570-5575. http://dx.doi.org/10.1021/jp054798q.

167. Müller, T., et al., *Temperature-programmed desorption studies of n-alkane derivatives on graphite: Desorption energetics and the influence of functional groups on adsorbate self-assembly.* Langmuir, 2003. **19**(7): p. 2812-2821. http://dx.doi.org/10.1021/la020856c.

168. Kampschulte, L., et al., *Thermodynamical Equilibrium of Binary Supramolecular Networks at the Liquid−Solid Interface.* J. Am. Chem. Soc., 2008. **130**(26): p. 8502-8507. http://dx.doi.org/10.1021/ja801883t.

169. Furukawa, S., et al., *Structural Transformation of a Two-Dimensional Molecular Network in Response to Selective Guest Inclusion.* Angew. Chem. Int. Ed., 2007. **46**(16): p. 2831-2834. http://dx.doi.org/10.1002/anie.200604782.

170. Ahn, S. and A.J. Matzger, *Additive perturbed molecular assembly in two-dimensional crystals: differentiating kinetic and thermodynamic pathways*. J. Am. Chem. Soc., 2012. **134**(6): p. 3208-3214. http://dx.doi.org/10.1021/ja210933h.

171. Miao, X.R., et al., *Solvent-Induced Structural Transitions of a 1,3,5-Tris(10-ethoxycarbonyldecyloxy)benzene Assembly Revealed by Scanning Tunneling Microscopy*. J. Phys. Chem. C, 2011. **115**(8): p. 3358-3367. http://dx.doi.org/10.1021/jp109686n.

172. Schaake, R.C.F., J.C. Vanmiltenburg, and C.G. Dekruif, *Thermodynamic Properties of the Normal Alkanoic Acids .1. Molar Heat-Capacities of 7 Odd-Numbered Normal Alkanoic Acids*. J. Chem. Thermodyn., 1982. **14**(8): p. 763-769. http://dx.doi.org/10.1016/0021-9614(82)90172-0.

173. Iwahashi, M., et al., *Dissociation of dimeric cis-9-octadecenoic acid in its pure liquid state as observed by near-infrared spectroscopic measurement*. J. Phys. Chem., 1993. **97**(13): p. 3129-3133. http://dx.doi.org/10.1021/j100115a011.

174. Murthy, A.S.N. and C.N.R. Rao, *Spectroscopic Studies of the Hydrogen Bond*. Appl. Spectrosc. Rev., 1968. **2**(1): p. 69-191. http://dx.doi.org/10.1080/05704926808050887.

175. Stevens, F. and T.P. Beebe, *Dynamical Exchange Behavior in Organic Monolayers Studied by STM Analysis of Labeled Mixtures*. Langmuir, 1999. **15**(20): p. 6884-6889. http://dx.doi.org/10.1021/la980416e.

176. Padowitz, D.F. and B.W. Messmore, *STM Observations of Exchange Dynamics at the Solid−Liquid Interface Using a Molecular Tracer*. J. Phys. Chem. B, 2000. **104**(43): p. 9943-9946. http://dx.doi.org/10.1021/jp002198f.

177. De Jong, A.M. and J.W. Niemantsverdriet, *Thermal desorption analysis: Comparative test of ten commonly applied procedures*. Surf. Sci., 1990. **233**(3): p. 355-365. http://dx.doi.org/10.1016/0039-6028(90)90649-s.

178. Bickerstaffe, A., et al., *The crystalline structures of carboxylic acid monolayers adsorbed on graphite.* J. Phys. Chem. B, 2006. **110**(11): p. 5570-5575. http://dx.doi.org/10.1021/jp054798q.

179. Hibino, M., et al., *Microscopic origin of the odd-even effect in monolayer of fatty acids formed on a graphite surface by scanning tunneling microscopy.* J. Phys. Chem. B, 1998. **102**(23): p. 4544-4547. http://dx.doi.org/10.1021/jp973412b.

180. Hoeppener, S., L.F. Chi, and H. Fuchs, *Molecular arrangement of fatty acids at the solid-liquid interface visualized by chemical decoration.* ChemPhysChem, 2003. **4**(5): p. 494-498. http://dx.doi.org/10.1002/cphc.200200584.

181. Rybolt, T.R., et al., *Evaluation of molecular mechanics calculated binding energies for isolated and monolayer organic molecules on graphite.* J. Colloid Interface Sci., 2007. **314**(2): p. 434-445. http://dx.doi.org/10.1016/j.jcis.2007.05.083.

182. Zacharia, R., H. Ulbricht, and T. Hertel, *Interlayer cohesive energy of graphite from thermal desorption of polyaromatic hydrocarbons.* Phys. Rev. B, 2004. **69**(15): p. 155406. http://dx.doi.org/10.1103/PhysRevB.69.155406.

183. Chakarova-Käck, S.D., et al., *Application of van der Waals Density Functional to an Extended System: Adsorption of Benzene and Naphthalene on Graphite.* Phys. Rev. Lett., 2006. **96**(14): p. 146107. http://dx.doi.org/10.1103/PhysRevLett.96.146107.

184. Fisher, A.J. and P.E. Blöchl, *Adsorption and scanning-tunneling-microscope imaging of benzene on graphite and MoS_2.* Phys. Rev. Lett., 1993. **70**(21): p. 3263-3266. http://dx.doi.org/10.1103/PhysRevLett.70.3263.

185. Shimada, J., et al., *Conformation of Amylose in Aqueous Solution: Small-Angle X-ray Scattering Measurements and Simulations.* J. Phys. Chem. B, 2000. **104**(9): p. 2136-2147. http://dx.doi.org/10.1021/jp992650z.

186. Aliev, A.E. and D. Courtier-Murias, *Experimental verification of force fields for molecular dynamics simulations using Gly-Pro-Gly-Gly.* J. Phys. Chem. B, 2010. **114**(38): p. 12358-12375. http://dx.doi.org/10.1021/jp101581h.

187. Wilms, M., et al., *In-situ STM investigation of adsorbate structures on Cu(111) in sulfuric acid electrolyte.* Surf. Sci., 1998. **416**(1–2): p. 121-140. http://dx.doi.org/10.1016/S0039-6028(98)00550-0.

188. Martsinovich, N. and A. Troisi, *Modeling the Self-Assembly of Benzenedicarboxylic Acids Using Monte Carlo and Molecular Dynamics Simulations.* J. Phys. Chem. C, 2010. **114**(10): p. 4376-4388. http://dx.doi.org/10.1021/jp911671b.

189. Marie, C., et al., *Tuning the Packing Density of 2D Supramolecular Self-Assemblies at the Solid−Liquid Interface Using Variable Temperature.* ACS Nano, 2010. **4**(3): p. 1288-1292. http://dx.doi.org/10.1021/nn901717k.

190. Sirtl, T., et al., *Solvent-Dependent Stabilization of Metastable Monolayer Polymorphs at the Liquid–Solid Interface.* ACS Nano, 2013. **7**(8): p. 6711-6718. http://dx.doi.org/10.1021/nn4014577.

191. Kendrick, C., A. Kahn, and S.R. Forrest, *STM study of the organic semiconductor PTCDA on highly-oriented pyrolytic.* Appl. Surf. Sci., 1996. **104**: p. 586-594. http://dx.doi.org/10.1016/s0169-4332(96)00207-3.

192. Mazur, U., K.W. Hipps, and S.L. Riechers, *Organization of Vanadyl and Metal-Free Tetraphenoxyphthalocyanine Complexes on Highly Oriented Pyrolytic Graphite in the Presence of Paraffinic Solvents: A STM Study.* J. Phys. Chem. C, 2008. **112**(51): p. 20347-20356. http://dx.doi.org/10.1021/jp805684z.

193. Hedgeland, H., et al., *Measurement of single-molecule frictional dissipation in a prototypical nanoscale system.* Nat. Phys., 2009. **5**(8): p. 561-564. http://dx.doi.org/10.1038/nphys1335.

194. Lifson, S., A.T. Hagler, and P. Dauber, *Consistent force field studies of intermolecular forces in hydrogen-bonded crystals. 1. Carboxylic acids, amides, and the C=O···H- hydrogen bonds.* J. Am. Chem. Soc., 1979. **101**(18): p. 5111-5121. http://dx.doi.org/10.1021/ja00512a001.

195. Meier, B.H., F. Graf, and R.R. Ernst, *Structure and dynamics of intramolecular hydrogen bonds in carboxylic acid dimers: A solid state NMR study.* J. Chem. Phys., 1982. **76**(2): p. 767-774. http://dx.doi.org/10.1063/1.443045.

196. Verevkin, S.P., *Measurement and Prediction of the Monocarboxylic Acids Thermochemical Properties.* J. Chem. Eng. Data, 2000. **45**(5): p. 953-960. http://dx.doi.org/10.1021/je990282m.

197. Metrangolo, P., et al., *Halogen bonding based recognition processes: a world parallel to hydrogen bonding.* Acc. Chem. Res., 2005. **38**(5): p. 386-395. http://dx.doi.org/10.1021/ar0400995.

198. Lu, Y., et al., *Halogen Bonding—A Novel Interaction for Rational Drug Design?* J. Med. Chem., 2009. **52**(9): p. 2854-2862. http://dx.doi.org/10.1021/jm9000133.

199. Kolar, M., P. Hobza, and A.K. Bronowska, *Plugging the explicit σ-holes in molecular docking.* Chem. Commun., 2013. **49**(10): p. 981-983. http://dx.doi.org/10.1039/C2CC37584B.

200. Politzer, P., et al., *An overview of halogen bonding.* J. Mol. Model., 2007. **13**(2): p. 305-311. http://dx.doi.org/10.1007/s00894-006-0154-7.

201. Clark, T., et al., *Halogen bonding: the σ-hole.* J. Mol. Model., 2007. **13**(2): p. 291-296. http://dx.doi.org/10.1007/s00894-006-0130-2.

202. Politzer, P., J. Murray, and M. Concha, *σ-hole bonding between like atoms; a fallacy of atomic charges.* J. Mol. Model., 2008. **14**(8): p. 659-665. http://dx.doi.org/10.1007/s00894-008-0280-5.

203. Yoon, J.K., et al., *Visualizing Halogen Bonds in Planar Supramolecular Systems.* J. Phys. Chem. C, 2011. **115**(5): p. 2297-2301. http://dx.doi.org/10.1021/jp110891y.

204. Chen, Q., et al., *Two-dimensional OPV4 self-assembly and its coadsorption with alkyl bromide: from helix to lamellar.* Chem. Commun., 2009. (25): p. 3765-3767. http://dx.doi.org/10.1039/B905281J.

205. Russell, J.C., et al., *Dimerization of Tri(4-bromophenyl)benzene by Aryl−Aryl Coupling from Solution on a Gold Surface.* J. Am. Chem. Soc., 2011. **133**(12): p. 4220-4223. http://dx.doi.org/10.1021/ja110837s.

206. Gutzler, R., et al., *Halogen bonds in 2D supramolecular self-assembly of organic semiconductors.* Nanoscale, 2012. **4**(19): p. 5965-5971. http://dx.doi.org/10.1039/C2NR31648J.

207. Giannozzi, P., et al., *QUANTUM ESPRESSO: a modular and open-source software project for quantum simulations of materials.* J. Phys.: Condens. Matter, 2009. **21**(39): p. 395502. http://dx.doi.org/10.1088/0953-8984/21/39/395502.

208. Tsuzuki, S., et al., *Magnitude and Origin of the Attraction and Directionality of the Halogen Bonds of the Complexes of C6F5X and C6H5X (X=I, Br, Cl and F) with Pyridine.* Chem. Eur. J., 2012. **18**(3): p. 951-960. http://dx.doi.org/10.1002/chem.201102562.

List of Figures

Figure 1.1. The schematic of a simplified quantum tunneling model between two metal electrodes 6

Figure 1.2. Tip model defined by Tersoff and Hamann. 9

Figure 1.3. Sketch of the STM setup. 11

Figure 2.1. The sublimation enthalpy measurement setup and an example. 17

Figure 2.2. Experimental setup for TPD. The sample is mounted inside a stainless steel UHV chamber. 21

Figure 2.3. An example of TPD measurements: TPA from graphite in UHV...... 24

Figure 2.3. a scheme of the UV-vis absorption spectrometer. 27

Figure 2.4. Measurement of TPA solubility in 9A as a function of temperature . 28

Figure 2.5. Free volume for hard cube approximation. 34

Figure 3.1. Molecular structures of used solvents and molecules 37

Figure 3.2. scheme of two-fold cyclic hydrogen bonds 38

Figure 3.3. Arrangement of HBTP molecules in an adsorbed monolayer.. 39

Figure 4.1. STM image of a TPA monolayer at the nonanoic acid−graphite interface. 47

Figure 4.2. Scheme of the proposed Born−Haber cycle.. 48

Figure 4.3. Measurement of the TPA effusion rate as a function of temperature. 49

Figure 4.4. Measurement of the TPA solubility in 9A as a function of temperature. 50

Figure 4.5. Temperature Programmed Desorption of TPA from graphite in ultra-high vacuum. 52

Figure 4.6. Results for the Born−Haber cycle. 54

Figure 4.7 STM images obtained at various temperatures 58

Figure 4.8. STM topography of a self-assembled nonanoic acid monolayer at the graphite-liquid nonanoic acid interface. 63

Figure 4.9. Structures of simulated 2D monolayers of 9A 68

Figure 4.10. Lowest-energy adsorption geometry for a 9A molecule on graphite 69

Figure 5.1. STM images of SDA monolayer at the nonanoic acid-graphite interface 76

Figure 5.2. Temperature Programmed Desorption of SDA from graphite 80

Figure 5.3. Model of the lowest energy SDA monolayer structure based on the experimental commensurate superstructure 81

Figure 5.4. Measurement of the SDA effusion rate from a Knudsen-cell by a Quartz Crystal Microbalance. 83

Figure 5.5. SDA solubility measurements in 9A as a function of temperature 84

Figure 5.6. Results for the Born-Haber cycle for SDA with respect to vacuum, i.e. with respect to free single molecule. 86

Figure 5.7. STM split-image of a SDA monolayer at the nonanoic acid-graphite interface. 89

Figure. 6.1. High resolution STM image of a HBTP monolayer and DFT optimized geometry 94

Figure. 6.2. Enthalpy diagram of the HBTP–7A–graphite system. 96

Figure. 6.3. Experimental determination of $\Delta H_{cryst \rightarrow vac}$ and $\Delta H_{cryst \rightarrow sol.}$ 97

Figure. 6.4. High-resolution STM image of a HBTP monolayer acquired at the 7A-graphite interface. 100

Figure. 6.5. Overview STM image of a HBTP monolayer acquired at the 7A–graphite interface. 101

Figure. 6.6. Optimized structures of 7A + HBTP aggregates.. 104

Figure 7.1. Born-Haber cycle of TPA self-assembly at the 9A-graphite interface.. 111

Figure 7.2. Born-Haber cycle of SDA self-assembly at the 9A-graphite interface.. 111

Figure 7.3. Thermodynamic driving force of halogen bonded networks at the 7A-graphite interface is determined using a hybrid Born-Haber cycle. 112

List of Publications

2014

Explosives Sensing by Using Electron-Rich Supramolecular Polymers: Role of Intermolecular Hydrogen Bonding in Significant Enhancement of Sensitivity

Bappaditya Gole, **Wentao Song,** Markus Lackinger and Partha Sarathi Mukherjee*,
Chem. Eur. J., 2014, 20, 1-20.

Thermodynamics of halogen bonded monolayer self-assembly at the liquid-solid interface

Wentao Song, Natalia Martsinovich, Wolfgang M. Heckl, and Markus Lackinger*,
Chem. Commun., 2014, 50, 13465-13468
Cf. Chapter 6

Thermodynamics of 4, 4’ -stilbenedicarboxylic acid monolayer self-assembly at the nonanoic acid-graphite interface

Wentao Song, Natalia Martsinovich, Wolfgang M. Heckl, and Markus Lackinger*,
Phys. Chem. Chem. Phys., 2014, 16, 13239-13247.
Cf. Chapter 5

2013

A Born-Haber cycle for monolayer self-assembly at the liquid-solid interface － assessing the enthalpic driving force

Wentao Song, Natalia Martsinovich, Wolfgang M. Heckl, and Markus Lackinger*,
J. Am. Chem. Soc., 2013, 135 (39), 14854-14862.
This article is highlighted in ***Nature Chemistry***
Cf. Chapter 4

Solvent-dependent stabilization of metastable monolayer polymorphs at the liquid-solid interface

Thomas Sirtl, **Wentao Song,** Georg Eder, Subhadip Neogi, Michael Schmittel, Wolfgang M. Heckl, and Markus Lackinger*, ACS Nano , 2013, 7 (8), 6711-6718.

2011

Characteristics of charge density waves on the surfaces of quasi-one-dimensional charge-transfer complex layered organic crystals

Feng Lin*, Xiaoming Huang, Shengchun Qu, Zheyu Fang, Shan Huang, **Wentao Song,** Xing Zhu, Zhongfan Liu
Phys. Rev. B 83, 125434, 2011.

Plasmonic Focusing in Symmetry Broken Nanocorrals

Zheyu Fang, Qian Peng, **Wentao Song**, Fenghuan Hao, Jia Wang, Peter Nordlander, Xing Zhu*, Nano Letters, 11(2), pp 893-897

2010

Homogeneous Epitaxial Growth of N, N '-di (n-butyl) quinacridone Thin Films on Ag (110)

Feng Lin, Zheyu Fang, Shengchun Qu, Shan Huang, **Wentao Song,** Lifeng Chi*, Xing Zhu, Journal of Nanoscience and Nanotechnology, 10(11), pp 7162-7166, 2010/11.

Near-field nanofocusing through a combination of plasmonic Bragg reflector and converging lens

Wentao Song, Zheyu Fang, Shan Huang, Feng Lin, Xing Zhu*, Optics Express, Vol. 18, 14762, 2010.

Nanofocusing by Phase delayed Plasmonic Nanostructures illuminated with a linearly polarized light

Wentao Song, Zheyu Fang, Feng Lin, Xing Zhu*, Acta Phys. Sin., 2010, 59(10): 6921-6926. (In Chinese)

2009

Focusing of surface plasmon polariton trapping of colloidal particles

Zheyu Fang, Feng Lin, Shan Huang, **Wentao Song,** Xing Zhu*, Applied Physics Letters, Vol. 94, 063306, (2009).

Dielectric loaded surface plasmon polariton characterization by using near-field optical microscopy

Zheyu Fang, **Wentao Song,** Chen Wang, Hong Qi, Feng Lin, Xing Zhu*, Journal of Chinese Electron Microscopy Society, **2**, 111, (2009). (In Chinese)

Acknowledgement

I would like to thank PD. Dr. Markus Lackinger for inviting me from China, and for helping me with the application of my scholarship, so that I have the opportunity to see Europe and to work in his group. From Markus, I have learned all the scientific and technical knowledge in this dissertation. Without all the discussions and working with him during the past four years, this dissertation would not exist. In addition, I would like to thank Markus for proofreading the endless errors of this dissertation.

I would like to thank Prof. Dr. Wolfgang Heckl for accepting me as a PhD candidate at the Physics department of TUM and also for the opportunity to work in the lab of the Deutsches Museum.

I would like to thank Natalia Martsinovich (University of Sheffield, UK). She performed all the simulations in this dissertation.

I would like to thank all my colleagues and former colleagues: Atena, Christoph, George, Jürgen, Matthias, Johanna, Oliver, Saskia, Stephan Kloft, Stefan Schlögl, Prof. Stefan Sotier, and Thommi for creating the nice working environment, teaching me all the equipments, sharing all the different cultures, and being so nice and patient with me in the past years.

I would like to thank all my friends in Munich for sharing their time and stories with me. Spending time with them released all my pressure and made me feel like at home.

I would like to thank my Chinese friends for organizing weekly parties, and also for the helps they have offered. Thank Xiaoyin Cheng and her husband Bohao Xie, they treated me as a real family. From them, I learnt how to get along with family and how to enjoy life.

I would like to thank my father for his trust and all the unconditional support. He never ran away from his responsibilities even when life was extremely difficult. Thank my mother for her pushing and training in my childhood. She gave me the will to change my life and conquer all hardships. Thank my younger brother for reminding me all the social responsibilities, and enduring my push on everything in our childhood.

In the end, I would like to thank my girlfriend Shizhu Sun, for sharing her life with me in the past years, for facing all the difficulties in our lives without giving up. Thank her for helping me through the valley of my life and for her belief in me. Her company and encouragement keep reminding me the purpose of my life and what kind of man I want to be.

Wentao Song in January 2015

Curriculum Vitae

Name: Wentao Song

Birth: December 18th, 1986, in Linqu, Shandong, China.

University Studies

Since 2010: PhD candidate, Physics Department, Technical University of Munich, Germany

2007-2010: Master of Science in condensed matter physics, Physics department, Peking University, China

2003-2007: Bachelor of Science in Physics, Physics department, Jilin University, China

Teaching Experiences

Teaching high school physics, TAL Education Group, Beijing, China

Teaching assistant, Progress of in Nano Science and Nano Technology, Physics Department, Peking University, Beijing, China

Teaching assistant, Mechanics, Physics department, Peking University, Beijing, China

Tutor, Practical course-Basic experimental physics, Technical University of Munich, Munich, Germany